

A Thesis
entitled

Kinetic Monte Carlo simulations of submonolayer and
multilayer epitaxial growth over extended time- and
length-scales

by
GIRIDHAR NANDIPATI

Submitted as partial fulfillment of the requirements for the
Doctor of Philosophy Degree in Physics

Advisor: Dr. Jacques G Amar

Graduate School

The University of Toledo
August 2009

An Abstract of

Kinetic Monte Carlo simulations of submonolayer and multilayer
epitaxial growth over extended time- and length-scales

GIRIDHAR NANDIPATI

Submitted in partial fulfillment
of the requirements for the
Doctor of Philosophy Degree in Physics

The University of Toledo
August 2009

The main objective of the work presented in this thesis is to develop new methods to extend the time and length scales of atomistic kinetic Monte Carlo (KMC) simulations. When all the relevant processes and their activation barriers are known, KMC is an extremely efficient method to carry out atomistic simulations for longer time scales. However, in some cases (ex. low barrier repetitive events) direct KMC simulations may not be sufficient to reach the experimentally relevant length and time scales. Accordingly, we have tested and developed several different parallel KMC algorithms and also developed a dynamic boundary allocation (DBA) method to improve parallel efficiency by reducing number of boundary events. Results for parallel KMC simulations of Ag(111) island coarsening at room temperature carried out using a large database of processes obtained from previous self-learning KMC simulations are also presented. We find that at long times the coarsening behavior corresponds to Ostwald ripening. We also find that the inclusion of concerted small-cluster events has a significant impact on the average island size. In addition, we have also devel-

oped a first passage time (FPT) approach to KMC simulations to accelerate KMC simulation of (100) multilayer epitaxial growth with rapid edge diffusion. In our FPT approach, by mapping edge-diffusion to a 1D random walk, numerous diffusive hops are replaced with first-passage time to make one large jump to a new location. As a test, we have applied our method to carry out multilayer growth simulations of three different models. We note that despite the additional overhead, the FPT approach leads to a significant speed-up compared to regular KMC simulations

Finally, we present results obtained from KMC simulations of irreversible submonolayer island growth with strain and rapid island relaxation. Our results indicate that in the presence of large strain there is significant anisotropy in qualitative agreement with experiments on InAs/GaAs and Ge/Si growth. Somewhat surprisingly, we also find that the scaled island-size distribution depends only weakly on the effects of strain. This is in qualitative agreement with recent experimental results for InAs/GaAs(100) submonolayer growth.

ACKNOWLEDGEMENTS

I am grateful to my advisor Prof. Jacques G Amar without whose guidance, attention, and perseverance this work would not exist. I want to thank Prof. Amar for sharing with me his ideas, and for providing me with countless hours of simulating conversation. I want to particularly thank Prof. Amar for always being willing to provide keen insights and for his patience and belief in me.

I would also like to thank Dr. Yunsic Shim for numerous simulating discussions, ideas and his invaluable help and encouragement throughout my research work.

I would like to thank my Ph.D advisory committee Prof. Tom Kvale, Prof. Robert Collins, Prof. Lawrence Anderson-Huang and Prof. Terry P. Bigioni for their concern and valuable suggestions.

For their valuable collaboration I would like to thank Prof. Talat Rahman, Dr. Abdelkader Kara at University of Central Florida and also Dr. Altaf Karim at Brookhaven National Lab.

Finally, I would also like to extend my thanks to all faculty and staff at the Department of Physics & Astronomy for their support.

Contents

Abstract	ii
Acknowledgments	iv
Contents	v
List of Figures	ix
List of Tables	xv
1 Introduction	1
1.1 Simulations of Thin Film Growth	1
1.2 The scope of this thesis	2
2 Monte Carlo Methods	6
2.1 Introduction to Monte Carlo Methods	6
2.2 Metropolis Monte Carlo	8
2.2.1 Markov Chains	8
2.2.2 Metropolis Algorithm	10
2.3 Kinetic Monte Carlo	11

2.3.1	KMC Algorithm	12
2.3.2	Binary tree Search Algorithm	13
2.4	On-the-Fly/Self Learning Kinetic Monte Carlo	16
2.4.1	Introduction	16
2.4.2	Self Learning KMC Algorithm	17
3	Algorithms for Parallel Kinetic Monte Carlo	21
3.1	Introduction	21
3.2	KMC Algorithm	23
3.3	Parallel Algorithms for the kinetic Monte Carlo Method	24
3.3.1	Optimistic Synchronous Relaxation (OSR) Algorithm	24
3.3.2	Optimistic Synchronous Relaxation with Pseudo-Rollback (OS- RPR) Algorithm	27
3.3.3	Synchronous Sublattice (SL) Algorithm	29
3.3.4	Dynamic Boundary Allocation	31
3.4	Parallel Efficiency Results	33
4	Parallel Kinetic Monte Carlo Simulations of Ag(111) Island Coarsening using a Large Database	38
4.1	Introduction	38
4.2	KMC Database	39
4.3	Results for Ag/Ag(111) Island Coarsening	43
4.4	Analysis of energy barriers	52
4.5	Conclusion	55

5	First-passage time approach to kinetic Monte Carlo simulations of metal(100) growth	58
5.1	Introduction	58
5.2	Model	61
5.3	Application of FPT method to KMC	67
5.3.1	First-Passage Time for 1D Random Walker	67
5.3.2	Implementation of FPT approach	69
5.4	Results	76
5.5	Discussion	83
6	Effects of Strain on Island Morphology and Size Distribution in Ir-reversible Submonolayer Growth	90
6.1	Introduction	90
6.2	Model	93
6.3	Results	96
6.3.1	Monomer and island densities	96
6.3.2	Island morphology	98
6.3.3	Island-size distribution	106
6.4	Conclusion	108
7	Conclusions and Future Work	110
A	Ewald Sums	112
B	Derivation of Expressions used in FPT KMC	118

B.1	Mean First Passage Time	118
B.2	Absorption Probabilities	120
B.3	Expression for Conditional First Passage Time	122
B.4	Number of times random walker reaches the boundary	124
C	Characterization of Surface Morphology	128

List of Figures

2-1	A binary tree, transition rates for events of the same type are stored in the leaves and cumulative rates stored at higher levels. The arrows indicate the direction of descend when choosing the type of an event the be executed. The highest node contains the total rate of the system S_{total}	14
2-2	Two-shell indexing around central atom labeled 1	18
2-3	Example of a multiple atom process and also shows how a configuration is stored in the database.	19
2-4	Example of 120° rotation symmetry operation showing two symmetry related configurations (a) and (b).	20
3-1	Schematic diagram of square decomposition for $N_p=9$. Solid lines correspond to processor domains	25
3-2	Time evolution of events for OSR and OSRPR algorithms with $G = 4$. Dashed lines correspond to selected events, while the dashed line with an X corresponds to an event exceeding t_{min} (see text). In OSR this event is discarded while in OSRPR this event is added to the next cycle.	27

3-3	Comparison between parallel results using the OSRPR algorithm with square decomposition ($N_p = 4$) and serial results for fractal model with $D/F = 10^5$ and $G = 7$	28
3-4	Schematic diagram of strip decomposition for $N_p = 2$. Each processor domain is subdivided into A and B sublattices. Boundary and ghost regions for B sublattice of processor 1 are also shown.	30
3-5	Time evolution in the SL algorithm. Dashed lines correspond to selected events, while the dashed line with an X corresponds to an event which is rejected since it exceeds the cycle time τ	31
3-6	Example of square decomposition with DBA for system size $L = 512$ (triangular lattice with periodic boundary conditions) and $N_p = 4$. . .	32
3-7	Same as Fig. 3-6 but for strip decomposition into sublattices with $N_p = 4$. . .	33
3-8	Comparison of results for the island density obtained from coarsening simulations carried out using serial KMC with the corresponding results obtained using the SL algorithm with DBA for $N_p = 4$ and $\tau = 10^{-6}$ s.	37
4-1	Two typical low-barrier moves in the large cluster database along with the corresponding activation barriers E_b . Dark blue atom corresponds to the central atom involved in the transition, while light blue and red atoms correspond to occupied sites in the first and second rings, respectively. Third ring of atoms (orange) is also shown.	42

4-2	Some typical concerted moves in the small cluster database. Color code is the same as in Fig. 4-1.	43
4-3	Histogram of energy barriers in the combined large and small cluster database (histogram width is 0.01 eV).	44
4-4	Evolution of island morphology during room-temperature coarsening. Pictures correspond to 256×256 portions of 1024×1024 system. . .	46
4-5	Average island size $S(t)$ as function of time (open circles). Dashed line corresponds to simulations without concerted motion. Inset shows log-log plot of $S(t) - S(0)$	47
4-6	Island and monomer (inset) densities as function of time.	48
4-7	Effective coarsening exponent n_{eff} as function of $1/S$	49
4-8	Scaled island size distribution at four different times during coarsening.	51
4-9	Histogram of energy barriers of selected events during the first 100 s of coarsening. Histogram width is 0.01 eV. Inset shows the same results on a semilog scale.	53
4-10	Configurations and energy-barriers corresponding to the 4 most frequently selected events during the first 100 s of coarsening.	54
5-1	Diagram showing neighboring sites affecting the energy barrier for intralayer diffusion of a central atom (shaded circle) used in EMT model of Cu/Cu(100) growth (see Eq. 5.1).	62

5-2	Diagram showing some important intralayer moves in EMT Cu(100) model along with corresponding activation barriers. (a) monomer diffusion (b) single-bond edge diffusion and detachment (c) two-bond edge diffusion (d) monomer attachment at a step-edge (e) corner-rounding ($E_c = 0.35$ eV) (f) kink detachment along an edge.	65
5-3	Pathways for edge- and interlayer diffusion in EMT Cu(100) model. Barriers for each process are as follows: (1) $E_a/2$ (2) E_c (3) $3E_a/2+E_{ES}$ (4) $3E_a/2$ (5) $E_a + E_{ES}$ (6) E_a (7) $E_a/2 + E_{ES}$	66
5-4	Schematic showing 1D random walker diffusing between partially absorbing boundaries at 0 and L with absorption probabilities β_0 and β_L respectively.	68
5-5	Example of edge-diffusion with two possible absorption pathways: attachment to a kink with rate D_e , and corner-rounding with rate D_c	70
5-6	Examples of edge-atoms (striped circles) and their corresponding absorption sites (dashed lines) including interactions with monomers, e.g. absorption sites for atom A are A_1 and A_2	74
5-7	Two interacting step-edges. Edge-atoms between sites I and II are treated with regular KMC, while edge-atoms outside this region (e.g. atom A) are treated using FPT KMC.	74
5-8	Schematic showing example of interaction sites (empty circles) associated with edge-diffuser (striped circle).	75

5-9	Comparison of regular KMC results (symbols) and FPT KMC results (lines) for surface roughness obtained from simulations of irreversible growth models at 200 K and 250 K.	78
5-10	Comparison of surface morphology ($L = 256$) obtained in regular KMC (a) and FPT KMC (b) simulations of “generic” fcc model at coverage of 20 ML and regular KMC (c) and FPT KMC (d) simulations of SOS model at 30 ML.	79
5-11	Comparison of regular KMC (symbols) and FPT KMC (lines) results for surface roughness and lateral correlation length (r_c) obtained in simulations using EMT model of Cu/Cu(100) growth at 200 K.	81
5-12	Comparison of surface morphology ($L = 256$) obtained in regular KMC (a) and FPT KMC (b) simulations of EMT model of Cu/Cu(100) growth at coverage of 60 ML.	82
5-13	Comparison of regular KMC (symbols) and FPT KMC (lines) results for surface roughness obtained in simulations using EMT model of Cu/Cu(100) growth at 250 K.	83
5-14	Dependence of surface roughness on edge-reduction factor R obtained in regular KMC simulations of EMT model of Cu/Cu(100) growth at 200 K.	88
6-1	Monomer density N_1 and island density N as a function of coverage θ with $D/F = 3 \times 10^6$ for $\alpha = 0.0, 1.0,$ and 2.0	97
6-2	Peak island density as a function of D/F for $\alpha = 0.0, 1.0,$ and 2.0	98

6-3	Island morphology for coverage $\theta = 0.2$ with $D/F = 3 \times 10^6$ for strains (a) $\alpha = 0.0$ (b) $\alpha = 1.0$ (c) $\alpha = 2.0$ (d) $D/F = 3 \times 10^7$ for strain $\alpha = 2.0$	99
6-4	Average aspect ratio $\langle A_r \rangle$ for $D/F = 3 \times 10^6$ (diamonds) and 3×10^7 (circles) at coverage $\theta = 0.2$ as a function of strain α .	101
6-5	Aspect ratio distribution $P(A_r)$ for coverage $\theta = 0.2$ at $D/F = 3 \times 10^6$ for strains (a) $\alpha = 0.0, 1.0,$ and 2.0 .	102
6-6	Scaled island-width distribution $f_w(w/W)$ for different coverages with $D/F = 3 \times 10^6$, (a) $\alpha = 0$ (b) $\alpha = 1.0$	104
6-7	Scaled island-length distribution $f_l(l/l_{pk})$ for different coverages with $D/F = 3 \times 10^6$, (a) $\alpha = 0$ (b) $\alpha = 1.0$	105
6-8	Scaled island-size distribution with $D/F = 3 \times 10^7$, $\alpha = 2.0$ and cov- erages ranging from $\theta = 0.05$ to $\theta = 0.2$.	106
6-9	Scaled island-size distribution with $D/F = 3 \times 10^7$ at coverage $\theta = 0.1$ for $\alpha = 0, 1.0$ and 2.0 .	107
C-1	Illustration of statistics used to describe rough surface. Mean height \bar{h} , interface width w , lateral correlation length ξ	128
C-2	The typical graph of the height-height correlation function $G(r)$	132

List of Tables

3.1	Comparison of efficiencies of parallel algorithms with $N_p = 2$ and $L = 1024$. The cycle time τ used for the SL algorithm is given in parentheses. f_R is the fraction of roll-back events per cycle in the OSR and OSRPR algorithms.	35
3.2	Comparison of efficiencies of parallel algorithms with $N_p = 4$ and $L = 1024$	36
5.1	Parameters used for “generic” fcc(100) and SOS models. Here D is the total rate for monomer diffusion, while D_e and D_c are the rates of edge-diffusion and corner-diffusion respectively.	80
5.2	Speed-up factors (compared to regular KMC) obtained in FPT KMC simulations of multilayer growth at $T = 200$ and 250 K using different models with Cu parameters.	84

Chapter 1

Introduction

1.1 Simulations of Thin Film Growth

Understanding and controlling the evolving surface morphology of epitaxial thin films is of immense technological interest. Work in this field has been motivated by the ever more stringent requirements on the quality of thin films needed for developing advanced microelectronic, optical, and magnetic devices, as well as the thrust toward nanometer- scale structures. As device miniaturization reaches sub-micrometer- and nanometer-length regimes, atomic-level control of the fabrication processes for both novel materials and new devices is becoming crucial. Depending on the application, one may wish to produce either atomically flat or nanostructured surfaces. However, in each case the performance depends critically on the surface morphology as well as on the underlying film structure.

A wide range of physical phenomena, from the molecular scale to galactic, may be studied using some form of computer simulation. Computer simulations of materials

behavior are an important component of materials science research because measurements are indirect, requiring theoretical interpretation. The main aim of the research in this field is to predict and control the morphology of the films by tuning the material composition and growth conditions. A model study of film growth typically involves deposition of a controlled amount of atoms onto a substrate in a prescribed set of growth conditions. The precisely defined growth conditions make it possible to decipher, at an atomic level, the rules governing the evolution of the growth front, and to explore ways to tailor film morphology to obtain specific characteristics.

Thin film growth involves a large range of time scales, with the detailed atomistic motions operating in a regime of $10^{-12} - 10^{-15}$ sec , while a typical time scale for the formation of an atomic layer of atoms is of the order of 1 sec -1 min. Thus, a continuing challenge in thin film growth simulations is to reach experimentally relevant time and length scales while keeping simulations as realistic as possible.

1.2 The scope of this thesis

In this thesis we have developed new methods to extend the time and length scales of kinetic Monte Carlo (KMC) simulations and successfully applied these methods to carry out realistic simulations of epitaxial thin-film growth.

In **chapter 2**, we first introduce the Monte Carlo method and briefly discuss different types of existing Monte Carlo methods used in thin film growth simulations. In addition, we will give a brief description of one of the newly developed on-the-fly KMC methods referred to as the self-learning kinetic Monte carlo method. In this

method, a fixed catalog of processes is replaced by the continuous identification of possible activated processes on the fly making KMC simulations more realistic.

In **chapter 3** we discuss a variety of algorithms for parallel kinetic Monte Carlo including the recently developed optimistic synchronous relaxation (OSR) algorithm as well as the semi-rigorous synchronous sublattice (SL) algorithm. A variation of the OSR algorithm corresponding to optimistic synchronous relaxation with pseudo-rollback (OSRPR) is proposed. In addition, a dynamic boundary allocation (DBA) method for improving the parallel efficiency by reducing the number of boundary events is proposed. A variety of other methods for enhancing the efficiency of our simulations are also discussed. These methods are then applied to study the coarsening of Ag(111) submonolayer islands at room temperature. We note that, because of the relatively high temperature of our simulations, as well as the large range of energy barriers (ranging from 0.05 eV to 0.8 eV), developing an efficient algorithm for parallel KMC and/or SLKMC simulations is particularly challenging. However, by using DBA to minimize the number of boundary events, we have achieved significantly improved parallel efficiencies for the OSRPR and SL algorithms. Finally, we note that, among the three parallel algorithms which we have tested here, the SL algorithm with DBA yielded the highest parallel efficiency. As a result, we have obtained reasonable parallel efficiencies in our simulations of room-temperature Ag(111) island coarsening for a small number of processors (e.g. $N_p = 2$ and 4). Since the SL algorithm scales with system size for fixed processor size, we expect that comparable and/or even larger parallel efficiencies should be possible for parallel KMC and/or SLKMC simulations of larger systems with larger a number of processors.

In **chapter 4**, we present the results of parallel KMC simulations of Ag(111) island coarsening at room temperatures carried out using a very large database obtained via self-learning KMC simulations. Our results indicate that, while cluster diffusion and coalescence play an important role for small clusters and at very early times, at late time the coarsening proceeds via Ostwald ripening, i.e. large clusters grow while small clusters evaporate. In addition, an asymptotic analysis of our results for the average island size $S(t)$ as a function of time t leads to a coarsening exponent $n = 1/3$ (where $S(t) \sim t^{2n}$), in good agreement with theoretical predictions. However, by comparing with simulations without concerted (multi-atom) moves, we also find that the inclusion of such moves significantly increases the average island size. Somewhat surprisingly we also find that, while the average island size increases during coarsening, the scaled island-size distribution does not change significantly.

In **chapter 5**, a first-passage-time (FPT) approach to accelerate kinetic Monte Carlo (KMC) simulations of metal(100) epitaxial growth with fast edge diffusion is described. In our approach, the process of (one-bond) edge-diffusion is replaced by an analytical expression for the first-passage time for an edge-diffuser to be absorbed either by corner-rounding or kink-attachment, while the remaining activated processes are treated with regular KMC. As a test of this approach we have studied three different models of multilayer growth, including two irreversible growth models as well as an effective-medium theory (EMT) model of Cu/Cu(100) growth. By taking into account the differences in hopping rates at boundaries and including interactions of edge-diffusers with other atoms we have obtained very good agreement between our FPT KMC and regular KMC simulations. In addition, we find that our FPT

approach can lead to a significant speed-up compared to regular KMC simulations. Finally, in Appendix B.3 expressions for the conditional first-passage time are also derived

In **chapter 6** the effects of strain on the island morphology and size distribution in irreversible submonolayer growth with rapid island relaxation are investigated. In our simulations the strain energy is approximated by an isotropic $1/r^3$ interaction. While the island density increases with strain, in the presence of sufficient island relaxation due to edge diffusion, the island shape changes from square to rectangular. However, due to fluctuations, there is a broad distribution of island widths. General scaling forms for the island width and island length distributions are derived and good scaling is obtained as a function of coverage while there is only a relatively weak dependence on the strain. The scaled island-size distribution is also found to be only weakly affected by strain. These latter results are in qualitative agreement with recent experimental results for InAs/GaAs(100) growth.

Chapter 2

Monte Carlo Methods

2.1 Introduction to Monte Carlo Methods

While a variety of models have been developed to study the evolution of the surface morphology and thin-film microstructure during the growth process, most of these models are classified into three basic approaches: (i) stochastic continuum equations, (ii) simple discrete models, and (iii) more realistic atomic scale models. However, in order to get a full understanding of the growth process, more realistic atomic scale models are needed. In particular, we will focus on kinetic Monte Carlo (KMC) and modifications to it, to make KMC simulations as realistic as possible.

There are essentially two approaches to performing molecular simulations: stochastic and deterministic. The stochastic approach is called Monte Carlo (MC) and the deterministic approach, called Molecular Dynamics (MD). If the interaction potential is known, then MD simulations are the most accurate atomistic simulation technique. Using this method the dynamics of a many-body system can be modeled by numeri-

cally solving the differential equations of motion for all atoms involved. This enables us to determine statistical averages of the static and dynamical physical properties. Hence, in MD simulations, the positions are deterministic and connected in time. However, it is difficult to accommodate the motions of all atoms accurately on the basis of a deterministic model, since the space and time intervals required are much longer than the length and time scales available in MD simulations (typically from ps to μs). In addition, it is difficult for MD to handle events that occur with vastly different rates or probabilities. This problem limits the scope of dynamical MD simulations involving interacting atoms, particles, or molecules [1]. Fortunately, there exists another method, the Monte Carlo (MC) method, for evaluating the properties of complex, many-body systems [1, 2, 3]. In this method a detailed knowledge of the exact positions of atoms and their velocities is sacrificed in favor of a more coarse-grained approach which takes into account the time-evolution of the system from one energy minimum or basin to another. Using this method, time scales significantly larger than those typically studied in MD can be used. In MC simulations the positions are generated stochastically such that an atomic configuration depends only on the previous configuration [4].

2.2 Metropolis Monte Carlo

2.2.1 Markov Chains

Before proceeding to Markov chains, we introduce *truly random* or *uncorrelated chains*, in which the probability of occurrence of a particular sequence of the system which transits from its initial state x_i to its final state x_f is statistically uncorrelated [2]:

$$P(x_i, x_{i+1}, \dots, x_{f-1}, x_f) = P_1(x_i)P_1(x_{i+1})\dots P_1(x_f) \quad (2.1)$$

where $P_1(x)$ is independent probability of occurrence for the state x . In contrast, a Markov chain is a correlated sequence of random events whose probability densities at a time interval depend upon the previous states of the system. It is defined in terms of a system with a set of transition probabilities $W(x_a \rightarrow x_b)$ to have state x_b succeed state x_a in the sequence. The probability of having a sequence of states x then may be written as:

$$P(x_i, x_{i+1}, \dots, x_{f-1}, x_f) = P_1(x_i)W(x_i \rightarrow x_{i+1})W(x_{i+1} \rightarrow x_{i+2})\dots W(x_{f-1} \rightarrow x_f) \quad (2.2)$$

Now we introduce the time evolution of the transition probability $P(x, t)$ of the system in state x . This evolution of dynamical transition probability $P(x, t)$ is quite intuitive and is given by a Markovian master equation [1].

$$\frac{\partial P(x_f, t)}{\partial t} = \sum_{x_i} W(x_i \rightarrow x_f) P(x_i, t) - \sum_{x_f} W(x_f \rightarrow x_i) P(x_f, t) \quad (2.3)$$

and $W(x_i \rightarrow x_f)$ Here $P(x, t)$ is the probability that a system is in state x at time t and $W(x_i \rightarrow x_f)$ is the transition probability per unit time that the system will transit from state x_i to state x_f .

The controlling factor in a Markov chain is the transition probability. The probability is a conditional probability for the system to transit or migrate to a particular new state, given the current state of the system. For many situations, such as the case in which the system is at thermal equilibrium (steady state), the occupation probability is weighted according to the Boltzmann distribution,

$$P_i \propto e^{-E_i/k_B T} \quad (2.4)$$

where E_i is the energy of state i , T is the temperature, and k_B is Boltzmann's constant.

At the steady state, the sum of all transitions into a particular state x equals the sum of all transitions out of the state. To be consistent with the Boltzmann distribution in equilibrium, the *detailed-balance criterion* must be imposed on the MC transition probabilities. The *detailed-balance criterion* may be expressed as [1]

$$W(x_i \rightarrow x_f) P(x_i, t = \infty) = W(x_f \rightarrow x_i) P(x_f, t = \infty) \quad (2.5)$$

However the *detailed balance criterion* does not uniquely determine the transition

probability $W(x_i \rightarrow x_f)$ but leaves an ambiguity in the choice of W [5].

2.2.2 Metropolis Algorithm

To evolve a system towards equilibrium or evaluate thermodynamic averages of the system, one can apply MC method with importance sampling. The desired importance sampling may be obtained by the Markov chain. This means that estimates could be quite efficient if the proper transition probabilities can be determined. There are many methods used to select the prior transition probabilities. One often used is the *Metropolis algorithm* given by:

$$W(x_i \rightarrow x_f) = \begin{cases} \frac{1}{\tau} e^{-\delta E/k_B T} & \text{for } \delta E > 0 \\ \frac{1}{\tau} & \text{Otherwise} \end{cases} \quad (2.6)$$

For Metropolis, τ is the usual MC step, and $\delta E = E(x_f) - E(x_i)$ the energy difference. The detailed procedure of the Metropolis algorithm may be outlined as [5, 3]:

- Produce a new state from the current state by using a uniform random number
- Calculate the energy difference δE between the new state and the current state.
- if $\delta E \leq 0$, update to new state.
- if $\delta E > 0$, generate a uniform random number $\nu \in [0,1]$.
 1. if $e^{\delta E/k_B T} > \nu$, update to new state.
 2. else, no update.

- Go to first step and repeat

A Monte Carlo simulation using such Metropolis algorithm is often called as Metropolis Monte Carlo simulation.

2.3 Kinetic Monte Carlo

In many materials, the dynamical evolution occurs through a series of “rare events”, in which the system spends a long time period in one potential-energy minimum before escaping and moving on to another. Since the localized motion in the potential-energy minima is not significant, the dynamical evolution can be simulated as a series of jumps between potential-energy minima. This is the aim of kinetic Monte Carlo (KMC) simulations.

Kinetic Monte Carlo (KMC), sometimes called dynamic MC [6], is an extremely efficient method for carrying out dynamical simulations of a wide variety of stochastic and/or thermally activated processes when the relevant atomic-scale processes are known. In KMC, the system is evolved using a stochastic algorithm that directly takes into account the physical energy barriers that govern the evolution of a system and that translates to a real time scale[1]. Importantly, the KMC time for a given step will be scaled by the average time required to observe the particular stochastic event chosen to occur at that time step. Thus, each KMC time step will have widely different magnitudes depending on the temperature, energy-barrier and so on.

Single-processor (serial) KMC simulations have been used to model a variety of dynamical processes ranging from catalysis to thin-film growth. In this section, we

first introduce the basic algorithm of KMC, then deal with models of crystal growth using KMC.

2.3.1 KMC Algorithm

The KMC algorithm is based on the so called “n-fold-way” [1, 7]. This algorithm for KMC is also known as Bortz-Kalos-Lebowitz(BKL) or *residence-time* algorithm.

This algorithm may be outlined as the following procedure:

1. Set the start time $t = 0$.
2. Update list of all possible events (transitions) that can occur and rates for each event in the system: assume each event ‘ i ’ has rate $R_i \propto e^{-E_b/k_B T}$, where E_b is the barrier energy.
3. Calculate the partial cumulative event rates (partial sums)

$$S_i = \sum_{j=1}^i R_j$$

for $i = 1, \dots, N$ where N is the total number of events. Denote $S_0=0$ and the total event rate $R_T = S_N$.

4. Get a uniform random number $P_j \in [0,1]$.
5. Select event j to occur with probability

$$S_{j-1}/R_T < P_j \leq S_j/R_T$$

6. Perform j .
7. Update time $t = t - \ln(r)/R_T$ where $0 < r < 1$ is uniform random number.
8. Go to 2 and repeat.

Because there is a thermally activated diffusion move or a deposition event in every loop of the program, KMC is a very efficient method, and can bridge the gap of time scales between relatively fast thermal diffusion processes and rare deposition events. However, one of the major disadvantage of KMC is that all parameters, such as the event rates R_i , have to be known in advance. This method itself can do nothing to predict them. Thus, they can only be obtained from experimental data, or derived from other simulation methods such as MD simulations or *ab initio* calculations. Despite this limitation, KMC remains the most powerful approach available for making dynamical predictions at the mesoscale.

2.3.2 Binary tree Search Algorithm

The search algorithm described above clearly scales as $O(N)$ where N is the total number of events, since step 3 has a sum over N elements. Using a binary-tree, it is possible to reduce the scaling below N , even down to $O(\log_2 N)$.

1. Update the list of all possible event types (transition) that can occur and rates for each event type in the system. Assume each type i has event number n_i with R_i .

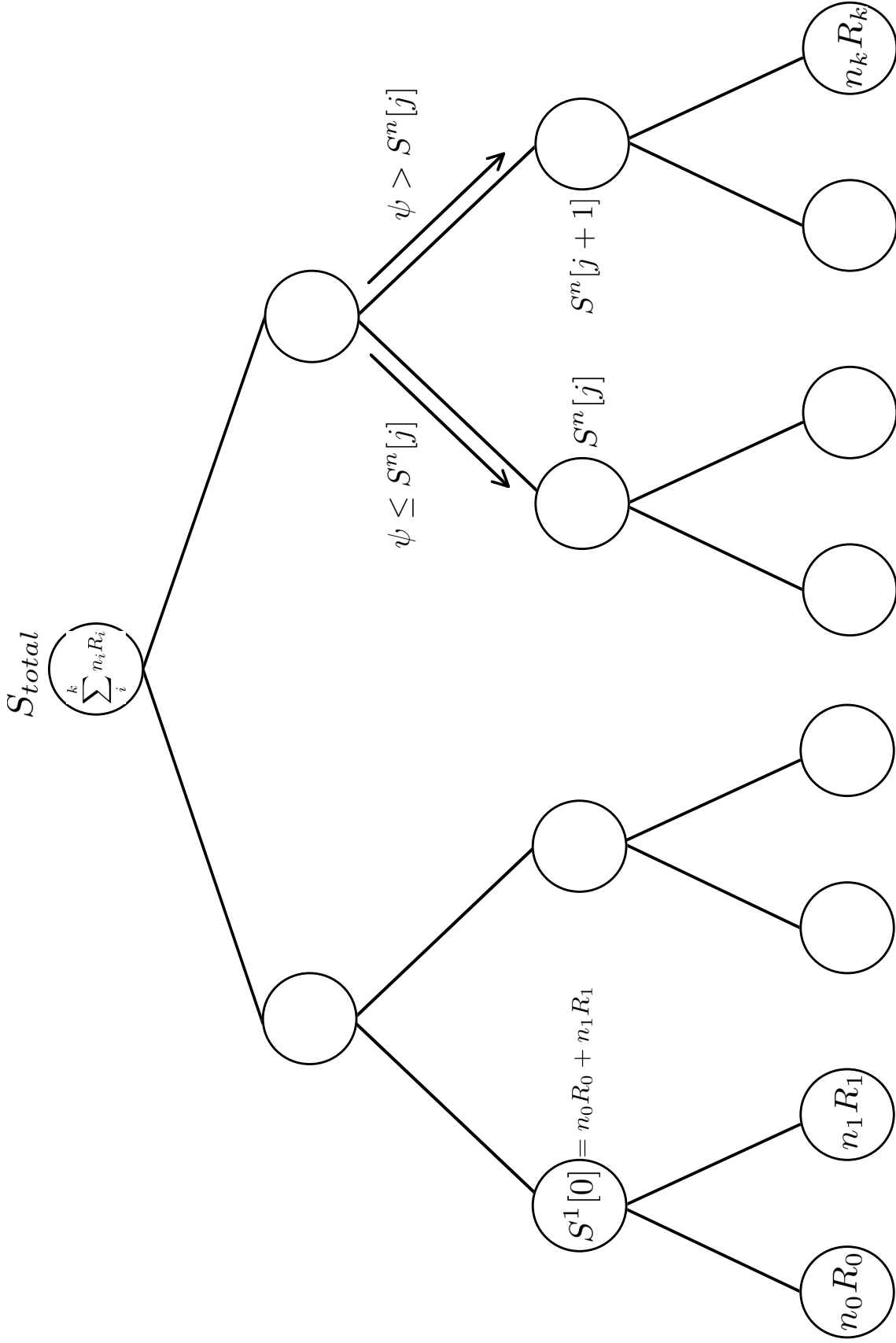


Figure 2-1: A binary tree, transition rates for events of the same type are stored in the leaves and cumulative rates stored at higher levels. The arrows indicate the direction of descent when choosing the type of an event to be executed. The highest node contains the total rate of the system S^{total}

2. Construct a binary tree where each node contains the sum of the rates below the node (see fig 2-1) and the lowest level nodes (leaves) contain the sums of the rates for the events of the same type: $S^0[i] = n_i R_i$. The root node the tree $S_{total} = S^k[0]$ has total rate of the entire system at all times, where k is the number of levels or total depth of the binary tree.
3. Generate a random number $\psi \in [0, S_{total}]$ and start from the root of the tree ($n = k, i = 0$).
4. Compare the number ψ with the left branch $S^{n-1}[2i]$
5. If $\psi \leq S^{n-1}[2i]$, descend to the left branch $n \rightarrow n - 1, i \rightarrow 2i$ (see fig 2-1) and continue to 4.
6. If $\psi > S^{n-1}[2i]$, update the random number $\psi \rightarrow \psi - S^{n-1}[2i]$ and descend to the right branch $n \rightarrow n - 1, i \rightarrow 2i + 1$ (see fig. 2-1) and then continue to 4.
7. If the lowest level $n = 0$ (leaves of the tree) is reached then i gives the type of picked event.
8. Another random number is generated $u \in [0, n[i]]$ and perform the event j for which $n^{j-1} < u \leq n^j[i]$.
9. Update the tree.

The binary tree search algorithm is more efficient than the n-fold way algorithm in large systems with many different kinds of objects and possible events.

2.4 On-the-Fly/Self Learning Kinetic Monte Carlo

2.4.1 Introduction

One of the limitations of KMC simulations is the reliance on an *ad hoc* choice of processes. If this input is accurate and complete, KMC simulations will give accurate results. Standard KMC simulations are performed with a set of the most obvious simple atom or concerted processes as input, and all others are ignored or included in approximate ways or in an *ad hoc* manner to fit experimental data. For these reasons and also because of experimental observations of complex and unforeseen processes, simulation with an *a priori* chosen catalog process needs to be replaced by a continuous identification of possible processes as the environment changes. This is the motivation behind On-the-fly KMC [8, 9, 10], to replace a chosen catalog of processes by finding all possible processes on the fly making KMC simulations more realistic.

One such recently developed technique to address the completeness issues of KMC is the self-learning KMC method (SLKMC) [10, 11]. In an SLKMC simulation, rather than use a fixed catalog of processes and their corresponding activation barriers, the activation barriers corresponding to new configurations not already included in the database are obtained on the fly. The resulting processes are then added to the SLKMC database. A pattern recognition scheme is used to identify configurations. This allow efficient storage and subsequent retrieval of information from the database of diffusion processes, their paths, and their activation energy barriers thus making it efficient and reliable.

2.4.2 Self Learning KMC Algorithm

As mentioned earlier the aim of SLKMC is to replace an *ad hoc* list of processes with the identification of processes on the fly. To identify different processes, SLKMC needs to identify the local environment of undercoordinated atoms during the course of the simulation. Then by carrying out MD simulations and using the nudged elastic band (NEB) method to determine activation energies, or alternatively using the less powerful “drag” method [10] the relevant activated processes for a given configuration can be determined. A pattern recognition scheme is then used to store them and for subsequent usage in the simulations. Pattern recognition described here is for an fcc(111) surface with six fold symmetry. Any process is assumed to involve a central atom and atoms in the next two shells(or three rings depending on the system) as illustrated in Fig. 2-2. The motif in Fig. 2-2 serves as cookie cutter and is placed on all active atoms. A process may be described as central atom moving to a neighboring vacancy accompanied by the motion of any other atoms or atoms in the surrounding shells. To uniquely indentify local environments each shell is given a ring number. This ring number is derived as a binary number based on locations of atoms in the shell and then converted to a decimal number as shown in Fig. 2-2, which is self explanatory. The same procedure is followed for atoms in the other outer shells. Hence for an atom to be active (i.e., the central atom for a given process), it should have a vacancy in its first shell (or occupancy number less than 63)

Once the atoms are classified as active and non active and encrypted with the

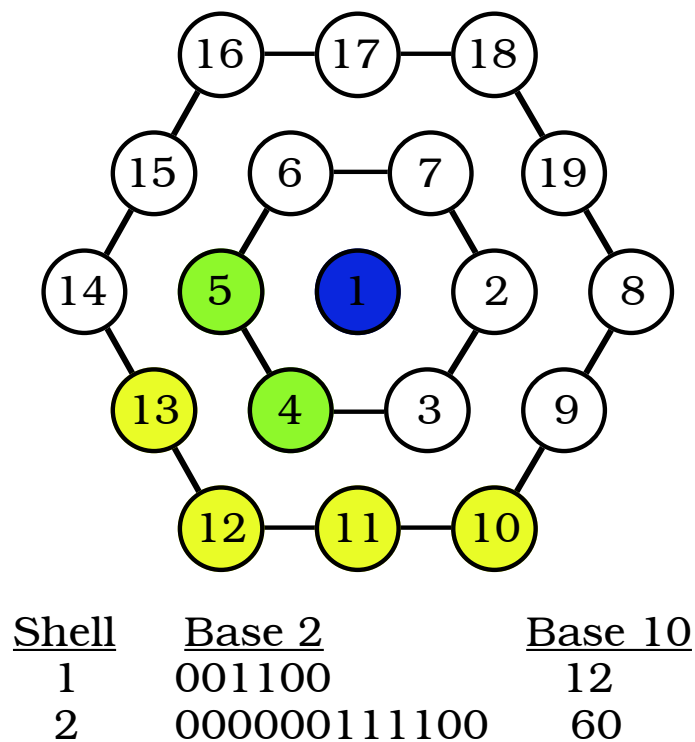


Figure 2-2: Two-shell indexing around central atom labeled 1

shell scheme all possible active atoms are determined. Fig. 2-3 shows a configuration with ring numbers (12,60), first and second number respectively. Fig. 2-3 also shows how processes are labeled and stored in the database and also an example of multiple atom process. Here central atom labelled 1 moves to a vacant site 2 along with atoms at sites 5, 4 and 13. The activation energy barrier for this process is found to be 0.373eV. Fig. 2-3 also shows other possible processes for that configuration along with their activation energies for those processes.

In standard KMC simulations these energy barriers are provided as input. But with SLKMC these barriers are calculated on the fly. These activation barriers are stored and tagged to atomic processes in the database. Self-learning is achieved by the system through the ability to (1) calculate activation energies on the fly, (2) store

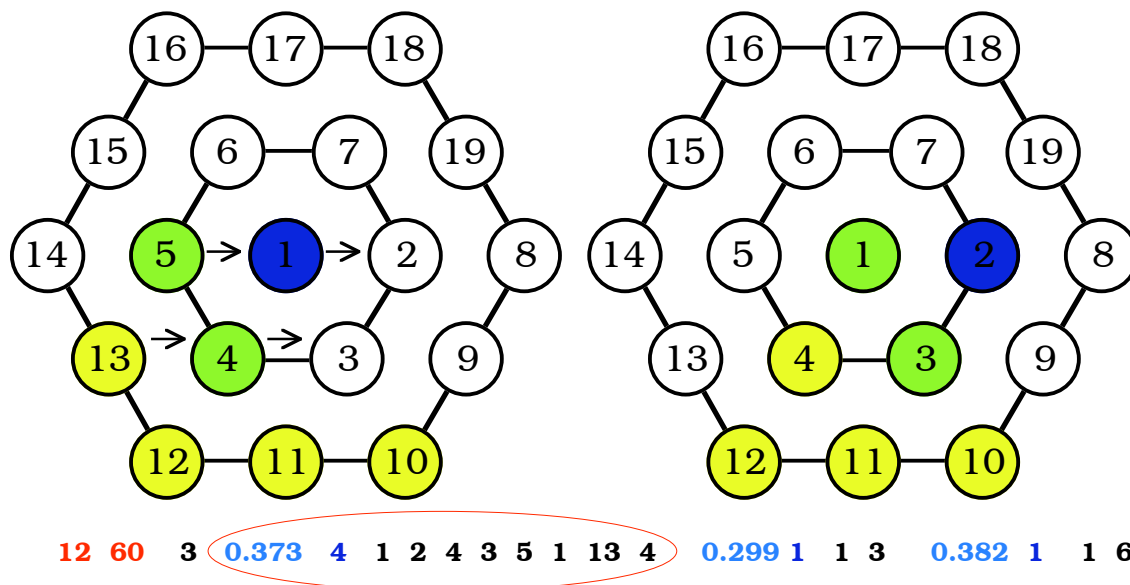


Figure 2-3: Example of a multiple atom process and also shows how a configuration is stored in the database.

them in a database and (3) recognize and retrieve them using the labeling described above. If a new process is encountered, actual calculation is performed and then added to the database.

In order to minimize the size of the database we have also used the symmetry of the fcc(111) surface. In particular, the following 5 symmetry operations were used: (1) 120° rotation (2) 240° rotation (3) mirror reflection (4) mirror reflection followed by 120° rotation and (5) Mirror reflection followed by 240° rotation. Thus, if a given configuration was not found in the database, then the symmetry operations mentioned above were performed and used to identify the configuration in the database. If it is still not found in the database then actual calculation is done to find paths and their corresponding barriers and these are then added to the database. Fig 2-4 shows an example of 120° rotation symmetry operation.

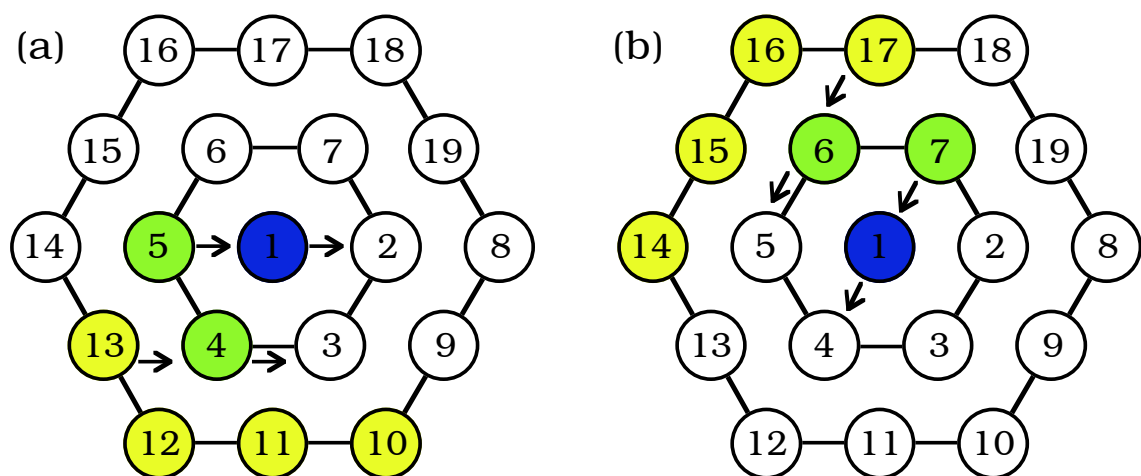


Figure 2-4: Example of 120° rotation symmetry operation showing two symmetry related configurations (a) and (b).

Chapter 3

Algorithms for Parallel Kinetic Monte Carlo

3.1 Introduction

Since the time of the next event is determined by the total overall rate for all processes, both the standard kinetic Monte Carlo method and SLKMC are serial algorithms, i.e. only one event can occur at each step. However, in some cases one needs to simulate larger length and/ or time scales than can be simulated using a serial algorithm. Therefore, it is desirable to develop efficient parallel kinetic Monte Carlo algorithms in order to extend the range of time and/or length scales over which realistic simulations can be carried out.

A number of different algorithms for parallel KMC have been studied and applied to simulations of thin-film growth. These include the synchronous relaxation (SR)

algorithm [12, 13, 14], the optimistic¹ synchronous² relaxation algorithm (OSR) [16] and the semi-rigorous synchronous sub-lattice (SL) algorithm [17]. The SL algorithm [17] has been shown to provide good parallel efficiency in simulations of variety of simplified models of nucleation and thin film growth. Due to the fact that it only requires local communications, the SL algorithm also scales with system size, e.g. for a fixed processor size the simulation time is independent of the number of processors.

We note that this work is part of a larger project to develop parallel algorithms to carry out realistic SLKMC simulations over larger time- and length-scales. Therefore, in addition to presenting results for the coarsening of Ag(111) islands in chapter 4 we also present results for the efficiency and accuracy of a number of different algorithms applied to Ag(111) island coarsening. In particular, we discuss the optimistic synchronous relaxation (OSR) algorithm, the optimistic synchronous relaxation with pseudo-rollback (OSRPR) algorithm, the synchronous sub-lattice (SL) algorithm as well as a number of improvements such as dynamic boundary allocation (DBA). We note that processes in the database have a very large range of event rates (see Fig. 4-3) (ranging from $4 \times 10^3 \text{ s}^{-1}$ for double-bond detachment from an island to $8 \times 10^{10} \text{ s}^{-1}$ for monomer hopping). As a result, developing an efficient algorithm for parallel KMC and/or SLKMC simulations is particularly challenging. However, our results indicate that by using the SL algorithm along with dynamic boundary allocation to increase the cycle time and thus reduce communication overhead, a reasonable parallel efficiency can be achieved.

¹Optimistic approach uses a *detection and recovery* approach [15]: causality errors are detected, and a *rollback* mechanism is invoked to recover.

²All processors are ‘in synch’ at the beginning and after each cycle.

3.2 KMC Algorithm

In order to maximize the efficiency of our simulations we have used a binary tree algorithm [18] combined with lists. In particular, at the beginning of our simulation we scan through the lattice and identify the configurations for every occupied site to determine the corresponding moves and activation barriers for each configuration. Based on this information we create an array of lists, where each list corresponds to one of the 4712 different possible mechanisms for activated events, and contains all the central atom locations corresponding to that type of event. The total rate for each type of move (corresponding to the rate for that move times the number of central atoms of that type) is calculated and placed at the “base” of a binary tree. We then generate a random number (between 0 and the total rate for all events) and use the binary tree structure to efficiently select the list “type” of the next move, while the particular move is randomly selected from the selected list. After each transition, the neighborhood of each changed site is updated along with the associated lists as well as the total rate and binary tree. This leads to a code which is efficient and scales with system size.

We note that all our simulations were carried out using the 1.4 Ghz Itanium Cluster at the Ohio Supercomputer Center (OSC). By replacing a “standard” KMC by one which uses a binary tree with lists as described above, as well as replacing a linear search through the database with a matrix (described in Sec. 4.2), we were able to significantly reduce the average time per KMC step from 592.8 μ s in our initial code to 24.6 μ s. For comparison, we note that in a typical KMC with a small number

of different event types such as edge- and/or corner-diffusion the corresponding time is typically 6 μ s or less.

3.3 Parallel Algorithms for the kinetic Monte Carlo

Method

3.3.1 Optimistic Synchronous Relaxation (OSR) Algorithm

One of the first rigorous algorithms for parallel discrete-event³ simulations was the synchronous relaxation algorithm developed by Lubachevsky [12]. We note that the application of this algorithm to KMC simulations as well as its scaling as a function of the number of processors N_p has been recently studied by Shim and Amar [14]. However, since this algorithm is relatively complex and requires multiple iterations for each cycle, Merrick and Fichthorn have recently developed a similar but simpler algorithm which they refer to as optimistic synchronous relaxation (OSR) [16].

Fig. 3-1 shows a typical decomposition of a square system into N_p square regions, where N_p is the number of processors. Also indicated in Fig. 3-1 are the boundary and “ghost” regions for the central processor, where the boundary region is defined as that portion of the processor’s domain in which a change may affect neighboring processors. Similarly, the ghost region corresponds to that part of the neighboring processors’ domains which can affect a given processor. Thus, in general the width

³A discrete event simulation model assumes that system being simulated only changes state at discrete points in simulated time. The simulation model jumps from one state to another upon the occurrence of an event.

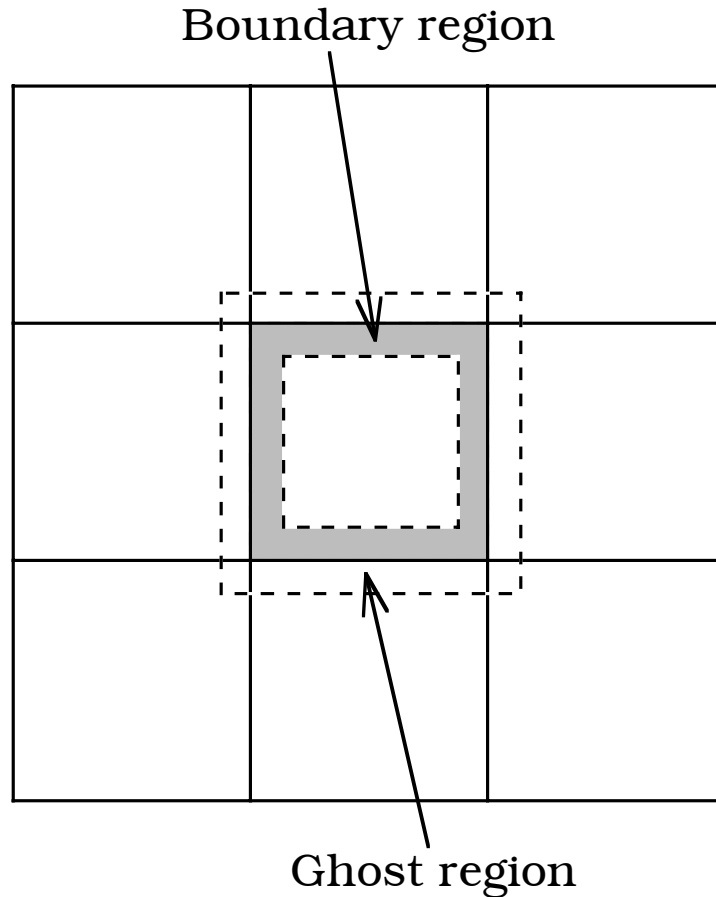


Figure 3-1: Schematic diagram of square decomposition for $N_p=9$. Solid lines correspond to processor domains

of the boundary and ghost regions must be at least equal to the range of interaction.

As shown in Fig. 3-2, in the OSR algorithm in each cycle all processors start with the same initial time and then simultaneously and independently carry out KMC events in their domains until either the number of KMC events reaches a pre-determined fixed number G , or one of the events corresponds to a “boundary event”, i.e. an event which modifies the boundary region of the given processor, and which can thus affect events in neighboring processors. Defining the time for the last event in each processor as t_{last} , a global communication is then carried out to determine the time t_{min} corresponding to the minimum of t_{last} over all processors. Each processor

then “rolls back” or undoes all KMC events which occur after t_{min} . If there are no boundary events then the processors all move on to the next cycle with the new starting time corresponding to t_{min} and all events after that time are rolled back. However, if t_{min} corresponds to a boundary event, then an additional communication is needed to update the ghost and/or boundary regions of all processors affected by the boundary event.

We note that typically the OSR algorithm requires 2 – 3 global communications each cycle, one to determine t_{min} , another to determine if the event with t_{min} corresponded to a boundary event, and a third to update the boundary regions of the affected processors if there was a boundary event. To reduce the number of global communications we have encoded the processor identity as well as whether or not the last event was a boundary event, along with the least advanced time of each processor in a single floating point number before doing a global communications to determine t_{min} . This was done by replacing t_{last} with a number whose most significant figures corresponded to t_{last} but whose least significant figures contained information about the processor ID and whether or not that processor had a boundary event ⁴. Thus, in our implementation of the OSR algorithm only one global communication was needed if t_{last} corresponded to a non-boundary event, while two communications were needed if it was a boundary event.

⁴ In this method, the time each processor advances from its previous cycle is multiplied by a very large number to form the integer part of the double precision packed number. The ratio of the processor ID to the total number of processors used N_p is then added to the decimal part if there is a boundary event in that processor. If there is no boundary event in that processor a decimal number is added such that it does not correspond to any processor identity. In our implementation the multiplying number was 10^{20} , which leads to good accuracy.

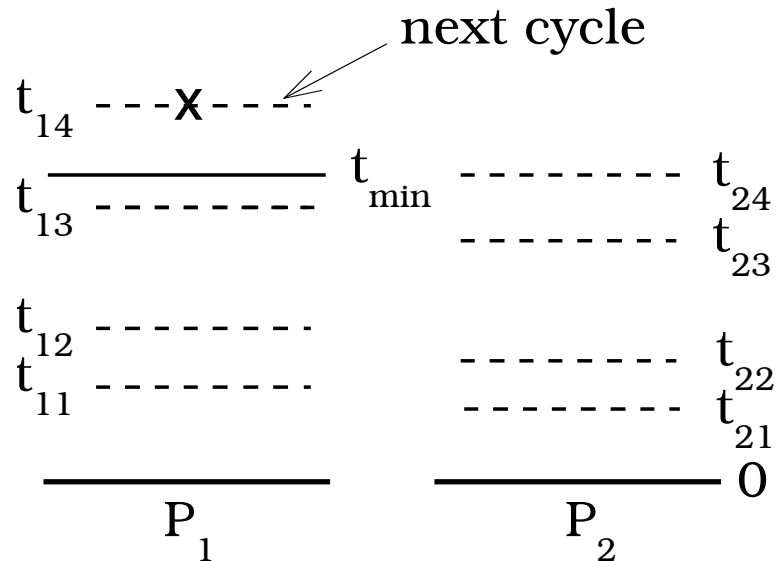


Figure 3-2: Time evolution of events for OSR and OSRPR algorithms with $G = 4$. Dashed lines correspond to selected events, while the dashed line with an **X** corresponds to an event exceeding t_{\min} (see text). In OSR this event is discarded while in OSRPR this event is added to the next cycle.

We note that in the OSR algorithm for a given configuration there is an optimal value of G which takes into account the tradeoffs between communication time (which is wasted if there are no boundary events) and rollbacks. While in general, an adaptive method could be used to attempt to optimize the value of G from cycle to cycle, in practice we have found it more efficient to simply use trial and error to find the optimal fixed value of G for our simulation (see Sec. 3.3.4).

3.3.2 Optimistic Synchronous Relaxation with Pseudo-Rollback (OSRPR) Algorithm

In the OSR algorithm each processor discards all KMC events which occur after t_{\min} . However, this is unnecessary if there are no boundary events in any of the processors. Therefore, we have considered a variation of the OSR algorithm (optimistic

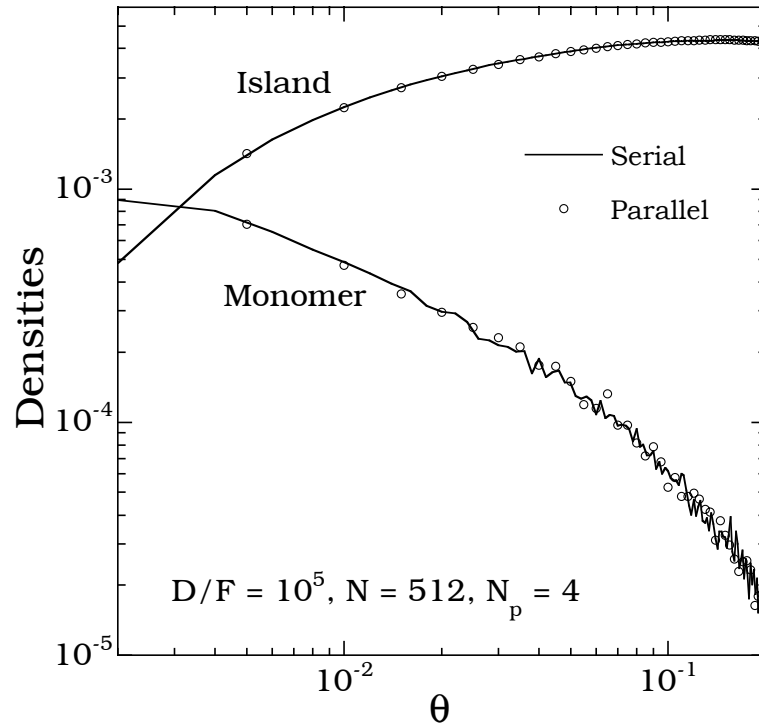


Figure 3-3: Comparison between parallel results using the OSRPR algorithm with square decomposition ($N_p = 4$) and serial results for fractal model with $D/F = 10^5$ and $G = 7$.

synchronous relaxation with pseudo-rollback [19]) in which, when there are no boundary events in the system, those events that would have been discarded are added to the next cycle. This can reduce the loss of computational time due to undoing and then ‘redoing’ events and thus enhance the computational efficiency. As a test of the OSRPR algorithm, we have carried out parallel simulations using this algorithm for a ‘fractal’ model of irreversible submonolayer growth in which only monomer deposition and diffusion processes are included [14], with $N_p = 4$. As expected, there is excellent agreement between serial and parallel results for the island and monomer densities (see Fig. 3-3).

3.3.3 Synchronous Sublattice (SL) Algorithm

In order to maximize the parallel efficiency we have also carried out simulations using the semi-rigorous synchronous sublattice (SL) algorithm recently developed by Shim and Amar [17]. To avoid conflicts between processors, in the SL algorithm each processor domain is divided into subregions or sublattices (see Fig. 3-4). A complete synchronous cycle corresponding to a cycle time τ is then as follows. At the beginning of a cycle, each processor's local time is initialized to zero. One of the sublattices (A or B) is then randomly selected so that all processors operate on the same sublattice during the cycle. Each processor then simultaneously and independently carries out KMC events in the selected sublattice until the time of the next event exceeds the time interval τ (see Fig. 3-5). The processors then communicate any necessary changes (boundary events) with their neighboring processors, update their event rates, and move on to the next cycle using a new randomly chosen sublattice. We note that in order to ensure accuracy, the cycle time must typically be less than or equal to the inverse of the fastest possible single-event rate in the system [17].

Since it only requires local communication, the scaling behavior of the SL algorithm is significantly better than for the OSR and OSRPR algorithms. As a result, it has been shown to be relatively efficient in parallel KMC simulations of a variety of models of growth [17, 20] and island coarsening [21]. In addition, while it is not exact, in simulations of a variety of models [17, 20, 21] it was found that unless the processor size is extremely small (smaller than a “diffusion length”) or the cycle time

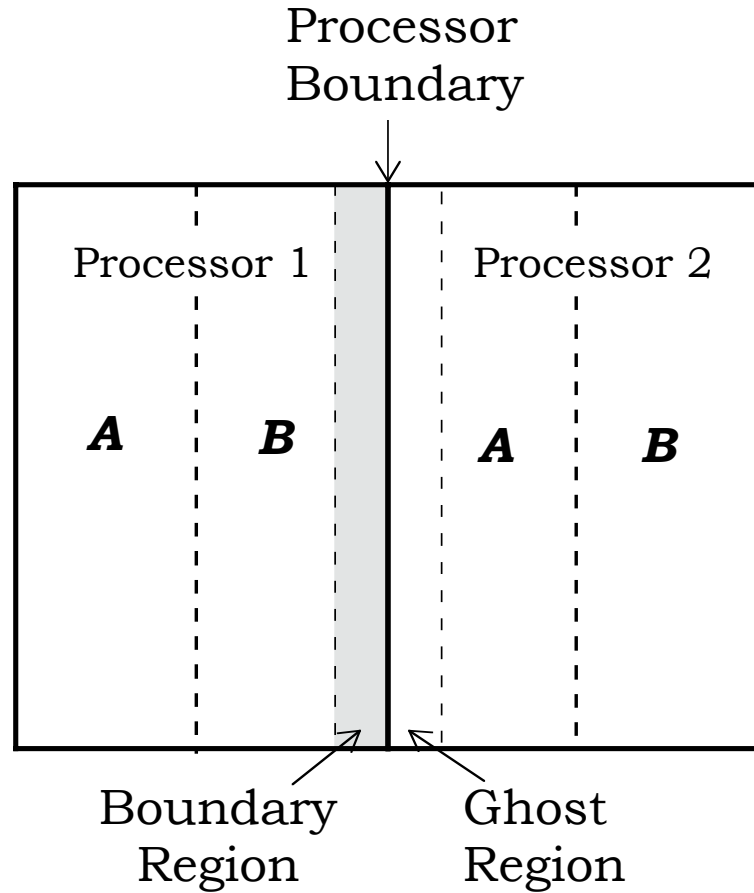


Figure 3-4: Schematic diagram of strip decomposition for $N_p = 2$. Each processor domain is subdivided into A and B sublattices. Boundary and ghost regions for B sublattice of processor 1 are also shown.

is too large, there is essentially perfect agreement between the results of parallel simulations using the SL algorithm and serial simulations. Furthermore, while the cycle time must typically be smaller than the inverse of the fastest possible single-event rate in the system [17], it has recently been shown [21] that in simulations of coarsening significantly longer cycle times can be used, thus decreasing the overhead due to communications and increasing the parallel efficiency.

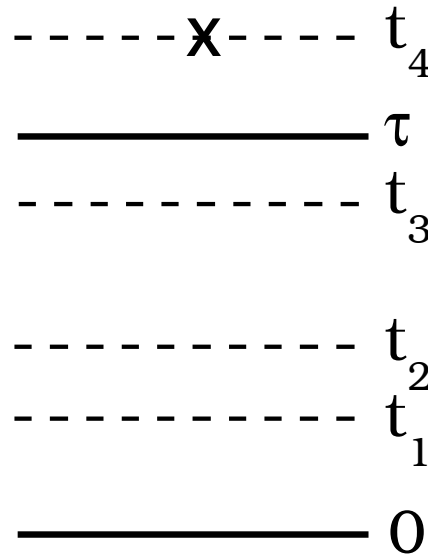


Figure 3-5: Time evolution in the SL algorithm. Dashed lines correspond to selected events, while the dashed line with an **X** corresponds to an event which is rejected since it exceeds the cycle time τ .

3.3.4 Dynamic Boundary Allocation

One of the main factors controlling the efficiency of a parallel KMC algorithm is the existence of boundary events, which can lead to “rollback” in the OSR algorithm and can decrease the accuracy of semi-rigorous algorithms such as the SL algorithm. A decrease in the number of boundary events can also significantly increase the optimal value of G used in the OSR and OSRPR algorithms and thus reduce the communications overhead. In the case of the SL algorithm, such a decrease can also allow the cycle time τ to be increased without sacrificing accuracy, thus increasing the parallel efficiency.

As an example, edge-diffusion near a processor boundary can lead to a large number of boundary events. Thus, if a processor or sublattice boundary passes near or cuts through an island this can significantly reduce the parallel efficiency. Accordingly,

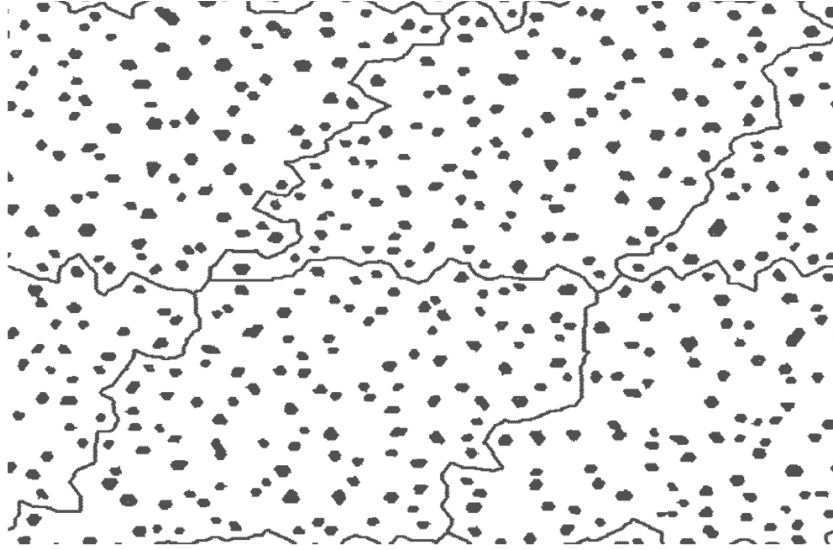


Figure 3-6: Example of square decomposition with DBA for system size $L = 512$ (triangular lattice with periodic boundary conditions) and $N_p = 4$.

we have developed a method for dynamic boundary allocation (DBA) [19] which keeps the processor and sublattice boundaries as far away as possible from islands. In our DBA method, we start with a spatial decomposition of the lattice using straight-line boundaries and use the island center-of-mass to assign islands to each processor or sublattice. We then use a “burning-algorithm” starting from each island boundary to determine the processor and/or sublattice boundaries between islands.

Since atoms and islands can diffuse and/or grow during a simulation, atoms will eventually move into the boundary region and as a result the parallel efficiency will decrease. To overcome this, DBA is carried out regularly (e.g. several times per *sec* of simulated time) to adjust the processor boundaries. Fig. 3-6 shows a typical square decomposition with DBA for the case of island-coarsening for a system size $L = 512$ with four processors. As can be seen, the processor boundaries are relatively

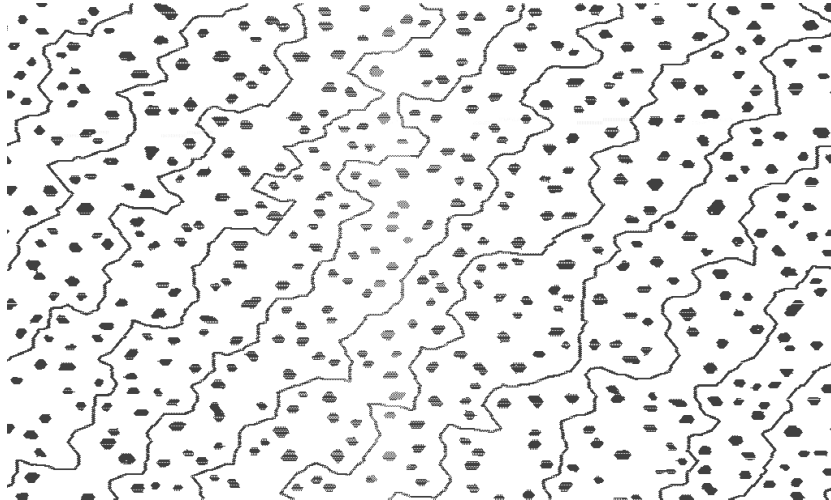


Figure 3-7: Same as Fig. 3-6 but for strip decomposition into sublattices with $N_p = 4$.

convoluted but remain well away from the island edges. A similar DBA decomposition is shown in Fig. 3-7 for the case of sublattice strip decomposition with four processors.

We note that in this case there are 8 separate sublattices.

3.4 Parallel Efficiency Results

Before presenting our results for Ag/Ag(111) island-coarsening, we first present our results for the parallel efficiencies of the OSR, OSRPR, and SL algorithm (with and without DBA) as obtained from simulations of room-temperature Ag/Ag(111) island coarsening (as described in more detail in Sec. 5.2) using our SLKMC-derived database. We note that in each case the parallel efficiency (PE) was obtained using the expression $PE = t_{ser}/(N_p t_p)$ where t_{ser} is the time for a serial simulation of the entire system (system size $L = 1024$), while t_p is the time for the corresponding parallel simulation where N_p is the number of processors.

Tables 3.1 and 3.2 summarize our results for the overall parallel efficiency of the

OSR, OSRPR and SL algorithms obtained from coarsening simulations with and without DBA for $N_p = 2$ and $N_p = 4$. As can be seen, in contrast to previous results using the OSR algorithm to study Ag/Ag(111) island nucleation and growth at very low temperatures [16], in our room temperature simulations of Ag(111) island coarsening, the PE of the OSR algorithm is generally low. In addition, due to the increased cost for global communications as well as the increased ratio of the boundary region to the processor “core” region, the PE decreases significantly with increasing N_p . Our results also indicate that including pseudo rollback (OSRPR algorithm) leads to a significant increase in the parallel efficiency although for the case $N_p = 4$ the PE still remains below 50%. However, in all cases we find that the SL algorithm yields the highest PE due to its significantly reduced communication overhead and relatively large number of KMC events carried out during a given cycle time τ .

We now discuss the effects of DBA on the PE as well as on the optimal value of G for the OSR and OSRPR algorithms. We note that without DBA the optimal value of G for the OSR and OSRPR algorithms is about 10 for $N_p = 2$ and decreases slightly with increasing N_p . On the other hand, with DBA the optimal value of G increases significantly, due to the significantly reduced number of boundary events. However, despite the large increase in G , the improvement of the PE for the OSR algorithm is only moderate due to the significant fraction of roll-back events f_R . On the other hand, the increase in the PE with DBA for the OSRPR algorithm is quite noticeable since the fraction of roll-back events is significantly decreased.

We now consider the parallel efficiency of the SL algorithm both with and without DBA. As already noted, in parallel KMC simulations of island nucleation and growth

Table 3.1: Comparison of efficiencies of parallel algorithms with $N_p = 2$ and $L = 1024$. The cycle time τ used for the SL algorithm is given in parentheses. f_R is the fraction of roll-back events per cycle in the OSR and OSRPR algorithms.

Algorithm	No DBA			DBA		
	PE	G (τ)	f_R	PE	G (τ)	f_R
OSR	0.33	9	0.27	0.43	161	0.21
OSRPR	0.47	11	0.04	0.58	161	0.02
SL	0.52	(10^{-7} s)	–	0.74	(10^{-6} s)	–

using the SL algorithm, the cycle time must typically be smaller than the inverse of the fastest possible single-event rate in the system [17]. More recently it was found [21] that in simulations of coarsening significantly longer cycle times can be used, thus decreasing the overhead due to communications and increasing the parallel efficiency. As shown in Fig. 3-8, by reducing the number of boundary events with DBA, the cycle time can be made even longer without affecting the accuracy, thereby improving the parallel efficiency significantly. Thus, we find (see Tables 3.1 and 3.2) that, due to the relatively low communications overhead as well as the relatively long cycle times, the PE for the SL algorithm is in general significantly higher than for the OSR and OSRPR algorithms. Accordingly, in our parallel KMC simulations of Ag(111) island coarsening over extended times, we have used the SL algorithm with $N_p = 4$ and a cycle time $\tau = 10^{-6}$ s. We note that with these parameters, the average number of events carried out per cycle per processor ($n_e \simeq 76$) was somewhat smaller than the optimal value of G using the OSRPR algorithm.

We now consider the parallel efficiency of the SL algorithm both with and without DBA. As already noted, in parallel KMC simulations of island nucleation and growth

Table 3.2: Comparison of efficiencies of parallel algorithms with $N_p = 4$ and $L = 1024$.

Algorithm	No DBA			DBA		
	PE	G (τ)	f_R	PE	G (τ)	f_R
OSR	0.14	7	0.53	0.25	151	0.45
OSRPR	0.22	7	0.28	0.41	151	0.05
SL	0.39	(10^{-7} s)	–	0.60	(10^{-6} s)	–

using the SL algorithm, the cycle time must typically be smaller than the inverse of the fastest possible single-event rate in the system [17]. More recently it was found [21] that in simulations of coarsening significantly longer cycle times can be used, thus decreasing the overhead due to communications and increasing the parallel efficiency. As shown in Fig. 3-8, by reducing the number of boundary events with DBA, the cycle time can be made even longer without affecting the accuracy, thereby improving the parallel efficiency significantly. Thus, we find (see Tables 3.1 and 3.2) that, due to the relatively low communications overhead as well as the relatively long cycle times, the PE for the SL algorithm is in general significantly higher than for the OSR and OSRPR algorithms. Accordingly, in our parallel KMC simulations of Ag(111) island coarsening over extended times, we have used the SL algorithm with $N_p = 4$ and a cycle time $\tau = 10^{-6}$ s. We note that with these parameters, the average number of events carried out per cycle per processor ($n_e \simeq 76$) was somewhat smaller than the optimal value of G using the OSRPR algorithm.

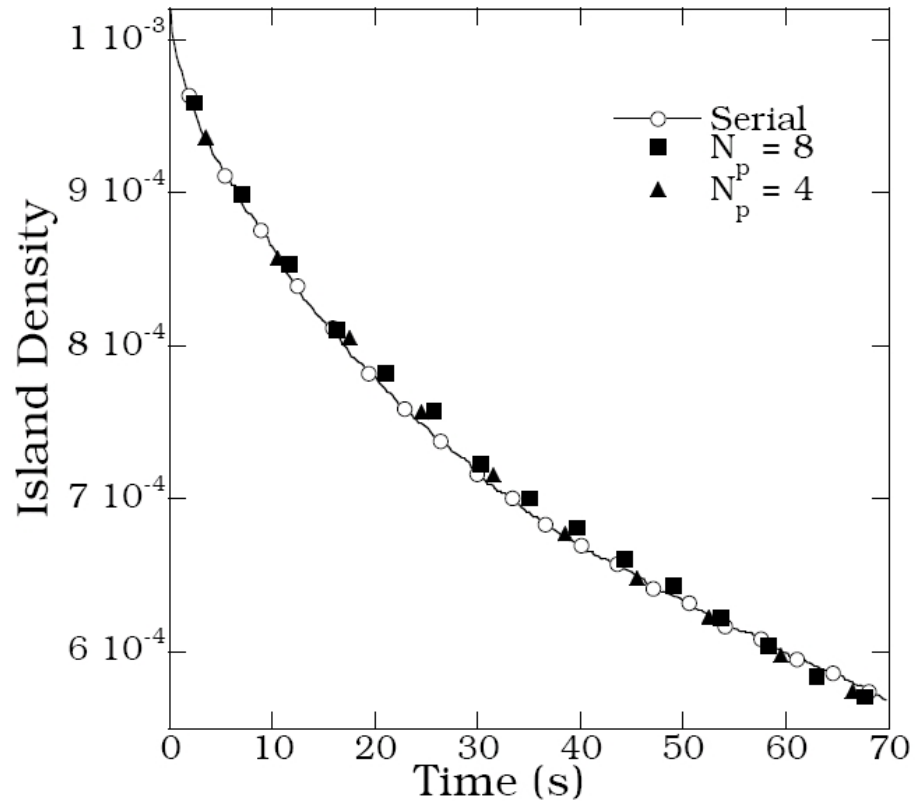


Figure 3-8: Comparison of results for the island density obtained from coarsening simulations carried out using serial KMC with the corresponding results obtained using the SL algorithm with DBA for $N_p = 4$ and $\tau = 10^{-6}$ s.

Chapter 4

Parallel Kinetic Monte Carlo

Simulations of Ag(111) Island

Coarsening using a Large Database

4.1 Introduction

Coarsening, i.e., the increase of the characteristic feature size with time, is a well known and ubiquitous phenomenon in many fields. In general, coarsening is driven by the minimization of the surface or interface energy in a system. This leads to survival of the fattest since large islands grow at the expense of small ones. Coarsening plays an important role in a wide variety of processes ranging from grain growth in alloys [22], to soot formation [23] to the formation of galaxies [24]. One example of particular current interest is the coarsening of two-dimensional (2D) or three-dimensional (3D) islands on a surface [25], since the coarsening process determines the

nanoscale ordering and surface structure. As a result, island-coarsening has recently been the subject of a large amount of experimental and theoretical work [25, 26, 27, 28, 29, 30, 31, 32, 33, 34]

Here we present the results of parallel kinetic Monte Carlo simulations of room-temperature coarsening of Ag(111) clusters carried out using a large database obtained via SLKMC simulations. We used the SL algorithm with DBA to extend the length and time scale of the simulation.

4.2 KMC Database

Our database was obtained from self-learning kinetic Monte Carlo simulations of Ag(111) island and cluster motion carried out at 300 K and 500 K and consists of two parts. The first part is a large-cluster database which was obtained from SLKMC simulations of islands of 19 atoms and larger, i.e. clusters typically consisting of a central atom and at least two filled rings. For these large islands, we have found that for homoepitaxy, cluster diffusion typically occurs via a series of single or multi-atom moves of edge-atoms from fcc sites to fcc sites. Accordingly, in this case the drag method was used for the associated saddle-point searches while all moves were assumed to involve fcc sites.¹

We note that for large islands we have found that these approximations are ad-

¹In the drag method, the moving entity is dragged in very small steps toward the probable (aimed) final state. The dragged atom is constrained in the direction toward the aimed position while the other two degrees of freedom (perpendicular to this direction) and all degrees of the rest of the atoms in the system are allowed to relax. The other atoms are thus free to participate in the move, thereby activating many-atom processes in which neighbor adatoms start to follow the central leading atom. In connection with the SLKMC method, the central atom is always dragged toward one of its vacant fcc sites.

equate to describe island diffusion. In particular, the scaling of the island diffusion coefficient with the island size was found to be in excellent agreement with previous determinations [10]. Hence, the first part of the database was filled using studies of the diffusion of large islands (i.e. periphery diffusion using drag method and fcc occupation). All activation energies were determined using interaction potentials based on the embedded-atom method (EAM) as developed by Foiles et al [35].

While the third shell surrounding a central atom was included in the SLKMC simulations when building the large-cluster database, in our KMC simulations only the first two shells were used, since the third shell surrounding a central atom has a relatively weak effect on the activation barrier. Accordingly, the large cluster database corresponds as shown in Fig. 2-2, to the first two shells surrounding an occupied site and contains approximately 2302 configurations (not including symmetry) with approximately 4455 different “moves” or transitions including concerted moves. Fig. 4-1 shows some of the low-barrier moves included in this database.

The second part of the database was a small-cluster database obtained from SLKMC simulations of islands of less than 19 atoms. In these small-island SLKMC simulations, it was found earlier [11] that the three assumptions used for large systems (that all cluster mobility is due to periphery motion, that all atoms remain on fcc sites, and that the drag method is sufficiently accurate) were unable to describe mechanisms revealed by molecular dynamics (MD) simulations of small islands on fcc(111). In particular, the most important mechanisms for diffusion of small islands were found (by MD) to be translation and rotation of the whole island. Since the drag method involving periphery atoms was unable to retrieve these two main mechanisms

and others involving collective motion, we proceeded by calculating their barriers using the nudged-elastic band (NEB) method [36, 37] and incorporating them into the SLKMC database. The last hurdle was to overcome the hcp occupancy (seen in MD simulations) since our SLKMC database involves only fcc occupancy. Using the fact that when a small cluster occupies fcc sites, it moves as a whole to hcp sites and then to fcc sites, we described a sequence of fcc-to-hcp and hcp-to-fcc moves as a single fcc-fcc move with a modified prefactor determined using symmetry (degeneracy) factors [11]. Hence, the database for small clusters was built by hand using NEB for mechanisms revealed by MD simulations and involving collective motion of the islands, in addition to moves involving periphery atoms which were found using the drag method attached to SLKMC.

Since the small-cluster database only involves clusters of less than 19 atoms, it only involves configurations in which there is a central atom surrounded by two partially filled rings and an empty third ring. We note that our small-cluster database contains 50 configurations (not including symmetry) with 252 different “moves“ or transitions including concerted moves. Fig. 4-2 shows some typical small-cluster transitions which were included in this database.

Thus, in order to find the possible transitions and their corresponding rates for a given configuration corresponding to an occupied central site and the surrounding rings, if the 3rd ring was unoccupied, we first searched the small cluster database for a match for the 1st and 2nd rings. If no match was found, or if the 3rd ring was not empty, we then searched the large cluster database for a match. We note

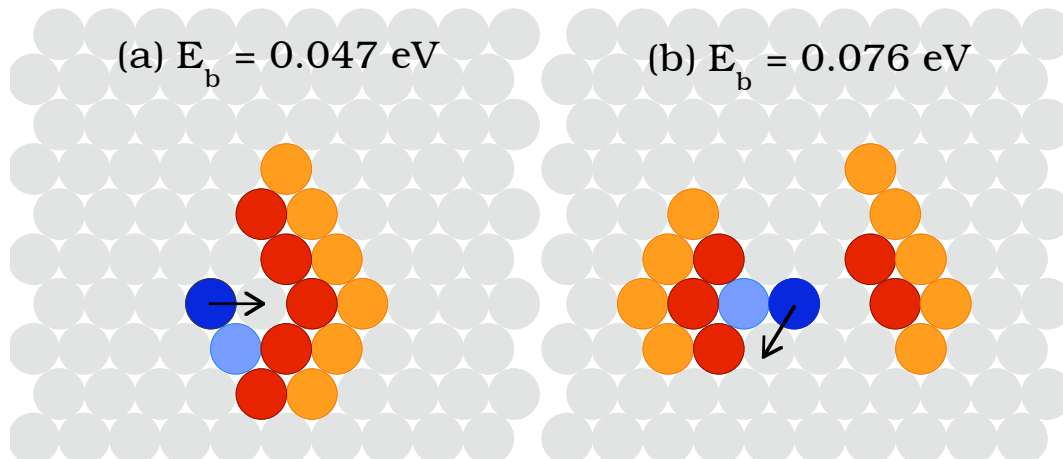


Figure 4-1: Two typical low-barrier moves in the large cluster database along with the corresponding activation barriers E_b . Dark blue atom corresponds to the central atom involved in the transition, while light blue and red atoms correspond to occupied sites in the first and second rings, respectively. Third ring of atoms (orange) is also shown.

that to save time, instead of doing a search through each database, we instead stored the data in a two-dimensional matrix with 1st (2nd) indices corresponding to the 1st (2nd) rings. However, if no match was found for either of the two indices, we then generated the (up to 5) additional symmetry representations for each of our two configuration ring indices, in order to search for symmetry equivalents. Once a configuration was identified as belonging to the database, the possible moves and their respective barriers were added to our KMC lists. However, if after searching both databases, the configuration was not identified as part of the database, then nothing was done.

Fig. 4-3 shows a histogram of the energy barriers corresponding to the 4712 processes (not including symmetry) in both databases. As can be seen, the distribution is very wide, covering activation energies as small as a few hundredths of an eV and as large as 0.8 eV. Assuming a prefactor of 10^{12} s^{-1} as was assumed in our sim-

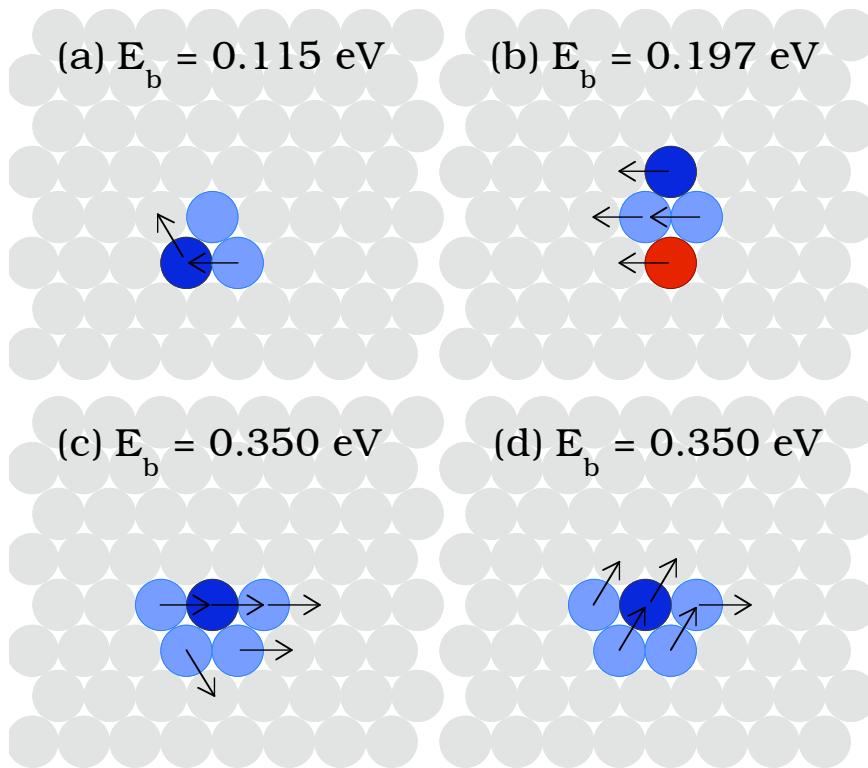


Figure 4-2: Some typical concerted moves in the small cluster database. Color code is the same as in Fig. 4-1.

ulations, this corresponds at room temperature to rates ranging from 0.036 s⁻¹ to approximately 8×10^{10} s⁻¹.

4.3 Results for Ag/Ag(111) Island Coarsening

In order to test our parallel KMC algorithm and also to apply the large database to a realistic problem, we have carried out parallel KMC simulations of Ag(111) island coarsening at room temperature. The initial configuration used in our coarsening simulations (see Fig. 4-4 (a)) was generated by depositing $\theta = 0.1$ ML at a deposition rate of 1 ML/s at 145 K. We then carried out parallel KMC simulations of coarsening at room temperature for 400 s using the SL algorithm with DBA and a cycle time of

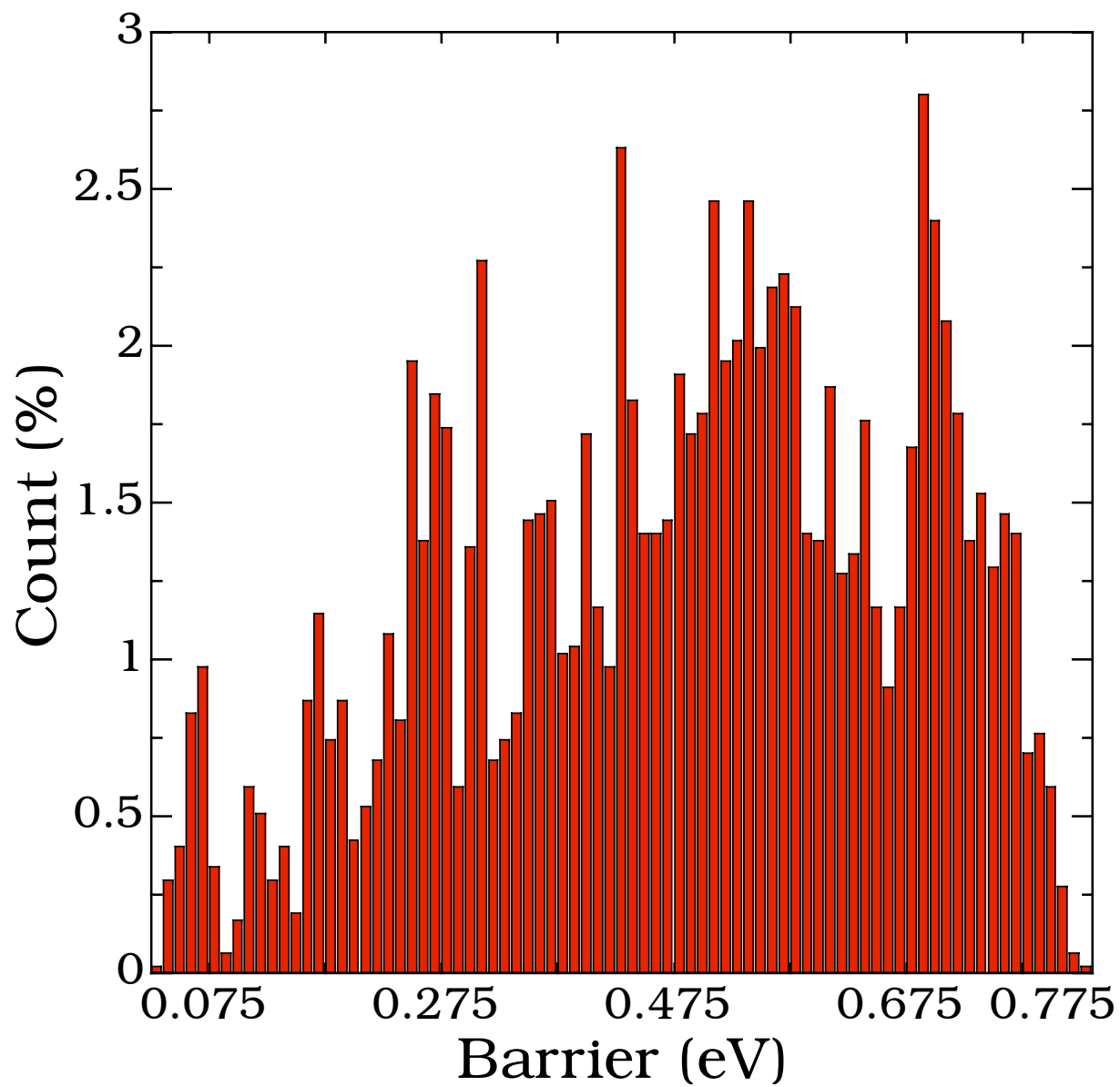


Figure 4-3: Histogram of energy barriers in the combined large and small cluster database (histogram width is 0.01 eV).

10^{-6} s with $N_p = 4$. In order to avoid finite-size effects our simulations were carried out using a relatively large lattice size $L = 1024$, while to have good statistics our results were averaged over 10 runs. We note that if each run had been carried out using serial KMC it would have taken almost 5 weeks. However, because of the use of parallel KMC the whole set of runs took only 2 weeks. In order to study the coarsening behavior, the island-size distribution $N_s(\theta, t)$ corresponding to the density of islands of size s (where s is the number of atoms in an island) at time t was measured along with the island density $N = \sum_{s \geq 2} N_s$, monomer density N_1 , and average island size $S = \sum_{s \geq 2} s N_s / N$.

Before presenting our simulation results, we note that for the case of 2D clusters on a surface, there are two particular limiting regimes - Ostwald ripening [38, 39] and cluster diffusion and coalescence [26, 27, 28, 40, 30, 29, 31, 32, 33] - in which the coarsening is dominated by diffusion. In the case of Ostwald ripening the islands are assumed to be immobile, while the coarsening is mediated by a background density of diffusing atoms such that islands bigger than a critical island-size grow while smaller islands shrink or evaporate. This results in power-law growth of the average island size $S(t) \sim t^{2n}$ where $n = 1/3$ [41, 42]. However, in the case of cluster diffusion and coalescence, if the cluster diffusion coefficient $D(s)$ decays as a power-law with island-size s , i.e. $D(s) \sim s^{-x}$, then $n = 1/2(1+x)$ [26]. In this case, three different limiting cases are of particular interest [27, 28, 40, 30, 29, 31, 32] - cluster diffusion due to periphery diffusion ($x = 3/2, n = 1/5$), cluster diffusion due to correlated evaporation/condensation ($x = 1, n = 1/4$), and finally cluster diffusion due to uncorrelated evaporation-condensation ($x = 1/2, n = 1/3$). Although asymptotically, one might

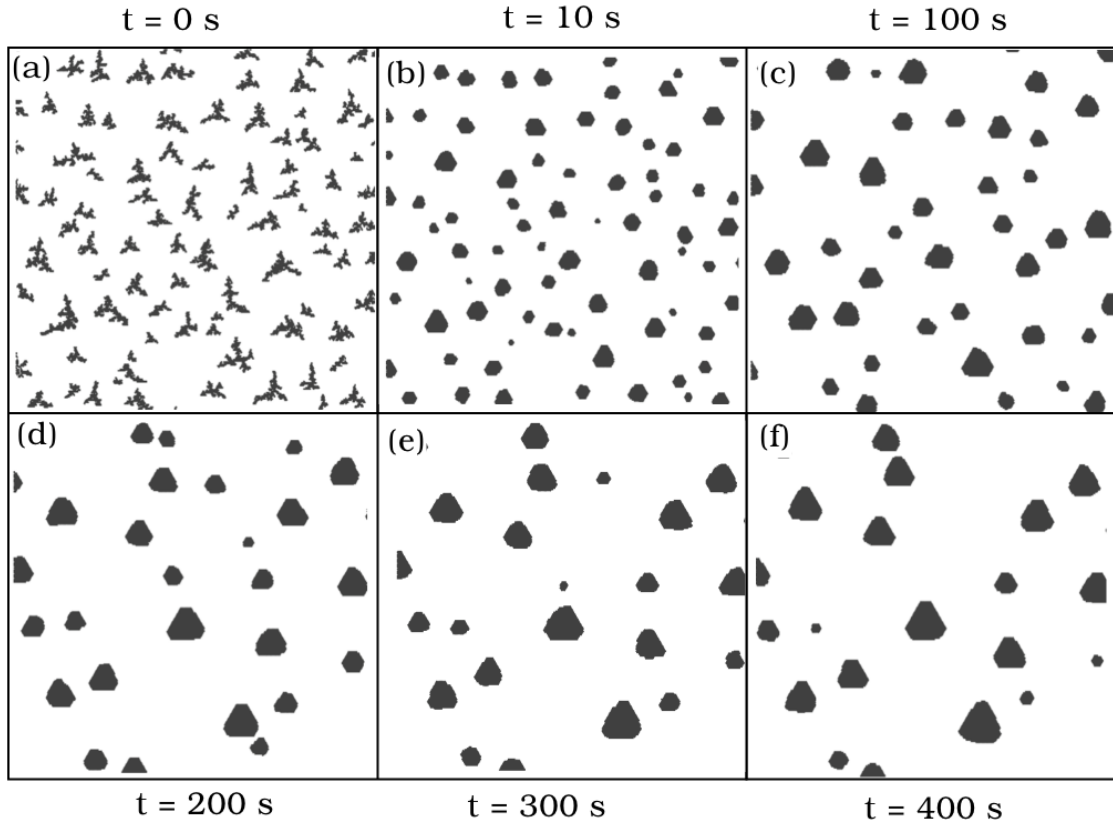


Figure 4-4: Evolution of island morphology during room-temperature coarsening. Pictures correspond to 256×256 portions of 1024×1024 system.

expect one of these processes to dominate, at intermediate times all of these processes may play a role.

Fig. 4-4 shows a typical example of the evolution of a portion of the system starting from the initial configuration at $t = 0$ and ending with the final configuration at $t = 400$ s. As can be seen, during the annealing process there is a dramatic change in the island morphology while the average island size increases dramatically. In particular, the system evolves from the small dendritic islands at $t = 0$ shown in Fig. 4-4(a) to the much larger truncated-hexagonal islands at $t = 400$ s shown in Fig. 4-4(f). These results for the island morphology are consistent with previous

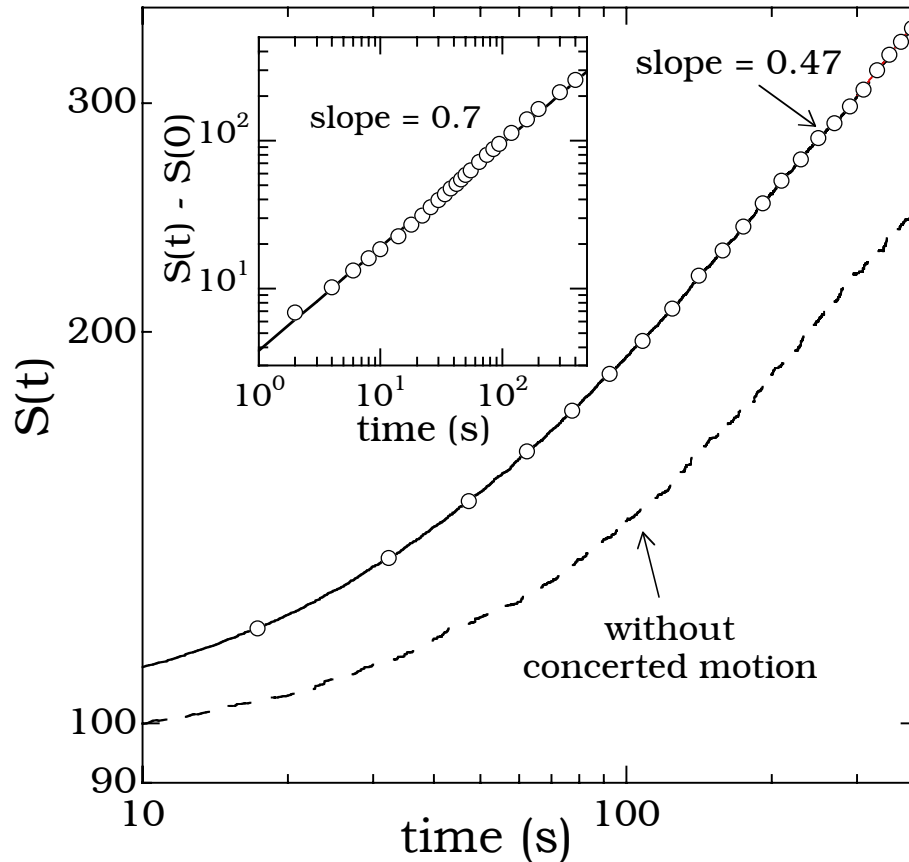


Figure 4-5: Average island size $S(t)$ as function of time (open circles). Dashed line corresponds to simulations without concerted motion. Inset shows log-log plot of $S(t) - S(0)$.

work using a simplified KMC model based on the same EAM potential for Ag, which indicates that for this potential the A step-edge is energetically favored over the B step edge [43].

Fig. 4-5 shows a log-log plot of the average island size $S(t)$ as a function of time. As can be seen, the effective slope increases with time while a fit to the late-time region indicates a coarsening exponent $n \simeq 0.47$. However, if the initial island size $S(0)$ is subtracted, then as shown in the inset, after an initial transient period the

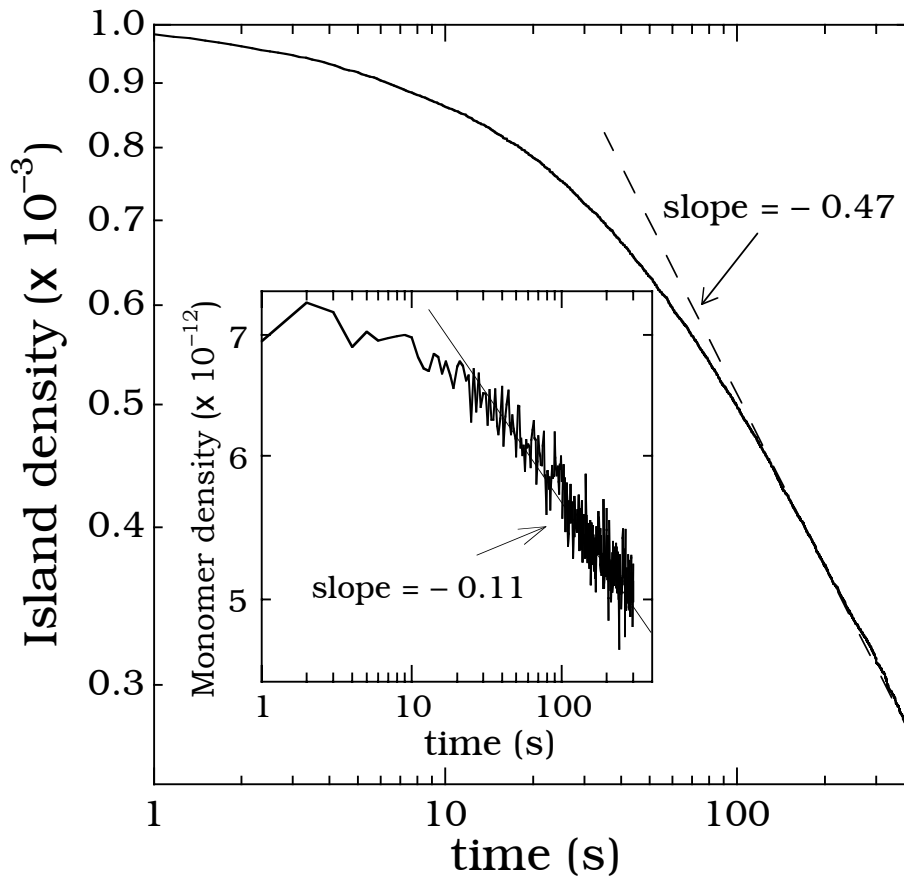


Figure 4-6: Island and monomer (inset) densities as function of time.

slope appears to approach an asymptotic value (0.70) which is close to $2/3$ and thus corresponds to a coarsening exponent $n \simeq 1/3$. Also shown in Fig. 4-5 (dashed curve) are results for the average island size starting with the same initial configurations but without the inclusion of multi-atom or concerted events during coarsening. As can be seen, while the asymptotic coarsening behavior is very similar, the average island size is significantly smaller. Thus, the inclusion of complex concerted moves in our KMC database significantly increases the average island size.

In order to better understand the asymptotic coarsening behavior we have also

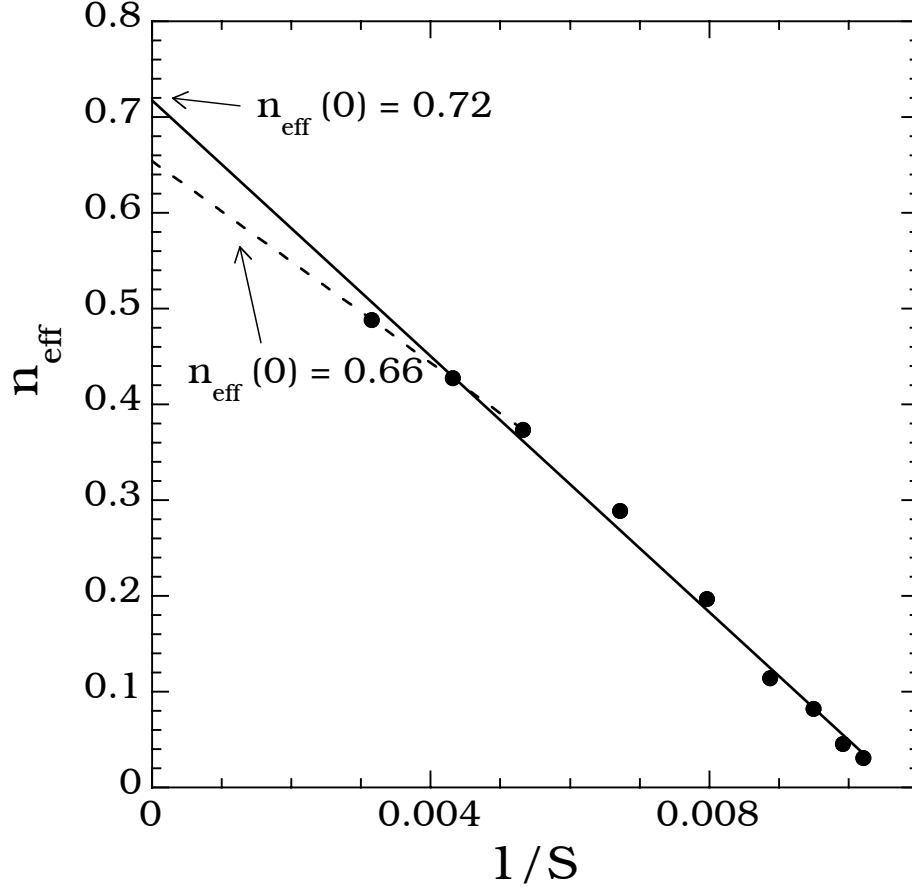


Figure 4-7: Effective coarsening exponent n_{eff} as function of $1/S$.

calculated the effective exponent $n_{\text{eff}}(t)$ [44] using the expression,

$$n_{\text{eff}}(t) = \frac{\ln[S(t_f)/S(t_i)]}{2 \ln(t_f/t_i)} \quad (4.1)$$

where $t_f/t_i \simeq 2$. Fig. 4-7 shows a plot of n_{eff} as a function of inverse average island size $1/S$. As can be seen, a linear fit to the data gives an asymptotic exponent $n_{\text{eff}}(\infty) = 0.72$, while a fit to the last 3 points gives $n_{\text{eff}}(\infty) = 0.66$. This suggests that the asymptotic exponent is indeed close to $1/3$. We note that such an exponent is consistent with both cluster diffusion due to uncorrelated evaporation-condensation and Ostwald ripening. However, a detailed analysis of our simulations indicates that

while there is some cluster diffusion and coalescence at early times, at later times there is very little cluster diffusion. Instead, the coarsening appears to proceed via evaporation-condensation, i.e. small clusters shrink while larger clusters grow. Thus, in general our results are consistent with Ostwald ripening.

We note that in recent parallel KMC simulations of coarsening using a simplified bond-counting model [21], Ostwald ripening was also observed, although in this case an exponent of $1/3$ was obtained directly from the late-time slope on a log-log plot of average island size $S(t)$ as function of annealing time t . In this case, it was also noted that the effective value of the coarsening exponent n on such a plot did not approach $1/3$ until the monomer density was larger than the island density, while for earlier times the effective exponent was close to $1/4$. We note that such a condition is reasonable, since only when the monomer density is significantly larger than the island density can one think of the islands as being in quasi-equilibrium with a gas of monomers.

In order to determine if such a late-time regime has been reached in our Ag/Ag(111) island coarsening simulations, we have measured both the island and monomer densities as a function of time as shown in Fig. 4-6. We note that the monomer hopping rate in our simulations ($D_m = 8 \times 10^{10} \text{ s}^{-1}$) is sufficiently large, while the adatom-island detachment rate is significantly lower than D_m ($D_{detach} \simeq 2.2 \times 10^{-4} D_m$) and thus, most of the time there are no monomers in the system, and instead the main processes are edge-diffusion and island re-arrangement. Accordingly, to accurately measure the monomer density, we instead measured the number of monomer hopping events over an extended time-interval of 10^{-3} s , and then divided this number by

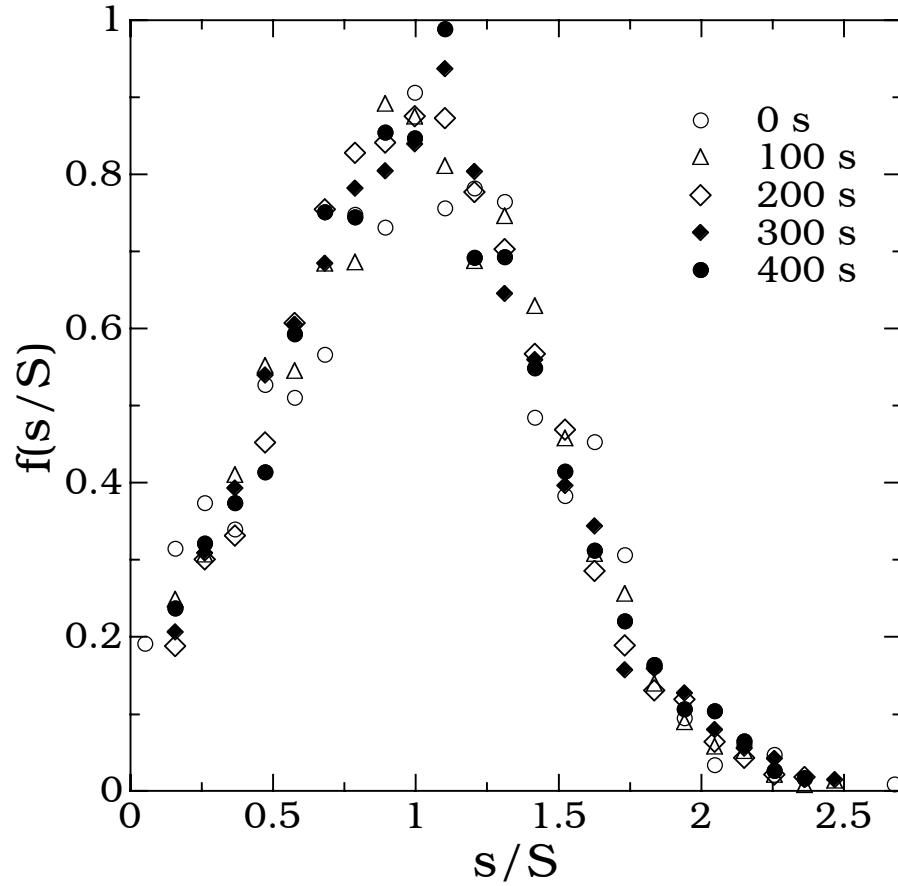


Figure 4-8: Scaled island size distribution at four different times during coarsening.

the product of this time-interval and the monomer hopping rate. As can be seen the monomer density is significantly lower than the island density, thus indicating that we have not yet reached the asymptotic regime. However, the slower decay of the monomer density indicates that at large enough times, the monomer density will indeed be larger than the island density. These results also support our conclusion that even though the asymptotic regime has not yet been reached, the coarsening is due to evaporation-condensation mediated by monomer diffusion.

We now consider the time evolution of the scaled island-size distribution (ISD)

given by [45],

$$f(s/S) = N_s(t)S^2/\theta. \quad (4.2)$$

Fig. 4-8 shows our results for the scaled ISD at $t = 0$, along with results at later times. Somewhat surprisingly, we find that even though the average island size increases significantly, the scaled ISD has very little dependence on time. This result is also in strong contrast to our previous study of a bond-counting model in which the asymptotic coarsening behavior was observed, while the scaled ISD was found to broaden and become less sharply peaked in the asymptotic regime. We note that this independence of the scaled ISD on time is consistent with recent experiments on room-temperature annealing of Cu/Cu(100) islands [46] in which the scaled ISD was also found not to change during the coarsening process. We believe that this independence of the ISD on annealing time is again due to the fact that we have not yet reached the asymptotic regime.

4.4 Analysis of energy barriers

In order to gain more insight into the dominant processes during coarsening we have also analyzed the frequency of events as a function of energy barrier. Fig. 4-9 shows a histogram of the energy barriers for all events carried out during the first 100 s of coarsening. Somewhat surprisingly, we find that the energy barriers for the most frequently selected processes are spread over a relatively wide range of values ranging from 0.06 eV to 0.5 eV, while the barrier for the most frequently selected event is

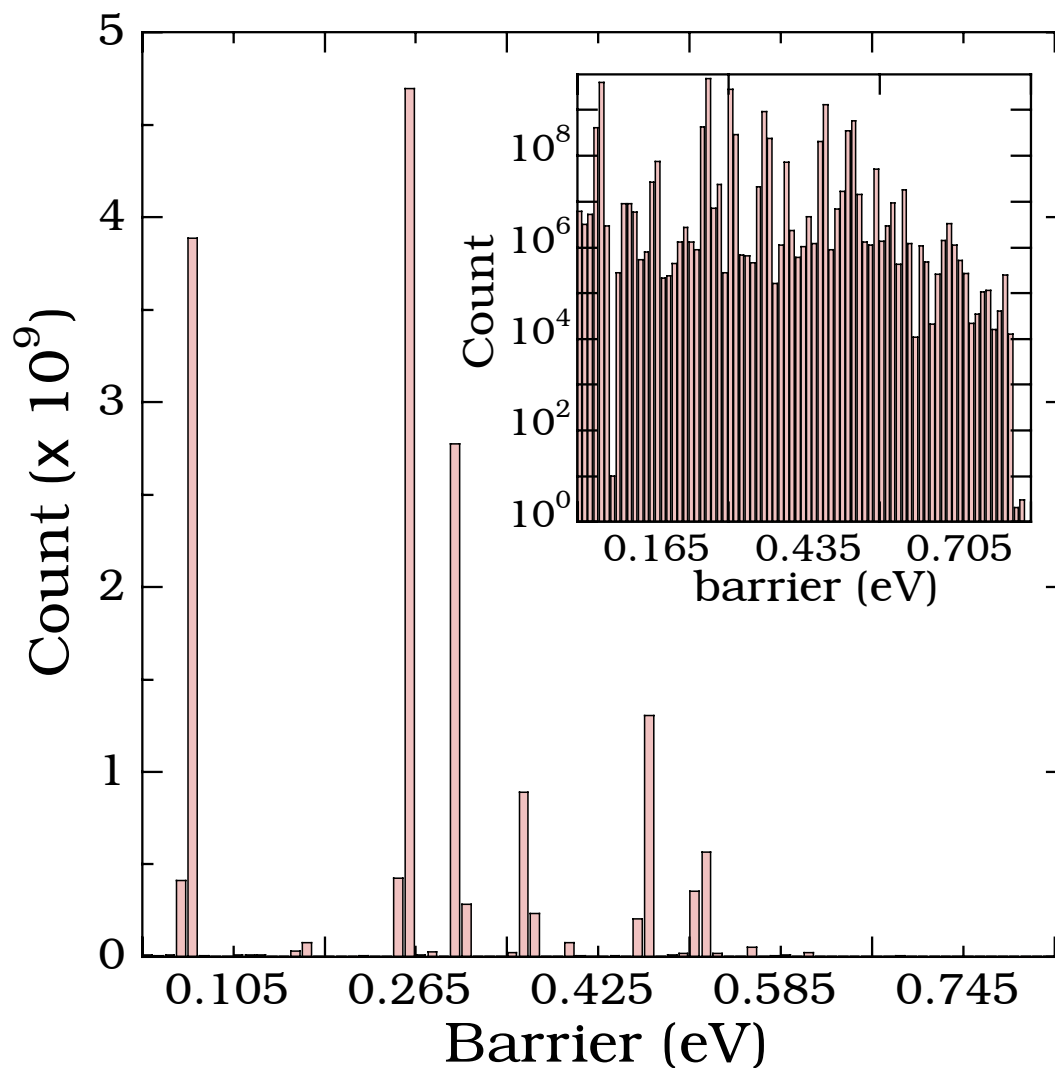


Figure 4-9: Histogram of energy barriers of selected events during the first 100 s of coarsening. Histogram width is 0.01 eV. Inset shows the same results on a semilog scale.

approximately 0.26 eV.

The inset of Fig. 4-9 shows the same data on a semi-log plot and indicates even more clearly that the energy barriers for selected events corresponds to a broad distribution. Fig. 4-10 shows the four most frequently selected moves other than monomer diffusion (which has a barrier of 0.066 eV) during the first 100 s of simulation. As can be seen the most frequently selected event corresponds to corner-rounding, with

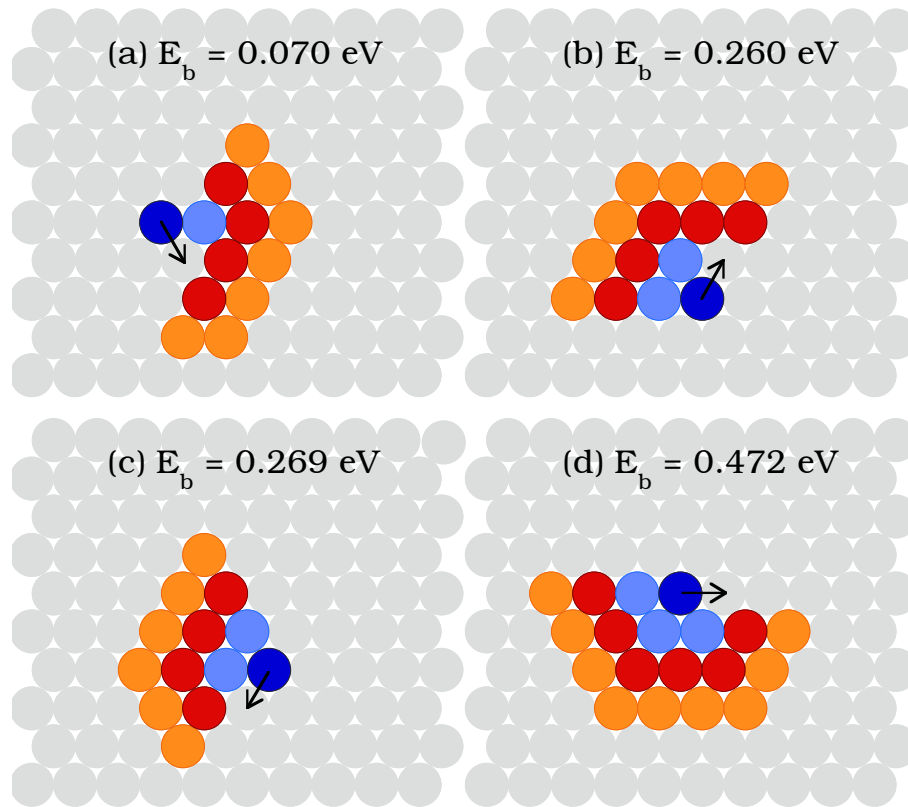


Figure 4-10: Configurations and energy-barriers corresponding to the 4 most frequently selected events during the first 100 s of coarsening.

a barrier of approximately 0.07 eV. However, the next two most frequently selected events correspond to edge-diffusion (see Fig. 4-10 (b) and (c)) and have significantly higher energy barriers (0.26 eV). We also note that detachment from a kink shown in Fig. 4-10 (d) occurs quite frequently despite its relatively high energy barrier (0.472 eV). However, it also leads to rapid reattachment to the kink site (with a much lower energy barrier of 0.253 eV) as shown in Fig. 4-10 (b). Thus, our results indicate that a variety of different processes with a wide range of energy barriers may play an important role in room-temperature island coarsening.

4.5 Conclusion

As a test of the applicability of parallel algorithms to realistic simulations over extended time- and length-scales, we have presented the results of kinetic Monte Carlo simulations of the room-temperature coarsening of Ag(111) islands carried out using a large database obtained via SLKMC simulations. Our results indicate that while cluster diffusion and coalescence play a role for small clusters and at very early times, at late time the coarsening proceeds via Ostwald ripening, i.e. large clusters grow while small clusters evaporate. In addition, an asymptotic analysis of our results for the average island-size as a function of time leads to a coarsening exponent $n = 1/3$ in good agreement with theoretical predictions for this case. By comparing with simulations without concerted (multi-atom) moves, we also find that the inclusion of such moves significantly increases the average island-size. Somewhat surprisingly we also find that, while the average island-size increases significantly during coarsening, the scaled island-size distribution does not change significantly.

In addition to presenting results for the coarsening of Ag(111) islands we have also presented results for the efficiency and accuracy of a number of different parallel algorithms. In particular, we have presented results for the optimistic synchronous relaxation (OSR), optimistic synchronous relaxation with pseudo-rollback (OSRPR), and semi-rigorous synchronous sublattice (SL) algorithms, as well as a number of improvements such as dynamic boundary allocation (DBA). Because of the relatively high temperature of our simulations, as well as the large range of energy barriers present in the database ranging from 0.05 eV to 0.8 eV, developing an efficient al-

gorithm for parallel KMC and/or SLKMC simulations was particularly challenging. However, by using dynamic boundary allocation (DBA) to minimize the number of boundary events, we have achieved significantly improved parallel efficiencies for the OSRPR and SL algorithms. In particular, the optimal value of G increased significantly for both the OSR and OSRPR algorithms due to the significantly reduced number of boundary events. However, there was a negligible improvement in the parallel efficiency for the OSR algorithm due to the significant fraction of roll-back events. Finally, we note that among the three parallel algorithms which we have tested, the semi-rigorous SL algorithm with DBA led to the highest parallel efficiencies. As a result, we have obtained reasonable parallel efficiencies in our simulations of room-temperature Ag(111) island coarsening using this algorithm for a moderate number of processors (e.g. $N_p = 2$ and $N_p = 4$). Since the SL algorithm scales with system size for fixed processor size, while the parallel efficiency increases with increasing processor size, we expect that comparable and/or even larger parallel efficiencies should be possible in parallel KMC and/or SLKMC simulations of larger systems with larger numbers of processors.

In conclusion, we have carried out realistic parallel KMC simulations of Ag(111) island coarsening using a large database obtained from SLKMC simulations and tested the parallel performance of the OSR, OSRPR, and SL algorithms with and without DBA. We find that the SL algorithm with DBA yields the highest parallel efficiency due to the significantly increased cycle time, and also exhibits the best scaling behavior as a function of the system size and number of processors. However, the parallel efficiency for the OSRPR algorithm with DBA is also quite reasonable for a relatively

small number of processors, suggesting that this algorithm may also be useful in a variety of parallel KMC simulations. Finally, our coarsening simulation results indicate that while cluster diffusion and coalescence play a role at early and intermediate times, at late times the coarsening appears to proceed via Ostwald ripening.

Chapter 5

First-passage time approach to kinetic Monte Carlo simulations of metal(100) growth

5.1 Introduction

Kinetic Monte Carlo (KMC) is an extremely efficient method[7, 47, 48, 49, 6, 18] to carry out non-equilibrium simulations of dynamical processes when the relevant rates are known. As a result, the KMC method has been successfully used to carry out simulations of a wide variety of dynamical processes over experimentally relevant time- and length-scales. However, in some cases, such as when the relevant processes have a wide range of activation energies, much of the simulation time can be ‘wasted’ on low-barrier repetitive events. As a result, in these cases direct KMC simulations may not be sufficient to reach the time-scales of interest.

A variety of approximate approaches to dealing with this “time-scale” problem have been suggested, including the level-set method[50] and other multi-scale approaches.[51, 52, 53, 54] However, another approach is the use of first-passage-time (FPT) algorithms. In this approach one avoids simulating the numerous diffusive hops of atoms, and instead replaces them with an analytic expression for the first-passage time to make a transition from one location to another.¹ For example, the FPT method has been used in Monte Carlo simulations of single-walker propagation,[56, 57] as well as in simulations of annihilating continuum random walkers in two and three-dimensions.[58] More recently a hybrid FPT method has been used to study the irreversible growth of extended one-dimensional islands.[59] However, perhaps because of their complexity, FPT techniques have not been previously used to carry out simulations of multilayer epitaxial growth.

Here we develop and apply a FPT method to accelerate KMC simulations of multilayer epitaxial growth. We note that one of the primary motivations of this work was the observation that, due to the extremely low-barrier for edge-diffusion in Cu/Cu(100) growth, a great deal of computation time is ‘wasted’ on repetitive edge-diffusion events even at relatively low temperatures. Accordingly, we have used our method to carry out simulations of a variety of models of epitaxial growth with fast edge-diffusion and a significant barrier for corner-rounding. These include a relatively sophisticated effective-medium-theory (EMT) model of Cu/Cu(100) growth as well as simpler irreversible growth models including a ‘generic’ model of irreversible fcc(100)

¹We note that in the context of standard Monte Carlo simulations a similar method, the ‘absorbing Markov chain method’ has also been developed, see Ref. [55]

growth and a solid-on-solid model.

In our simulations, the process of (one-bond) edge diffusion is treated using the FPT approach, while the remaining activated processes are treated with regular KMC. In particular, the process of edge diffusion was first mapped onto a one-dimensional random walk between two partially absorbing boundaries for which explicit expressions for the mean FPT and absorption probabilities have already been derived. [60, 44] For completeness, we have also derived explicit expressions for the conditional first-passage time. In order to take into account the difference in hopping rate at a corner and along a straight-edge, we have also derived analytical expressions for the number of times an edge-diffuser reaches a boundary corresponding to a kink-attachment site or a corner before being absorbed. Since an edge-diffuser can interact with other atoms such as another edge-diffuser or a monomer approaching a step, we have also included these interactions in our simulations. While this requires significant overhead, we have been able to achieve a significant speed-up in simulations of multilayer epitaxial growth carried out using our FPT method. In addition, we find that in the absence of significant detachment of edge-diffusers from step-edges, there is excellent agreement between our FPT KMC simulations and regular KMC simulations.

This chapter is organized as follows. In Sec. 5.2 we describe the models used in our simulations. These include an effective medium theory (EMT) model of Cu/Cu(100) growth as well as two irreversible growth models - a generic model of fcc (100) growth and a solid-on-solid (SOS) model. In Sec. 5.3.2 we describe our FPT approach in detail and also provide the corresponding analytical expressions for first passage time and

absorption probabilities. A comparison between simulation results obtained using FPT KMC and regular KMC is presented in Sec. 5.4, while a summary of our results is presented in Sec. 5.5. Finally, in Appendix B.4 we derive corrections to the mean FPT corresponding to the number of times a diffusing particle hits the boundaries before it is absorbed. Explicit expressions for the conditional FPT are also derived in Appendix B.3.

5.2 Model

In order to test our FPT KMC method, we have applied it to an EMT model of Cu/Cu(100) growth with fast edge-diffusion which also takes into account the fcc crystalline geometry. We note that this model has previously been used [20, 61] to obtain excellent quantitative agreement with the experimental results of Ernst *et al* [62] for Cu/Cu(100) multilayer growth at 160 and 200 K. More recently it has also been used [63] to explain similar but slightly different experimental results for Cu/Cu(100) growth obtained by Botez *et al.* [64]

In this model, the energy barriers for intralayer diffusion correspond to a parameterization of EMT barriers calculated by Jacobsen. [65] In particular, as shown in Fig. 5-1, in the EMT model the energy barriers for hopping of an adatom on a flat terrace are determined by its interactions with the five neighboring atoms labeled A, B_1, B_2, C_1 , and C_2 . In particular, if an adatom (filled circle) has a lateral bond with neighboring site i (where $i = A, B_1, B_2, C_1$ and C_2), then the occupation number N_i for that site is 1 and otherwise it is zero. The corresponding energy barrier E_b

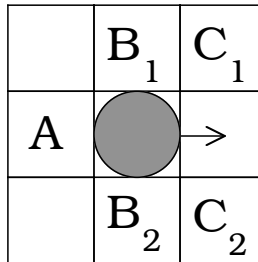


Figure 5-1: Diagram showing neighboring sites affecting the energy barrier for intralayer diffusion of a central atom (shaded circle) used in EMT model of Cu/Cu(100) growth (see Eq. 5.1).

may then be calculated using the expression, [65]

$$E_b = \frac{E_a}{2} + \frac{E_a}{2} [\delta(N_A, 1) + \delta(N_{C_1}, 0)\delta(N_{C_2}, 0) (1 + \delta(N_{B_1}, 1)\delta(N_{B_2}, 1))] \quad (5.1)$$

where $E_a = 0.425$ eV is the activation energy for monomer diffusion. We note that this expression implies the existence of 4 possible different values for the intralayer diffusion barrier: $E_a/2$ for atoms without an A neighbor but with one or both of C_1, C_2 , E_a for atoms with no neighbors, and also for atoms with an A neighbor and one or both of C_1, C_2 , $3E_a/2$ for atoms with an A neighbor and no “B” or “C” neighbors, and $2E_a$ for atoms with an A neighbor and both “B” neighbors and no “C” neighbors. One of the consequence of Eq. 5.1 is the existence of “fast” edge-diffusion (see Fig. 5-2) with a barrier ($E_a/2$) which is significantly smaller than that for monomer diffusion. Another consequence is that dimer diffusion (via reptation) is as fast as monomer diffusion. Once the activation barrier is obtained, the rate for a given move is given by $D = D_0 e^{-E_b/k_B T}$ where $D_0 = 3 \times 10^{11} \text{ sec}^{-1}$. We note that this value was determined by comparing the calculated antiphase diffraction factor

at a coverage of 0.3 monolayer (ML) at $T = 213$ K and deposition rate $F = 0.1$ ML/min with the corresponding experimental results of Swan *et al.* [66] In all of our simulations a deposition rate $F = 1/120$ ML/s - the same as in the experiments of Ernst *et al.*[62] - was assumed.

In order to simulate multilayer growth, the model described by Eq. 5.1 has been modified in two ways.[20] First, to take into account the Ehrlich-Schwoebel (ES) barrier, [67, 68] for all interlayer diffusion processes an additional ES barrier of 0.02 eV is added to the value E_b given by Eq. 5.1. We note that this should be considered to be an *effective* ES barrier, since both EMT calculations[69] and density-functional theory (DFT) calculations[70] indicate that the ES barrier for interlayer diffusion at a close-packed step-edge is significantly higher than at an open step-edge. The second modification involves the barrier for corner-rounding (see Fig. 5-2(e)). Since Eq. 5.1 implies that the barrier for an adatom at a corner along a step-edge of an island to detach along the edge is given by E_a while the barrier to ‘re-attach’ is very small ($E_a/2$), this implies an effective corner-rounding barrier of 0.425 eV. However, in Ref. [20] it was found to be necessary to assume a smaller effective corner-rounding barrier (e.g. 0.35 eV) in order to explain the relatively large value of the growth exponent β ($\beta \simeq 1/2$) found in the experiments of Ernst *et al.*[62] at 200 K. Accordingly, in our simulations, this smaller barrier was used. We note that in our model this enhanced corner-rounding move is only allowed to occur for the case of in-plane motion, i.e. no combined enhanced corner-rounding and interlayer diffusion moves are included in our simulations. Finally, we note that in all the results presented here the ‘corner-rounding’ move was suppressed for dimers and trimers since this leads

to enhanced dimer and trimer diffusion.

As in previous simulations of metal(100) growth, also included in our model is downward funneling (DF),^[71] for atoms deposited at non-four-fold hollow sites. In KMC simulations with the usual DF and no short-range attraction, atoms are assumed to be deposited only at the underlying fcc(100) lattice sites, each of which corresponds to a ‘capture zone’ for deposition.^[72, 73] In particular, if a selected deposition site is a four-fold hollow site, then the deposited atom remains where it is immediately after deposition. However, if one or more of the four-fold hollow ‘support’ atoms is missing, then the atom ‘cascades’ randomly to one of the missing support sites. This process is repeated until a four-fold hollow site is found. As in Ref. ^[20], in the simulations presented here, the deposition process is similar, but with a small modification to take into account the effects of uphill funneling as determined from molecular dynamics simulations.^[73] In particular, if an atom lands at a site which is not a four-fold hollow site but for which one or more of the missing support sites are themselves four-fold hollow sites, then one of these four-fold hollow sites is randomly selected. Otherwise, the deposition process is the same as for DF.

Fig 5-2 shows some of the important intralayer diffusion moves in our EMT model, including monomer-diffusion (Fig. 5-2(a)), singly-bonded edge-diffusion (Fig. 5-2(b)), double-bond edge-diffusion (Fig. 5-2(c)), corner-rounding (Fig. 5-2(e)), kink detachment (Fig. 5-2(f)), and kink re-attachment (Fig. 5-2(d)). As can be seen, the barriers for singly-bonded edge-diffusion, doubly-bonded edge-diffusion and kink re-attachment are very low (e.g. $E_a/2 = 0.2125$ eV) while the barrier for kink de-

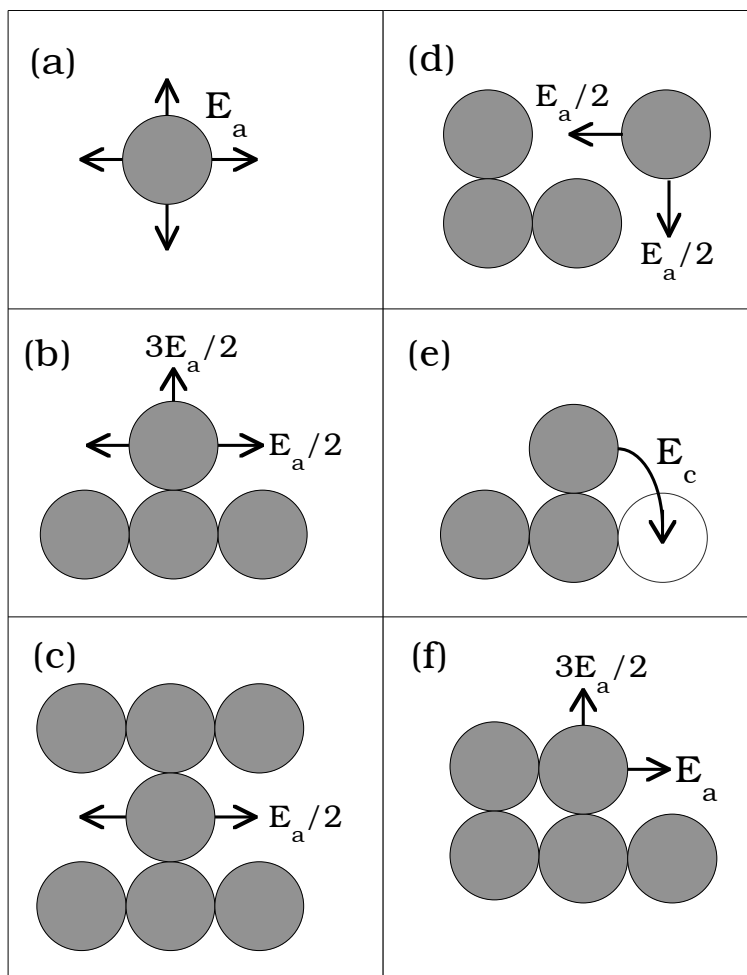


Figure 5-2: Diagram showing some important intralayer moves in EMT Cu(100) model along with corresponding activation barriers. (a) monomer diffusion (b) single-bond edge diffusion and detachment (c) two-bond edge diffusion (d) monomer attachment at a step-edge (e) corner-rounding ($E_c = 0.35$ eV) (f) kink detachment along an edge.

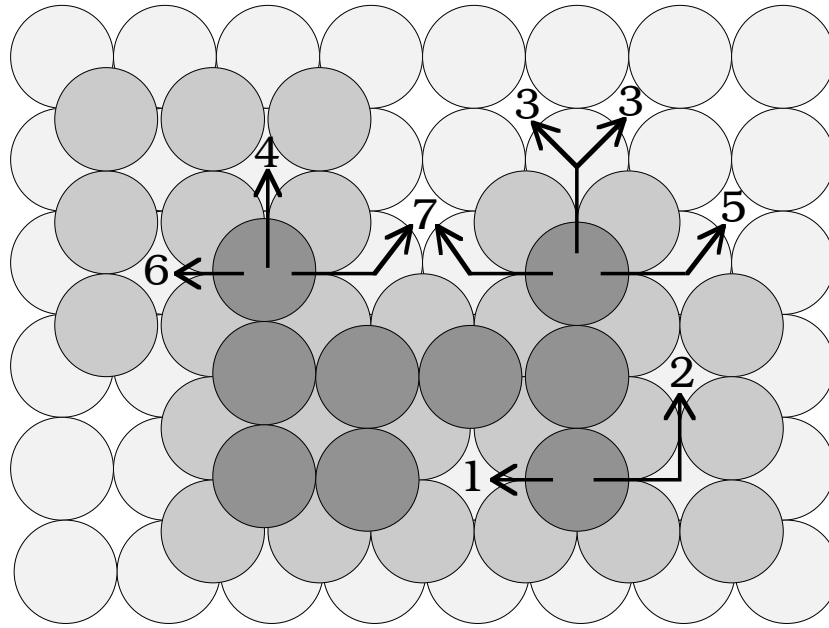


Figure 5-3: Pathways for edge- and interlayer diffusion in EMT Cu(100) model. Barriers for each process are as follows: (1) $E_a/2$ (2) E_c (3) $3E_a/2 + E_{ES}$ (4) $3E_a/2$ (5) $E_a + E_{ES}$ (6) E_a (7) $E_a/2 + E_{ES}$

attachment along an edge (see Fig. 5-2(f)) is the same as for monomer diffusion. Accordingly, we expect that both singly-bonded and doubly-bonded edge-diffusion will lead to fast repetitive events which can significantly slow down regular KMC simulations. However, because it turns out that two-bond edge-diffusion has almost no effect on either the surface roughness or the surface morphology, and also because the focus here is on applying the FPT method to accelerate single-bond edge-diffusion, to save computational time the rate of two-bond edge-diffusion has been reduced by a factor of 10 in all of our EMT model simulations. Fig. 5-3 shows all the possible different absorption pathways for a singly-bonded edge-diffusing atom in our EMT model along with the corresponding barriers. In addition to kink-attachment (1) and corner-rounding (2), these include detachment perpendicular to an edge with (3) or

without (4) interlayer diffusion, detachment parallel to an edge with (5) and without (6) interlayer diffusion, and edge-diffusion over a step-edge (7).

In addition to the Cu/Cu(100) growth simulations carried out using the EMT model described above, we have also carried FPT KMC simulations of two simpler irreversible growth models. These include a “generic” fcc model with DF and irreversible island formation (no detachment) as well as an even simpler solid-on-solid (SOS) model which is similar to the “generic” fcc model but which does not take into account the fcc geometry. In order to mimic the effects of DF, in the SOS model any atom deposited at a step-edge was assumed to “funnel” down randomly to one of the lower nearest-neighbor sites. For both of these irreversible growth models, the deposition flux, and the rates of monomer interlayer and intralayer diffusion, and edge- and corner-diffusion were assumed to be the same as for the EMT model.

5.3 Application of FPT method to KMC

5.3.1 First-Passage Time for 1D Random Walker

Before discussing the application of our FPT method to KMC simulations, we first present the relevant analytical expressions for the FPT of a 1D random walker diffusing on the interval $[0, L]$ with partial reflection and absorption at each boundary (see Fig. 5-4). Away from the boundaries the particle has an equal probability of moving to the right or to the left at each time-step. However, we assume that when the walker arrives at site 0 (L), it is absorbed with probability β_0 (β_L) and reflected

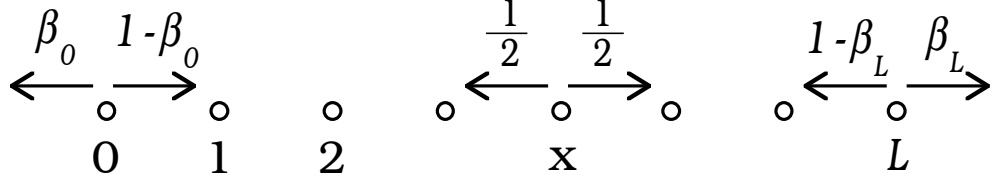


Figure 5-4: Schematic showing 1D random walker diffusing between partially absorbing boundaries at 0 and L with absorption probabilities β_0 and β_L respectively.

with probability $1 - \beta_0$ ($1 - \beta_L$) respectively. The probability $P_0(x, L, \eta_0, \eta_L)$ that a walker initially at site x will be absorbed at 0 is then given by,[60, 44]

$$P_0(x, L, \eta_0, \eta_L) = \frac{L - x + \eta_L}{L + \eta_0 + \eta_L} \quad (5.2)$$

where $\eta_0 = (1 - \beta_0)/\beta_0$ and $\eta_L = (1 - \beta_L)/\beta_L$, while the probability that the walker will be absorbed at site L is given by $P_L(x, L, \eta_0, \eta_L) = 1 - P_0(x, L, \eta_0, \eta_L)$. In addition, the average number of hops $n(x)$ or mean FPT before a walker initially at site x is absorbed at *either* of the boundaries is given by,[74, 60]

$$n(x) = \left[\frac{L(L + 2\eta_L)(x + \eta_0)}{(L + \eta_0 + \eta_L)} - x^2 \right] \quad (5.3)$$

While we will primarily make use of Eq. 5.3, it is also interesting to consider the *conditional* first-passage time $n_0(x)$ ($n_L(x)$) corresponding to the average number of hops before a particle is absorbed at site 0 (L). We note that the conditional first-passage times $n_0(x)$ and $n_L(x)$ must satisfy the condition,

$$n(x) = P_0(x, L, \eta_0, \eta_L) n_0(x) + P_L(x, L, \eta_0, \eta_L) n_L(x) \quad (5.4)$$

We also note that expressions for the conditional FPT's $n_0(x)$ and $n_L(x)$ were presented in Ref. [60]. However, perhaps due to an error in the boundary conditions, these expressions are not correct and do not satisfy Eq. 5.4. Accordingly, in Appendix B.3 we derive and present correct expressions for the conditional first passage times $n_0(x)$ and $n_L(x)$ for a 1D random walker diffusing between two partially absorbing boundaries.

5.3.2 Implementation of FPT approach

In order to speed-up our KMC simulations, we have replaced the detailed moves of a singly-bonded atom diffusing along an island-edge, by a calculation of its overall escape time for “absorption”. We note that the remaining diffusive moves, for which the barriers are typically significantly higher than for edge-diffusion, are treated as regular KMC moves. Accordingly, we map the diffusion of an edge-atom to a 1D random walk with partially absorbing boundaries with the appropriate values of x, L, β_0 and β_L . For example, for the case shown in Fig. 5-5, with kink-attachment and corner-rounding at the boundaries, one has $x = 0, L = 3, \beta_0 = 1/2$, and $\beta_L = D_c/(D_e + D_c)$ where D_e and D_c are the rates of edge-diffusion and corner-rounding respectively. Assuming that the rate for edge-hopping in a given direction (D_e) is the same for all sites along the edge including the boundary sites, and ignoring the time required for the last “absorption” move from the boundary, then the mean first passage time $\tau_{mfp}(x)$ for an edge-diffuser at site x to “escape” from the edge is given by

$$\tau_{mfp}(x) = n(x)/(2D_e) \tag{5.5}$$

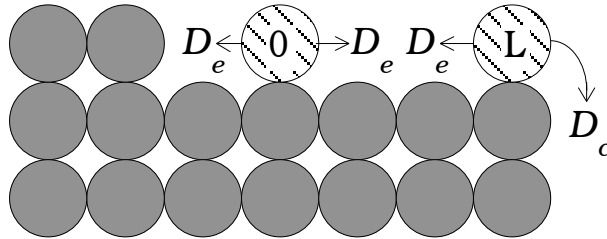


Figure 5-5: Example of edge-diffusion with two possible absorption pathways: attachment to a kink with rate D_e , and corner-rounding with rate D_c .

where $n(x)$ is given by Eq. 5.3 while $1/(2D_e)$ is the average time for each individual hop along the edge. However, as discussed in the next subsection, additional terms must be included to take into account the boundary site corrections. These corrections turn out to be important to obtain good agreement with regular KMC simulations.

Corrections to first passage time

In deriving Eq. 5.5, we have assumed that the total edge-hopping rate ($2D_e$) for an edge-diffuser is the same for all sites including the boundary. However, this is not generally true, since the total hopping rate at a corner is given by $D_e + D_c$. As a result corrections to Eq. 5.5 must be included. In order to do so, one first needs to calculate the number of times an edge-atom arrives at a corner site before being absorbed. Let us denote by $h_{\alpha_1}(x, \alpha_2)$ the number of times (excluding the last time if $\alpha_1 = \alpha_2$) that a walker initially at position x arrives at boundary site α_2 before being absorbed at site α_1 (where $\alpha_1, \alpha_2 = 0$ or L). Then, assuming that the edge-atom was absorbed at boundary site α , the corresponding correction time $\Delta t_\alpha(x)$ to the mean

FPT given in Eq. 5.5 is given by,

$$\Delta t_\alpha(x) = \delta_0 h_\alpha(x, 0) + \delta_L h_\alpha(x, L) + \beta_\alpha/D_\alpha \quad (5.6)$$

where D_α is the rate for absorption at the boundary, $\delta_\alpha = \frac{\beta_\alpha}{D_\alpha} - \frac{1}{2D_e}$ corresponds to the correction time for each hop away from a boundary at site α , and the last term takes into account the additional time required for the last hop over the boundary. The mean correction-time $\Delta t_{av}(x)$ is then obtained by averaging over the possibilities that the edge-diffuser is absorbed at site 0 and site L and is given by,

$$\Delta t_{av}(x) = P_0(x)\Delta t_0(x) + P_L(x)\Delta t_L(x) \quad (5.7)$$

where $\Delta t_0(x)$ and $\Delta t_L(x)$ are given in Eq. 5.6.

By carrying out an exact enumeration of all possible walks (see Appendix B.4), we have derived analytical expressions for $h_0(x, 0)$, $h_0(x, L)$, $h_L(x, 0)$, and $h_L(x, L)$. In particular we find,

$$h_L(x, 0) = \frac{\eta_0(\eta_0 + 1)}{L + \eta_0 + \eta_L} \frac{L - x + \eta_L}{x + \eta_0} \quad (5.8)$$

$$h_L(x, L) = \eta_L \left[\frac{L - 1 + \eta_0}{L + \eta_0 + \eta_L} \right] \quad (5.9)$$

$$(5.10)$$

The corresponding results for $h_0(x, 0)$ and $h_0(x, L)$ may be obtained by interchanging

η_0 and η_L and replacing x with $L-x$ in Eq. 5.9 and Eq. 5.8 respectively. By combining Eq. 5.5 and Eq. 5.7 we obtain our final result for the mean first-passage time,

$$t_{mfp}(x) = \tau_{mfp}(x) + \Delta t_{av}(x) \quad (5.11)$$

We note that while the distribution of waiting times for a single KMC event corresponds to an exponential distribution (with mean equal to the inverse of the event rate) the distribution of first-passage times (with mean equal to the mean first-passage time) is expected to be somewhat sharper, since it corresponds to an ‘‘average’’ over a large number of elementary events. However, a general calculation of the full first-passage-time distribution is extremely difficult. Accordingly, we have considered the two extreme possibilities: (i) a delta-function distribution, e.g. $t_{fp}(x) = t_{mfp}(x)$ and (ii) an exponential distribution with mean equal to the mean first-passage time, e.g. $t_{fp}(x) = -\ln(\xi) t_{mfp}(x)$ where ξ is a uniform random number between 0 and 1. Somewhat surprisingly, we found that there was no difference in the simulation results obtained using the different distributions. Accordingly, in most of our FPT KMC simulations we have used the assumption of a delta-function distribution.

Interactions between edge-diffuser and other atoms

While the FPT expressions above give the escape time for an isolated edge-diffuser, an edge-atom can also interact with other atoms before escaping. Examples include the interaction of an edge-atom with another edge-atom on the same edge, with another edge-atom on a step-edge two lattice units away, and with a monomer ap-

proaching the same edge either from above or below the step. We first consider the interaction between an edge-atom and another edge-atom on the same edge (atoms B & C in Fig. 5-6). Since it is difficult to determine an exact expression for the distribution of collision-times and locations for two edge-diffusers along an edge in order to approximately include such an interaction in our simulations, for each edge-diffuser we have treated any neighboring edge-diffuser as a stationary kink site (see sites C_2 and B_1 in Fig. 5-6). However, to take into account the fact that the relative diffusion rate is twice the rate of a single edge-diffuser, the calculated FPT for collision of each edge-diffuser with the other is divided by a factor of 2. Similarly, a monomer approaching a step-edge on the lower terrace one step away from the step-edge, is also treated as a kink site (Fig. 5-6, sites A_2 and C_1). However, in this case the edge-diffuser is first moved to a random site along the edge before calculating the FPT to attach to the monomer. This is a good approximation for the models studied here since the rate of edge-diffusion is significantly higher than the monomer hopping rate as well as the (per site) deposition rate. For the SOS model this “equilibration” is particularly important if the monomer arrives from the upper step. In this case the edge diffuser is first moved to a random site along the edge before either performing interlayer diffusion or calculating the effective DF due to knockout for a freshly deposited atom at a step-edge. We note that while the inclusion of such approximate equilibration processes only affects the surface roughness very weakly, it has a strong effect on the surface morphology, and is therefore important to include especially in SOS models.

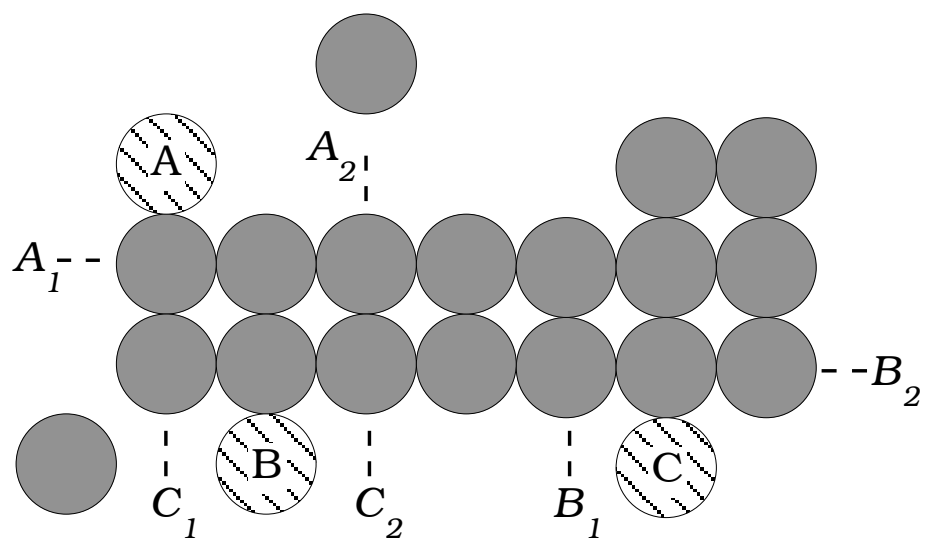


Figure 5-6: Examples of edge-atoms (striped circles) and their corresponding absorption sites (dashed lines) including interactions with monomers, e.g. absorption sites for atom A are A_1 and A_2 .

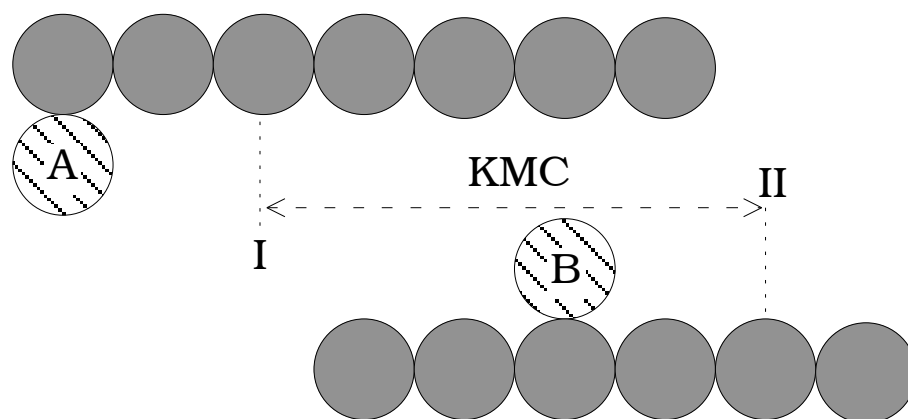


Figure 5-7: Two interacting step-edges. Edge-atoms between sites I and II are treated with regular KMC, while edge-atoms outside this region (e.g. atom A) are treated using FPT KMC.

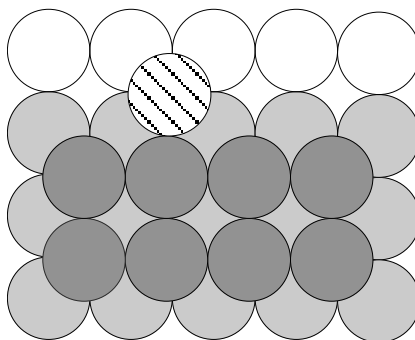


Figure 5-8: Schematic showing example of interaction sites (empty circles) associated with edge-diffuser (striped circle).

Finally, we consider the interaction between two edge-diffusers which are on edges which are two steps away as shown in Fig. 5-7. In this case, regular KMC is used when both edge-atoms are in the “common” region (in between I & II) as shown in Fig. 5-7. Including this process is particularly important in order to properly include island coalescence in our simulations. Otherwise, FPT KMC is used with sites I and II treated as kink sites.

In order to take these interactions into account we associate each lattice site with a list of edge-diffusers it can affect. Accordingly, every time there is a change at the site all affected edge diffusers are updated. We note that all sites one step away from the edge as well as both absorption sites are linked with the edge diffuser in this way. In the case of the fcc model, all potential edge-diffuser support sites one step away from the edge (see Fig. 5-8) are also linked with the edge diffusing atom in order to properly take into account the effects of steps on “absorption”.

Time-based KMC

In order to implement our FPT approach we have used a time-based rather than a rate-based method. Thus, in addition to maintaining a list of first-passage times for all edge-diffusers, after each event we also update the total rate for all regular KMC moves $R_{KMC} = \sum n_i R_i$ (where R_i is the rate for a process of type i , and n_i is the number of processes of this type). This rate is then used to calculate the time before the next regular KMC event given by $\Delta t_{KMC} = -\ln(\xi)/R_{KMC}$ where ξ is a uniform random number between 0 and 1. This time is then compared with the time of the earliest FPT event (selected using another binary tree). If the event type corresponds to a regular KMC event, then the specific event is selected randomly from one of the possible events of this type. (We note that for the Cu/Cu(100) growth model there are 8 possible barriers and/or event-types corresponding to a binary tree of order 3.) After each event the lists containing the number and location of all regular KMC processes of each type are updated along with any changes to the neighborhood (e.g. absorption sites, length of the edge and type of boundaries) of all FPT atoms. We note that in the case of an FPT move, Eq. 5.2 is used to determine to which absorption site the edge-diffuser will “escape”.

5.4 Results

We first consider the application of our FPT KMC method to the irreversible fcc(100) growth model described in Sec. 5.2. We note that in these simulations a system size $L = 256$ was used, while the rates for monomer interlayer and intralayer

diffusion, single-bond edge-diffusion, and corner-rounding were assumed to be the same as for the EMT model (see Table 5.1) at the corresponding temperature. Figs. 5-9(a) and (b) show a comparison between regular KMC and FPT KMC results for the surface roughness or “width” (e.g. r.m.s. height fluctuation) as a function of film thickness obtained at $T = 200$ K and 250 K, while a comparison between the corresponding morphologies at $T = 200$ K and a coverage of 20 ML is shown in Fig. 5-10. As can be seen, there is excellent agreement between the KMC and FPT KMC simulation results. Similar good agreement (not shown) has also been obtained for the lateral correlation length r_c (corresponding to the first zero-crossing of the circularly-averaged height-height correlation function) as well as for the circularly-averaged height-height correlation function $G(r)$. In addition (see Table 5.2), the FPT KMC simulations at 200 (250) K are approximately 48 (75) times faster than the corresponding KMC simulations. However, due to the fact that the rate of corner diffusion also increases with increasing temperature, the increase in the speed-up factor from 200 to 250 K is not as large as the increase in the rate of edge-diffusion.

We now consider the SOS model described in Sec. 5.2. As for the generic fcc model, the rates of monomer interlayer and intralayer diffusion, single-bond edge-diffusion, and corner-rounding were assumed to be the same as for the EMT model of Cu/Cu(100) growth at the corresponding temperature. Figs. 5-9(c) and (d) show a comparison between the roughness obtained from regular KMC and FPT KMC simulations of this model at $T = 200$ K and 250 K while Figs. 5-10(c) and (d) show the corresponding morphologies at a coverage of 30 ML at $T = 200$ K. As can be

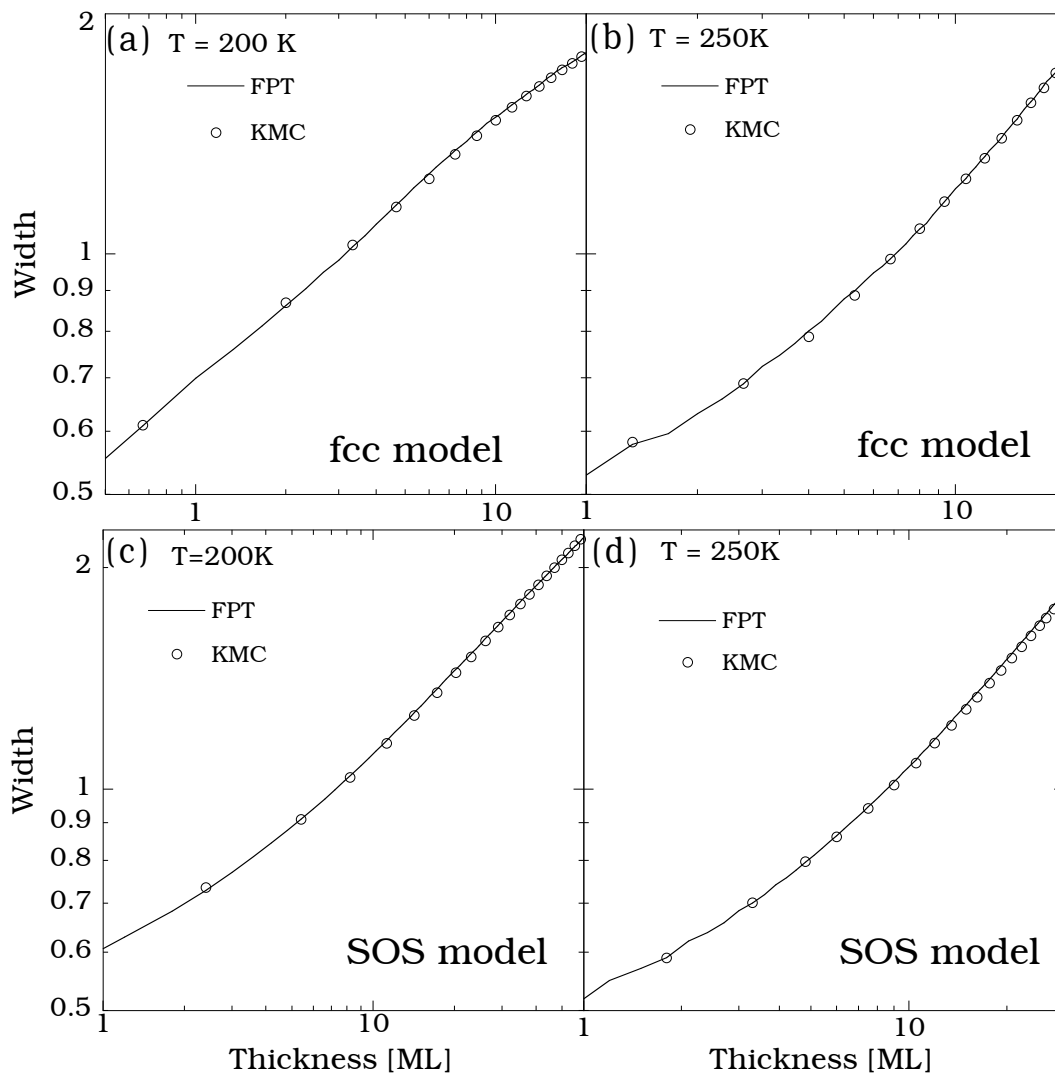


Figure 5-9: Comparison of regular KMC results (symbols) and FPT KMC results (lines) for surface roughness obtained from simulations of irreversible growth models at 200 K and 250 K.

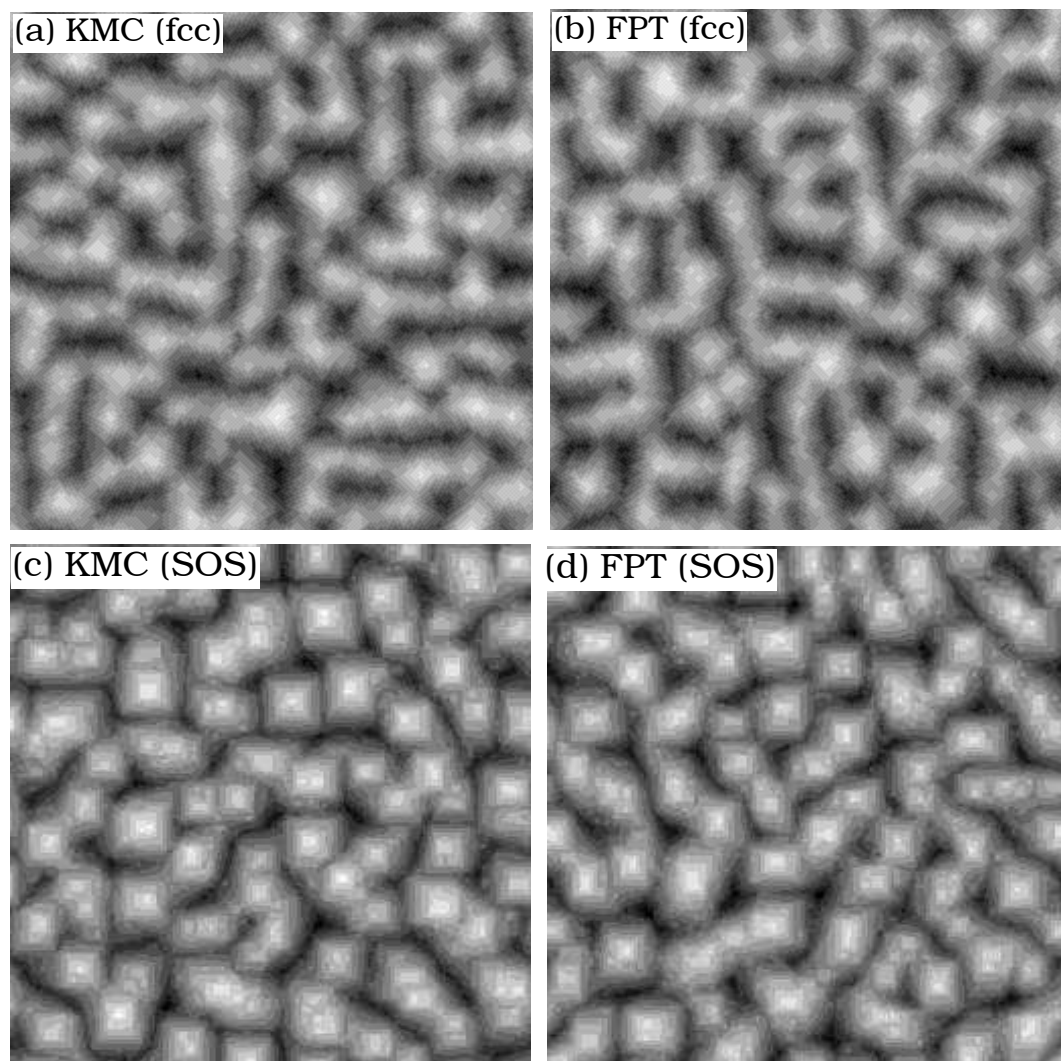


Figure 5-10: Comparison of surface morphology ($L = 256$) obtained in regular KMC (a) and FPT KMC (b) simulations of “generic” fcc model at coverage of 20 ML and regular KMC (c) and FPT KMC (d) simulations of SOS model at 30 ML.

seen, there is excellent agreement for both the surface roughness and the surface morphology. In addition, as for the fcc growth model, good agreement (not shown) has also been obtained for the lateral correlation length. We note that in this case (see Table 5.2) the speed-up factors are not quite as large as for the generic fcc growth model, but also increase with increasing temperature.

Table 5.1: Parameters used for “generic” fcc(100) and SOS models. Here D is the total rate for monomer diffusion, while D_e and D_c are the rates of edge-diffusion and corner-diffusion respectively.

Temperature	D/F	D_e/F	D_c/F
200 K	2.8×10^3	1.6×10^8	5.5×10^4
250 K	4.0×10^5	1.9×10^9	3.2×10^6

We now consider the application of our FPT KMC method to simulations of Cu/Cu(100) growth using our EMT model. We first consider growth at 200 K, since at this temperature there is negligible one-bond and two-bond detachment. As can be seen in Fig. 5-11(a), there is very good agreement between the FPT KMC results (line) and regular KMC results (symbols) for the surface roughness. As shown in Fig. 5-11(b), similarly good agreement has also been obtained for the lateral correlation length. As indicated by Figs. 5-12(a) and (b), there is also very good agreement between the morphology obtained using FPT KMC and that obtained using regular KMC. In addition, in this case the use of FPT leads to a speed-up of approximately 32 (see Table 5.2) over regular KMC.² We note that as discussed in Sec. II, in both our regular KMC and FPT KMC simulations of the EMT model, the rate of two-bond

²In particular, while a single FPT KMC simulation takes 2.3 hours on the Ohio Supercomputer Center (OSC)’s Glenn cluster, the corresponding regular KMC simulation takes over 3 days.

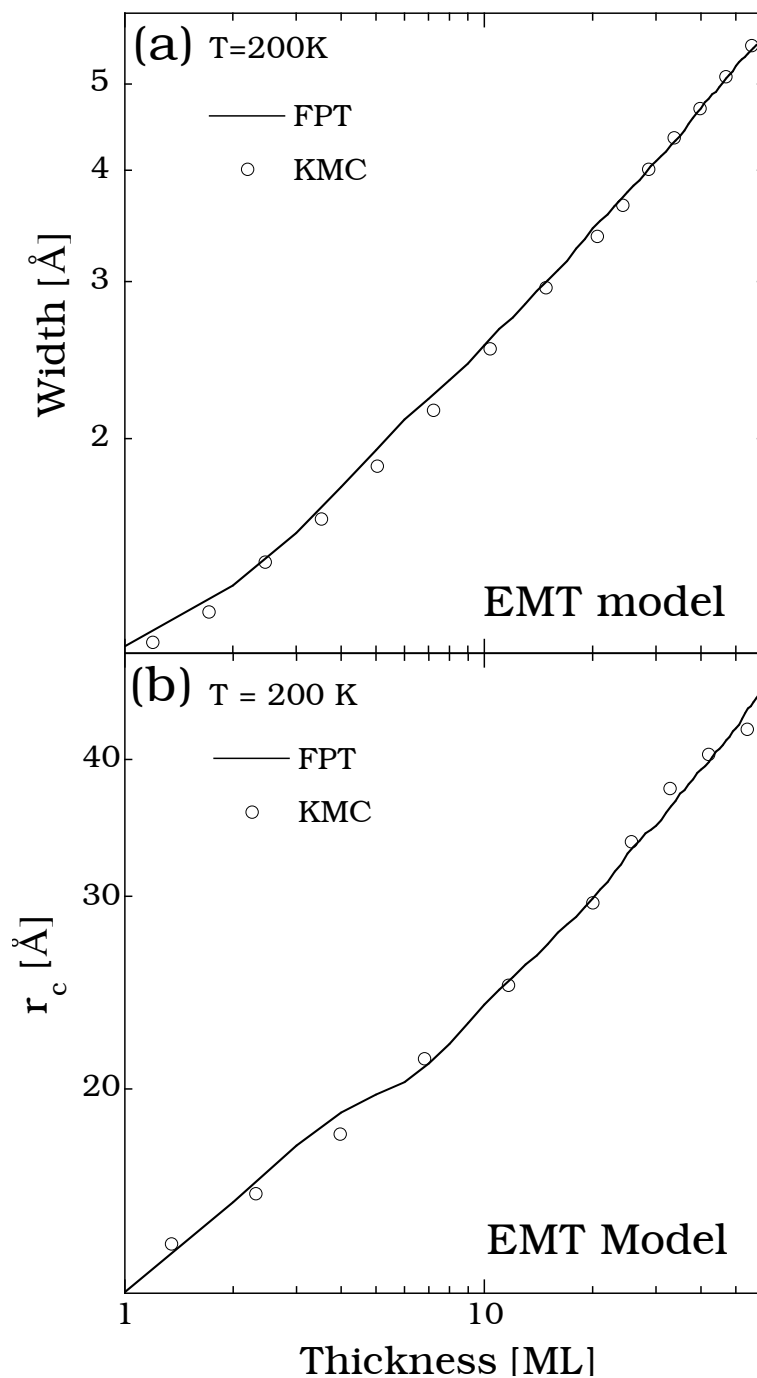


Figure 5-11: Comparison of regular KMC (symbols) and FPT KMC (lines) results for surface roughness and lateral correlation length (r_c) obtained in simulations using EMT model of Cu/Cu(100) growth at 200 K.

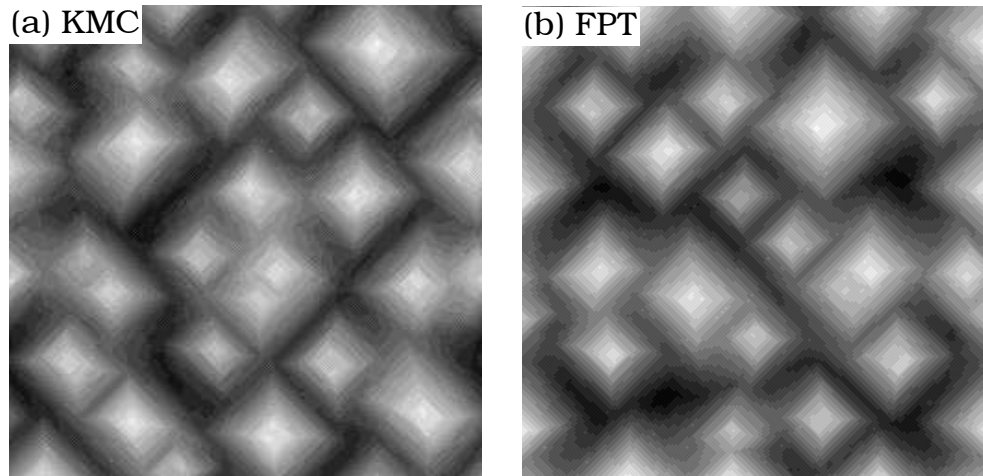


Figure 5-12: Comparison of surface morphology ($L = 256$) obtained in regular KMC (a) and FPT KMC (b) simulations of EMT model of Cu/Cu(100) growth at coverage of 60 ML.

edge-diffusion was reduced by a factor of 10 to save computer time, since two-bond edge-diffusion has almost no effect on the surface morphology. However, for comparison we have also carried out simulations at 200 K with two-bond edge-diffusion completely suppressed. While this has little effect on the surface morphology, in this case the speed-up due to FPT is even larger (approximately 60).

Finally, we consider our EMT model of Cu/Cu(100) growth at 250 K. As can be seen in Fig. 5-13 there is again very good agreement between our FPT KMC simulations and regular KMC simulations. However, due to the increased rates of double-bond edge-diffusion and corner-rounding, in this case the speed-up factor (see Table II) is not quite as large as at 200 K.

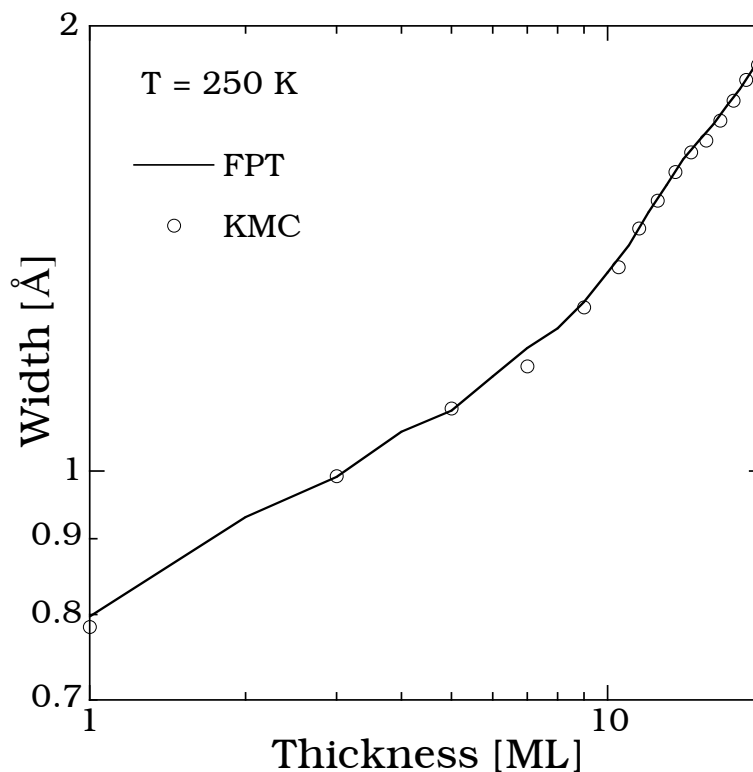


Figure 5-13: Comparison of regular KMC (symbols) and FPT KMC (lines) results for surface roughness obtained in simulations using EMT model of Cu/Cu(100) growth at 250 K.

5.5 Discussion

Motivated by the observation that in KMC simulations of growth models with fast edge-diffusion, a great deal of computer time is wasted on repetitive edge-diffusion events, we have developed a first-passage-time (FPT) method for accelerating KMC simulations. We note that while our method applies strictly only to irreversible growth (e.g. no detachment of monomers from islands) because of the relatively low detachment rate we have successfully applied it to models of reversible Cu/Cu(100) growth at 200 and 250 K. In our method, the detailed computation of edge-diffusion events is replaced by a calculation of the mean first-passage-time for an edge-diffuser to be ‘absorbed’, either by attaching to another atom near the edge, or by corner-rounding.

Table 5.2: Speed-up factors (compared to regular KMC) obtained in FPT KMC simulations of multilayer growth at $T = 200$ and 250 K using different models with Cu parameters.

Model	200 K	250 K
fcc	48	75
SOS	27	58
EMT	32	24

Accordingly, we have mapped the process of edge-diffusion to a 1D random walk between two partially absorbing boundaries. The corresponding FPT expressions for an isolated edge-diffuser were then obtained by using known expressions for the escape probabilities and mean first-passage-times for a 1D random walker, and also including corrections due to the difference in hopping rate near a corner and along an edge.

By using these expressions and also taking into account the interactions between an edge-diffuser and other atoms, we have obtained excellent agreement between our FPT KMC simulations and regular KMC simulations in both the submonolayer and multilayer regime for a variety of different growth models. These include an EMT model of Cu/Cu(100) growth as well as simpler models of irreversible growth including a generic fcc model and an SOS model. In addition, despite the additional computational overhead required to keep track of the interactions between an edge-diffuser and other atoms, we have found a significant speed-up in our FPT KMC simulations compared to regular KMC simulations. For example, in our EMT model simulations of Cu/Cu(100) growth at 200 and 250 K, we have obtained speed-up factors of 32 and 24 respectively. We note that the decrease in the acceleration factor as the temperature is increased from 200 K to 250 K is due to the increase in both the rate of corner-rounding and kink-detachment with increasing temperature.

In FPT KMC simulations of a generic fcc model with the same parameters for monomer diffusion, edge-diffusion, corner-rounding, and interlayer diffusion as in our EMT model, we have obtained even larger speed-up factors (e.g. 50 at 200 K and 75 at 250 K). Similar speed-up factors have also been obtained for the corresponding SOS model at 200 and 250 K. The larger acceleration obtained for these models is in part due to the fact that compared to the EMT model, in these models edge-diffusion plays an even more dominant role. Similarly, the increase in the FPT acceleration factor with increasing temperature is due to the increase in the rate of edge-diffusion. However, the barrier for corner-rounding also plays an important role. In particular, we expect that even larger acceleration factors may be obtained in the case of a larger corner-rounding barrier. As a test of this, we have carried out additional FPT KMC simulations of our generic fcc model at $T = 250$ K using a barrier for corner rounding which is 0.1 eV higher than the value (0.35 eV) used in the EMT model of Cu/Cu(100) growth. In this case, due to the higher barrier for corner rounding the speed-up factor was almost doubled from 75 to 140.

In addition to deriving expressions for the appropriate absorption probabilities and mean first-passage time as discussed in Sec. 5.3.2, we have also derived expressions for the conditional first-passage time (see Appendix B.3). However, we found that the use of a mean first-passage time rather than a conditional first-passage time (CFPT) provides significantly better agreement with KMC simulations. In addition, we find that CFPT KMC simulations are several times slower than the corresponding FPT KMC simulations, due at least in part to the more complicated expressions required to calculate the conditional FPT. Accordingly, here we have focused on FPT KMC

simulations and have not presented any conditional FPT KMC results.

We note that the inclusion of interactions between an edge-diffuser and other atoms turns out to be crucial in using our FPT method to obtain accurate results. This includes the interaction with other edge-diffusers on the step-edge or a nearby step-edge, and with monomers approaching the step-edge from above and below. In particular, the interaction with another edge-diffuser was included by treating the other edge-diffuser as a ‘kink’ atom and dividing the FPT by a factor of two to take into account the relative motion of both edge-diffusers. We have also assumed that by the time another atom approaches a step-edge on which there is already an edge-diffuser, this edge-diffuser is already ‘equilibrated’. This is done by randomly re-locating the edge-diffuser along the edge before re-calculating the corresponding FPT. While this ‘equilibration’ assumption does not strongly affect the surface roughness, it turns out to be crucial in obtaining good agreement with the surface morphology observed in regular KMC simulations.

Since the FPT method requires significant overhead, in both our KMC and FPT KMC simulations we have taken care to maximize the efficiency. For example, in both cases binary trees were used to select the next event. In addition, in both KMC and FPT KMC simulations the regular KMC events were organized into lists of different types in order to minimize the size of the corresponding binary tree. Nevertheless, significant additional overhead was still required in our FPT KMC simulations to keep track of the interactions between an edge-diffuser and other atoms. If in the future a more efficient method is devised to take these interactions into account then this could significantly increase the speed-up possible via FPT KMC simulations.

Since the implementation of our FPT KMC method is also relatively complex, it is of interest to compare it with simpler although perhaps less accurate methods. For example, one possible method to accelerate simulations with fast repetitive events, is to artificially reduce the rate of these events by a factor of R where $R < 1$. However, while this can lead to a speed-up of up to a factor of $1/R$, care must still be taken to ensure that detailed balance is maintained. For the models considered here which have a relatively short range of interaction, this can be done by using ‘edge-reduction’, i.e. reducing the rate of edge-diffusion for all singly-bonded edge-diffusers which are more than one hop away from a kink or other attachment site.³

Fig. 5-14 shows a comparison between the results of regular KMC simulations using the EMT model at $T = 200$ K and KMC simulations carried out using different edge-reduction factors ranging from $R = 1.0$ (no reduction) to $R = 0.01$. Also shown for comparison are results obtained using FPT KMC. As can be seen, while there is good agreement between the KMC and FPT KMC simulations, the results obtained with $R = 0.1$ and 0.01 deviate significantly from the KMC results at large thicknesses. In addition, the FPT KMC simulations are approximately 4 times faster than the edge-reduction simulations with $R = 0.1$ and are also approximately as fast as the edge-reduction simulations with $R = 0.01$. Thus our FPT KMC method provides a more accurate and efficient way to accelerate KMC simulations with fast

³In previous work,[20] a similar comparison between KMC simulations with and without ‘edge-reduction’ was also made. However, in this case detailed balance was not preserved since the hopping rate for edge-atoms one step away from a kink was reduced, while the hopping rate for kink-detachment was not reduced. This leads to even larger deviations from regular KMC results than is shown here, due to the fact that detailed balance is not preserved.

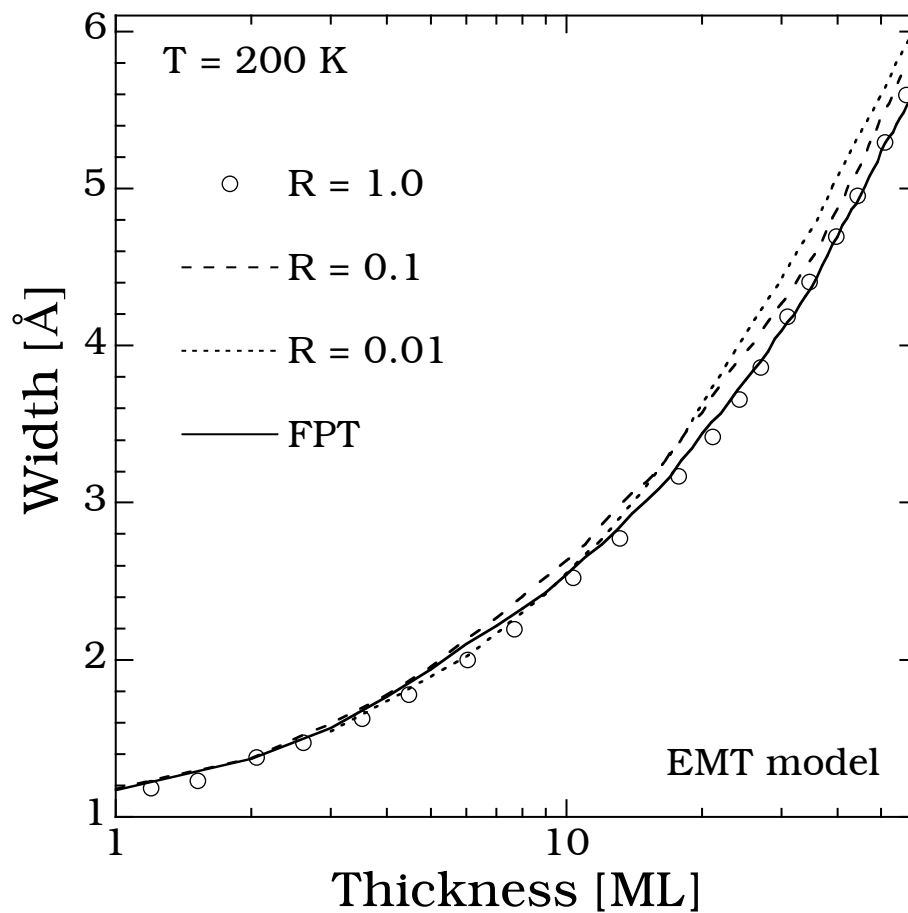


Figure 5-14: Dependence of surface roughness on edge-reduction factor R obtained in regular KMC simulations of EMT model of Cu/Cu(100) growth at 200 K.

edge-diffusion.

Finally, we note that one possible limitation of our method involves the issue of detachment of an edge-diffuser from a step-edge. In particular, while the effects of detachment are partially taken into account in our method (since the process of detachment is simulated using regular KMC) the expressions for the FPT of an edge-diffuser to be absorbed at a nearby kink or corner site are based on the assumption of negligible detachment. However, in the presence of detachment the correct mean FPT will be somewhat less than predicted by Eq. 5.3. Therefore, in order to carry out FPT KMC simulations with significant detachment it would be desirable to extend our FPT expressions to take detachment into account.

Chapter 6

Effects of Strain on Island

Morphology and Size Distribution

in Irreversible Submonolayer

Growth

6.1 Introduction

Heteroepitaxial growth is an important process [75, 76, 77] for the fabrication of nanostructures ranging from quantum wires[78] to quantum dots.[79] In many cases, the existence of strain due to lattice mismatch can lead to the formation of three-dimensional (3D) clusters, [80, 81] whose shape can depend on a variety of factors. A classic example of such 3D clusters are the (105)-facet “hut” clusters observed

in growth of Si/Ge(001). By analyzing the strain energy of a $3D$ island with a rectangular base, Tersoff and Tromp[82] have investigated the effects of biaxial strain on the equilibrium shape and aspect ratio of dislocation-free $3D$ islands. In particular, they demonstrated the existence of a shape transition such that for islands smaller than a critical size the islands are “square”, while for larger sizes the islands are elongated with a selected width which is determined by the competition between the strain and surface energies. In more recent work[83, 84] the effects of anisotropic strain on the equilibrium shape of $2D$ islands have also been studied.

While there have been extensive studies of the effects of strain on the equilibrium shape of $2D$ and $3D$ islands, there has been less work on the effects of strain on the island-shape during growth. Recently, Steinbrecher et al [85] have studied the effects of strain on the fractal growth of individual islands in the absence of island-relaxation. In their model, the elastic interaction was approximated by a $1/r^3$ interaction between the depositing monomer and the atoms of the growing island, which corresponds to the leading term in a multipole expansion of the strain energy.[86] In this case they found that the fractal dimension of the growing DLA cluster increased with strain. More recently, the strain-dependence of the island-density during irreversible submonolayer growth without island relaxation was studied[87, 88] using a model in which the elastic interaction was approximated by a $1/r^3$ interaction between all atoms on the surface. In this case the strain was found to lead to an increase in the island-density as well as the critical coverage for nucleation. Earlier, Ratsch et al [89] studied the dependence of the island-size distribution on strain in a reversible model of heteroepitaxial submonolayer growth. However, the effects of strain on the

island-shape and scaled island-size distribution in the presence of relaxation have not been studied for the case of irreversible growth. This is of particular interest since in recent work on InAs/GaAs(100) growth, it has been suggested[90] that in the early stages of growth, e.g. before the transition from $2D$ to $3D$ islands, the island-size distribution is the same as that for irreversible growth without strain, and thus serves as a template for $3D$ island formation.

Here we present the results of kinetic Monte Carlo simulations of $2D$ submonolayer growth with strain for the case of irreversible island growth (corresponding to a critical island size of 1) with rapid island relaxation due to edge- and corner-diffusion. We note that in contrast to previous studies of the effects of strain on the equilibrium island-shape,[82, 83, 84] the island-shape in our model is entirely determined by kinetic factors, and so there is no selected island-width as predicted by equilibrium calculations. In addition to studying the island-shape, including the scaled island-width and island-length distributions, we also present results for the scaled island-size distribution as a function of strain. Results for the dependence of the island-density on deposition flux are also presented.

We note that in our simulations we have approximated the elastic interaction due to strain by an isotropic $1/r^3$ interaction.[85, 87, 88] However, unlike Refs. [85, 87, 88] in which it has been assumed that the strength of the $1/r^3$ interaction is the same for all adatoms, in most of our simulations we have only included the strain interaction between island-atoms, while there is no strain interaction between monomers and other adatoms. This is motivated by the fact that the latter interaction is in general weaker than the interaction between island-atoms and may be either

attractive or repulsive depending on the system.[91] However, for comparison we have also carried out some simulations in which all adatoms, including both island-atoms and monomers, interact with the same $1/r^3$ interaction, and similar results were obtained.

6.2 Model

In order to study the effects of strain on the island morphology and island-size distribution in irreversible growth, we have carried out kinetic Monte Carlo simulations of a simple model of submonolayer growth which includes irreversible island nucleation as well as rapid island relaxation via edge- and corner-diffusion. In our model, atoms are deposited randomly on a square lattice with deposition rate F and diffuse (hop) to nearest-neighbor sites with diffusion rate D where $D = D_0 e^{-E_a/k_B T}$ in the absence of strain. In order to allow for island-relaxation, edge-diffusion of singly-bonded atoms along island edges with rate D_e in the absence of strain, and around corners with rate D_c in the absence of strain was also included. In most of our simulations we have assumed $D_c = D_e = D$ corresponding to rapid island relaxation. However, for comparison simulations were also carried out with both higher and lower rates of edge- and corner-diffusion. In order to eliminate dimer and trimer diffusion we have suppressed corner rounding for dimers and trimers.

In order to include the effects of strain in our simulations, we have approximated the strain energy by a repulsive $1/r^3$ interaction. We note that a similar approximation has been used in previous work[85, 88] and corresponds to the leading term

in a multipole expansion of the strain energy.[86] Thus, we may write for the strain energy,

$$E^{st}(\gamma) = \sum_{ij} \frac{\gamma}{r_{ij}^3} \quad (6.1)$$

where γ characterizes the strength of the elastic interaction and the sum is over all island adatoms, e.g. all adatoms with one or more nearest-neighbor in-plane bonds. We note that in contrast to previous work[85, 87, 88] the interaction due to strain between monomers (*corresponding to adatoms with no nearest-neighbor in-plane bonds*) and other adatoms is not included since this interaction is in general weaker than the interaction between island-atoms and may be either attractive or repulsive depending on the system.[91]

In order to include the effects of strain on the energy barriers for diffusion in our simulations, we have assumed that the shift in the energy barrier for hopping of an atom from site i to site j may be approximated as,

$$\Delta E_{ij}^b(\gamma) = \frac{1}{2}(E_j^{st}(\gamma) - E_i^{st}(\gamma)) \quad (6.2)$$

where $E_i^{st}(\gamma)$ is the interaction due to strain between the atom at site i and all other island-atoms. This corresponds to an estimate of the strain-induced shift in the saddle-point energy which is a linear interpolation between the corresponding energy shift at the initial site and at the final site. We note that such an interpolation is not exact, since the effect of strain at a saddle-point may be different from that at a binding site.[92, 93] However, we expect that it should be a reasonable approximation

for the “local” effects of the strain-induced interaction between an island-atom and other nearby island-atoms.¹In this connection, we note that in previous work by Fichthorn and Scheffler [16] it has been found that Eq. 6.2 is a good approximation for the “long-range” interactions between adatoms in Ag on 1-ML-Ag/Pt(111) growth. We also note that Eq. 6.2 implies the existence of an “attachment barrier” due to strain for a monomer to attach to another monomer or an existing island, and also implies a tendency for diffusing edge-atoms to diffuse “away” from other island-atoms.

Thus, in our model the rate for an atom to hop from site i to a nearest-neighbor or corner diffusion site j is given by,

$$D_{ij}(\gamma) = D_{ij}(0) \exp[-(E_j^{st} - E_i^{st})/2k_B T] \quad (6.3)$$

where $D_{ij}(0)$ is the corresponding rate in the absence of strain. As already noted, in most of our simulations we have assumed $D_{ij}(0) = D_e = D_c = D$. For simplicity, we have also assumed that atoms deposited on top of existing islands do not feel the strain interaction and that there is no barrier to interlayer diffusion at an island-edge.

Since the hopping rate of an atom may be different at every lattice site and may also depend on direction, we have used a binary tree[18] to keep track of the rates for all processes and selected kinetic Monte Carlo moves. In our algorithm, the rates for nearest-neighbor and next-nearest-neighbor hops for all sites are stored in the leaves (nodes of the lowest level) of a binary tree. Since the strain energy of an atom depends

¹Here we assume that the effect of strain on the activation barrier for an isolated monomer is already taken into account in the value of D used in our simulations

on its position relative to all other atoms on the substrate, whenever an atom moves its rate has to be re-calculated while the rates of all atoms affected by this move also have to be updated. To minimize the computation time only interactions up to a range of 25 lattice units were included during the update after each move. However, periodically the rates for all events in the system were re-calculated without any cutoff in order to eliminate any possible accumulation of errors. The interaction of an atom with all of its periodic images was included during this re-calculation by the inclusion of pre-calculated Ewald sums for each possible displacement vector within the lattice.[94]

Our simulations were carried out using a system of size $L = 256$ with periodic boundary conditions in both spatial directions, Simulations of submonolayer island growth were carried out using values of D/F ranging from $10^5 - 10^7$. Values of the strain energy parameter $\alpha = \gamma/2k_B T$ ranging from $\alpha = 0$ (no strain) to $\alpha = 2.0$ were used and our results were averaged over 30 runs.

6.3 Results

6.3.1 Monomer and island densities

We first consider the effects of strain on the island and monomer densities. Fig. 6-1 shows a log-log plot of the monomer density N_1 and island density N as a function of coverage θ for $D/F = 3 \times 10^6$ and three different values of the strain parameter α . As can be seen, with increasing strain α both the island and monomer density increase. In

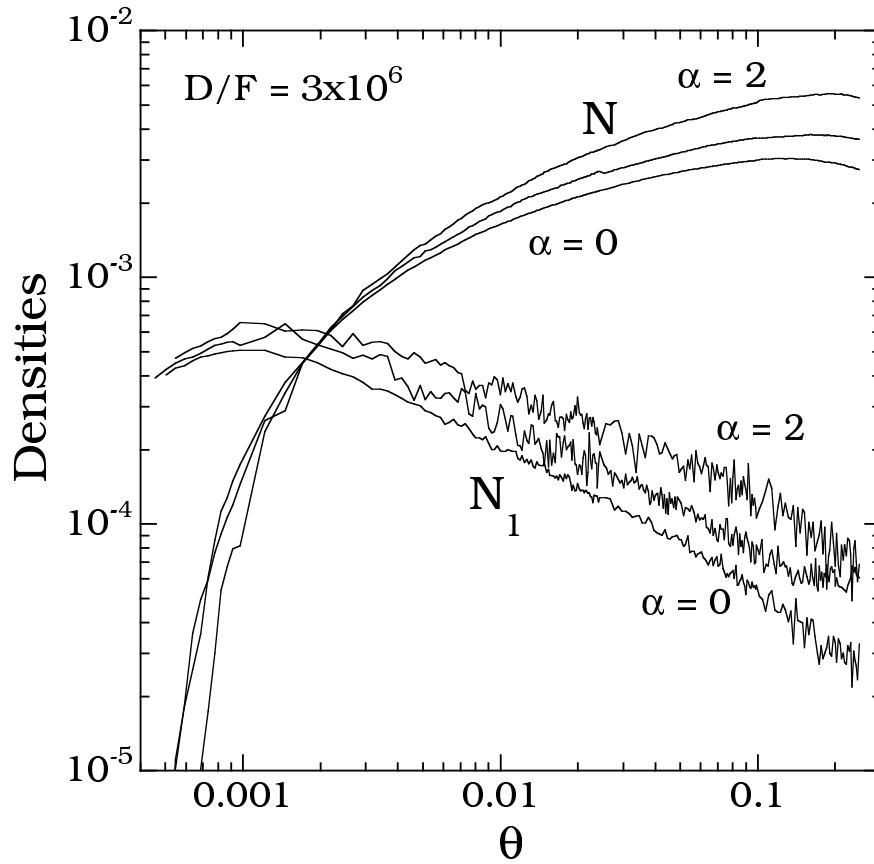


Figure 6-1: Monomer density N_1 and island density N as a function of coverage θ with $D/F = 3 \times 10^6$ for $\alpha = 0.0, 1.0, \text{ and } 2.0$.

addition, the range of the nucleation regime (corresponding to coverages for which the monomer density is larger than the island density) is pushed towards higher coverages with increasing strain. These effects are primarily due to the strain-induced barrier to dimer formation and are similar to what has been observed in previous simulations of irreversible growth with strain in the absence of island relaxation.[85] Fig. 2 shows a plot of the peak island-density as a function of D/F for different values of α . As expected, in the absence of strain ($\alpha = 0$) the value of χ is close to but slightly lower than $1/3$. However, with increasing strain, the effective value of χ decreases. Again, these results are due primarily to the strain-induced barrier to dimer nucleation and

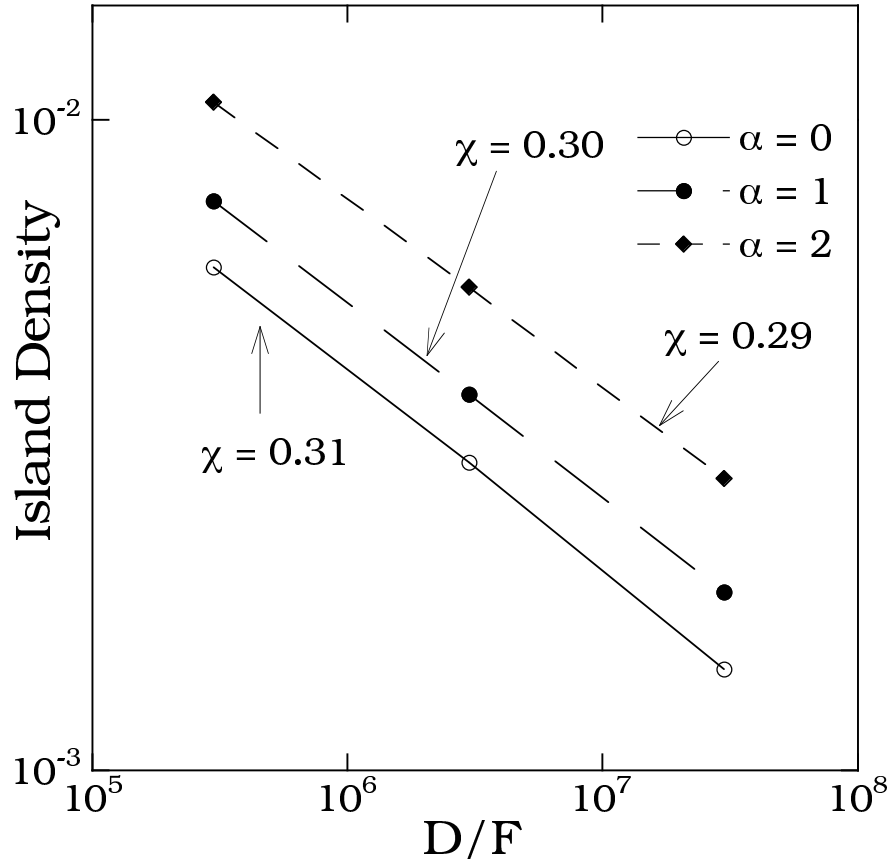


Figure 6-2: Peak island density as a function of D/F for $\alpha = 0.0, 1.0,$ and 2.0 .

are similar to what has been observed in previous simulations of irreversible growth with strain in the absence of island relaxation.[85]

6.3.2 Island morphology

We now consider the effects of strain on the island morphology. Fig. 6-3 shows typical pictures of the island shapes both with and without strain obtained in our simulations for the same parameters as in Fig. 6-1 ($D/F = 3 \times 10^6, \alpha = 0 - 2$). As can be seen, in the absence of strain (Fig. 6-3(a), $\alpha = 0$) but in the presence of relaxation due to edge-and-corner diffusion, square islands are obtained. In contrast,

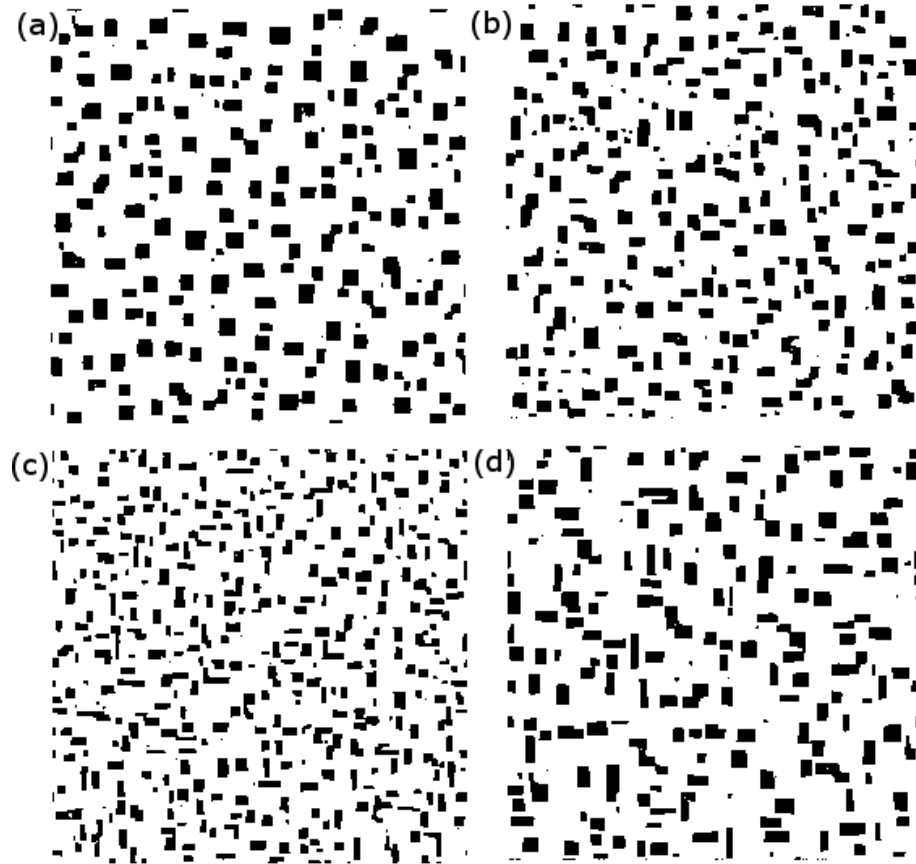


Figure 6-3: Island morphology for coverage $\theta = 0.2$ with $D/F = 3 \times 10^6$ for strains (a) $\alpha = 0.0$ (b) $\alpha = 1.0$ (c) $\alpha = 2.0$ (d) $D/F = 3 \times 10^7$ for strain $\alpha = 2.0$

in the presence of sufficient strain, the island-size is smaller due to the increased island-density while the island-shape becomes significantly more rectangular. Also shown in Fig. 6-3(d) is a picture for a somewhat larger value of D/F (3×10^7) with $\alpha = 2$. In this case the average island is somewhat larger than in Fig. 6-3 (c). We also note that while the largest islands tend to be rectangular, the smaller islands are a mixture of square and rectangular islands.

In order to quantify the island morphology we have measured the average aspect ratio $\langle A_r \rangle$, corresponding to the average over all islands of the ratio of the range in the

long (x or y) direction to the range in the short direction. Fig. 6-4 shows typical results for the average aspect ratio as a function of strain at coverage $\theta = 0.2$ for different values of D/F . As can be seen, the average aspect ratio increases significantly with increasing strain. Interestingly, even for the case of zero strain ($\alpha = 0$) the average aspect ratio is slightly higher than 1 due to fluctuations. Fig. 6-4 also indicates that, in general, the aspect ratio also increases with increasing D/F for fixed D_e as well as with increasing relaxation rate D_e for fixed D/F for $D_e \leq D$. Also shown in Fig. 6-4 are results for $D_e = 10D$ with $D/F = 3.0 \times 10^6$ (open diamonds). As can be seen in this case, due to the very high rate of edge-diffusion, the island aspect-ratio appears to have saturated, i.e. increasing the rate of edge diffusion does not lead to an increased aspect ratio.

In order to quantify more precisely the island morphology we have also measured the aspect ratio distribution $P(A_r) = N(A_r)/N$ where $N(A_r)$ is the density of islands with aspect ratio A_r and N is the total island density. Fig. 6-5 shows a comparison of the aspect ratio distributions both with and without strain at $\theta = 0.2$ with $D/F = 3 \times 10^6$. Due to the equivalence between the x and y directions, both distributions are symmetric about $A_r = 1$. We note that even for the case without strain ($\alpha = 0$), the aspect ratio distribution has a finite width due to fluctuations. However, with increasing strain the peak at $A_r = 1$ decreases significantly while the width of the aspect ratio distribution increases, thus indicating a significant increase in the island anisotropy.

In order to further quantify the island morphology we have also measured the

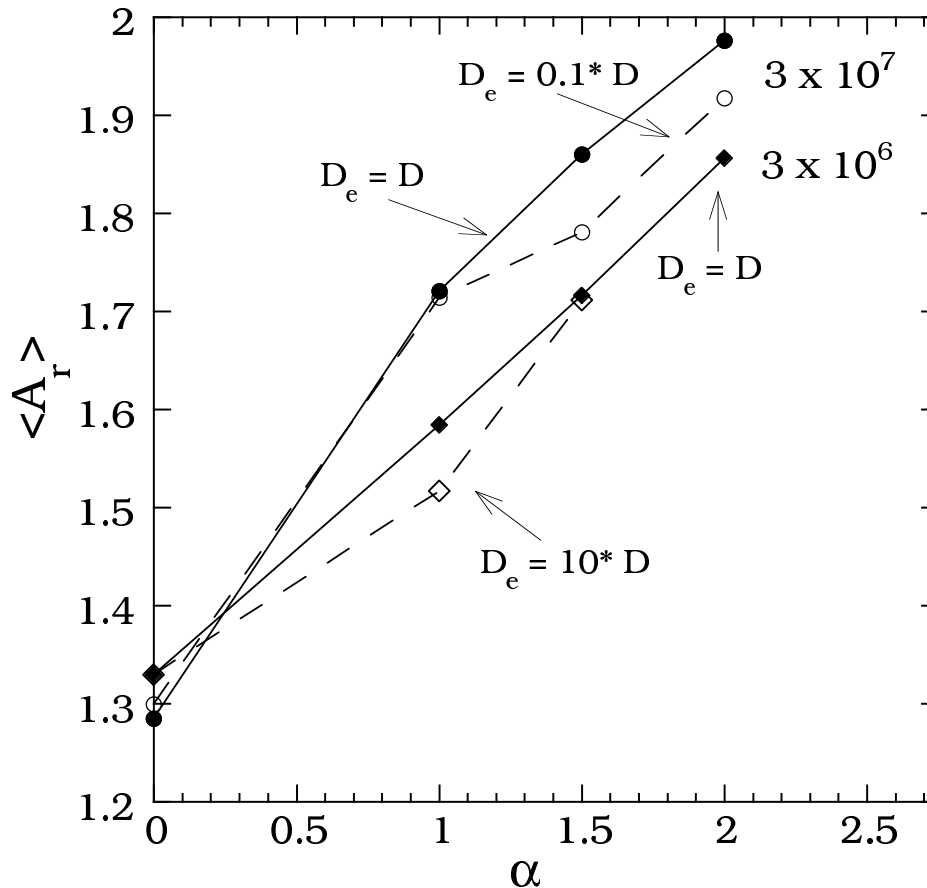


Figure 6-4: Average aspect ratio $\langle A_r \rangle$ for $D/F = 3 \times 10^6$ (diamonds) and 3×10^7 (circles) at coverage $\theta = 0.2$ as a function of strain α .

scaled island-width and scaled island-length distributions. As already noted, in previous work on the equilibrium island-shape for 2D islands[83, 84] and 3D islands[82] in the presence of strain, it was found that for islands larger than a critical size, the islands will be rectangular with a selected width which is determined by a competition between the surface energy of an island and the strain energy. In contrast, in our non-equilibrium simulations the surface or lateral-bond energy does not play a direct role, and as a result fluctuations are likely to be significantly more important.

We first consider the scaled island-width distribution, where the island-width is defined as the smallest of the lengths corresponding to the range of the island in the

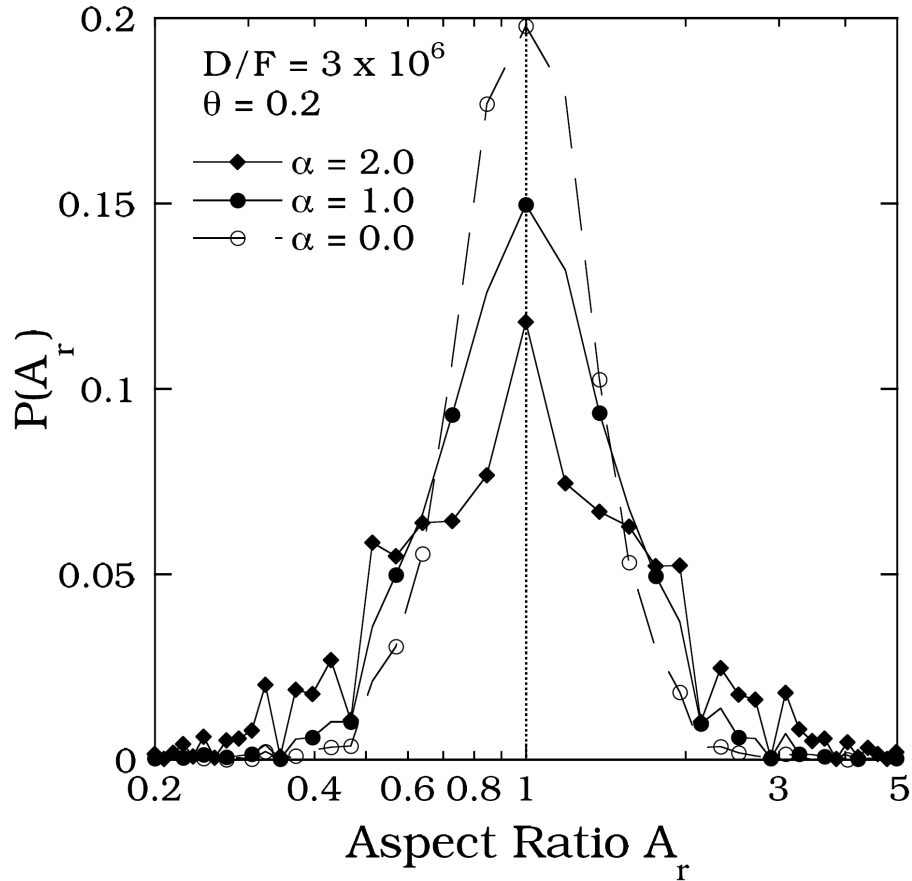


Figure 6-5: Aspect ratio distribution $P(A_r)$ for coverage $\theta = 0.2$ at $D/F = 3 \times 10^6$ for strains (a) $\alpha = 0.0, 1.0,$ and 2.0 .

x and y directions. Assuming scaling with the average island-width W , we may write $N_w(\theta) = A(\theta, W)f_w(w/W)$ where $N_w(\theta)$ is the density of islands with width w , and $f_w(w/W)$ is the island-width distribution scaling function. Using this definition for the scaling function one may write,

$$N(\theta) = A(\theta, W) \sum_w f_w(w/W) \simeq A W \int_0^\infty f_w(u) du \quad (6.4)$$

Assuming the normalization $\int_0^\infty f_w(u) du = 1$ implies $A(\theta, W) = N(\theta)/W$. We thus

obtain the general scaling form for the island-width distribution,

$$f_w(w/W) = WN_w(\theta)/N(\theta) \quad (6.5)$$

Fig. 6-6 shows typical results for the scaled island-width distribution $f_w(w/W)$ both with and without strain over a range of coverages up to $\theta = 0.2$. As can be seen in both cases there is excellent scaling, i.e. the scaled island-width distribution is independent of coverage. However, in contrast to the predictions of Tersoff and Tromp[82] for the equilibrium island shape, the scaled island-width distribution is relatively broad even in the presence of strain. In addition, the scaled island-width distribution depends only weakly on strain, i.e. the scaled island-width distribution is slightly less sharply peaked in the presence of strain than in the absence of strain.

We have also carried out similar measurements for the scaled island-length distribution. However, in this case we found that the distribution does not scale with the average island-length L although it does scale with the peak island length l_{pk} . Accordingly, one may write for the island-length distribution scaling function,

$$f_l(l/l_{pk}) = l_{pk}N_l(\theta)/N(\theta) \quad (6.6)$$

As shown in Fig. 6-7, there is again excellent scaling as a function of coverage. However, in this case the peak of the scaled island-length distribution is significantly lower in the presence of strain than in the absence of strain.

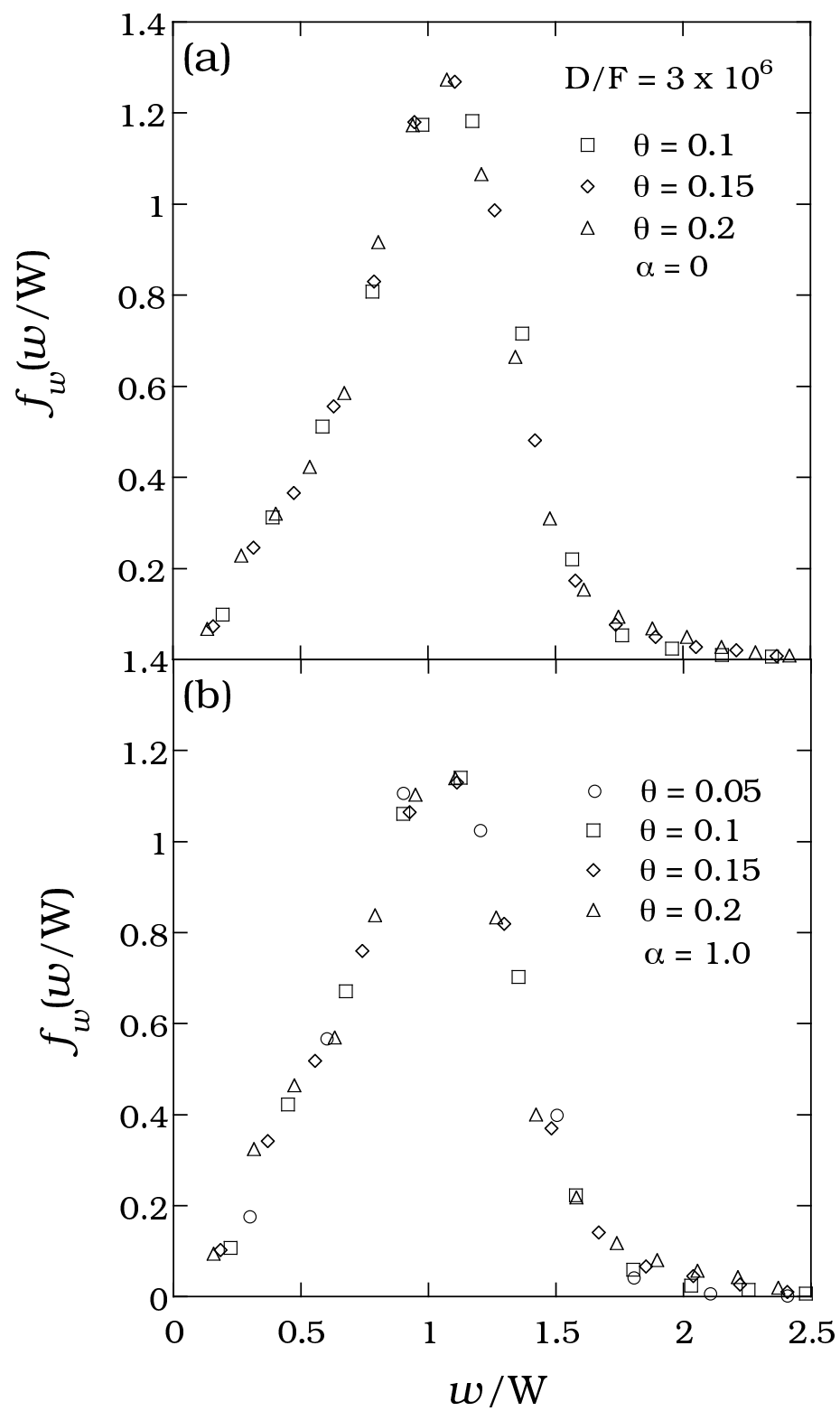


Figure 6-6: Scaled island-width distribution $f_w(w/W)$ for different coverages with $D/F = 3 \times 10^6$, (a) $\alpha = 0$ (b) $\alpha = 1.0$

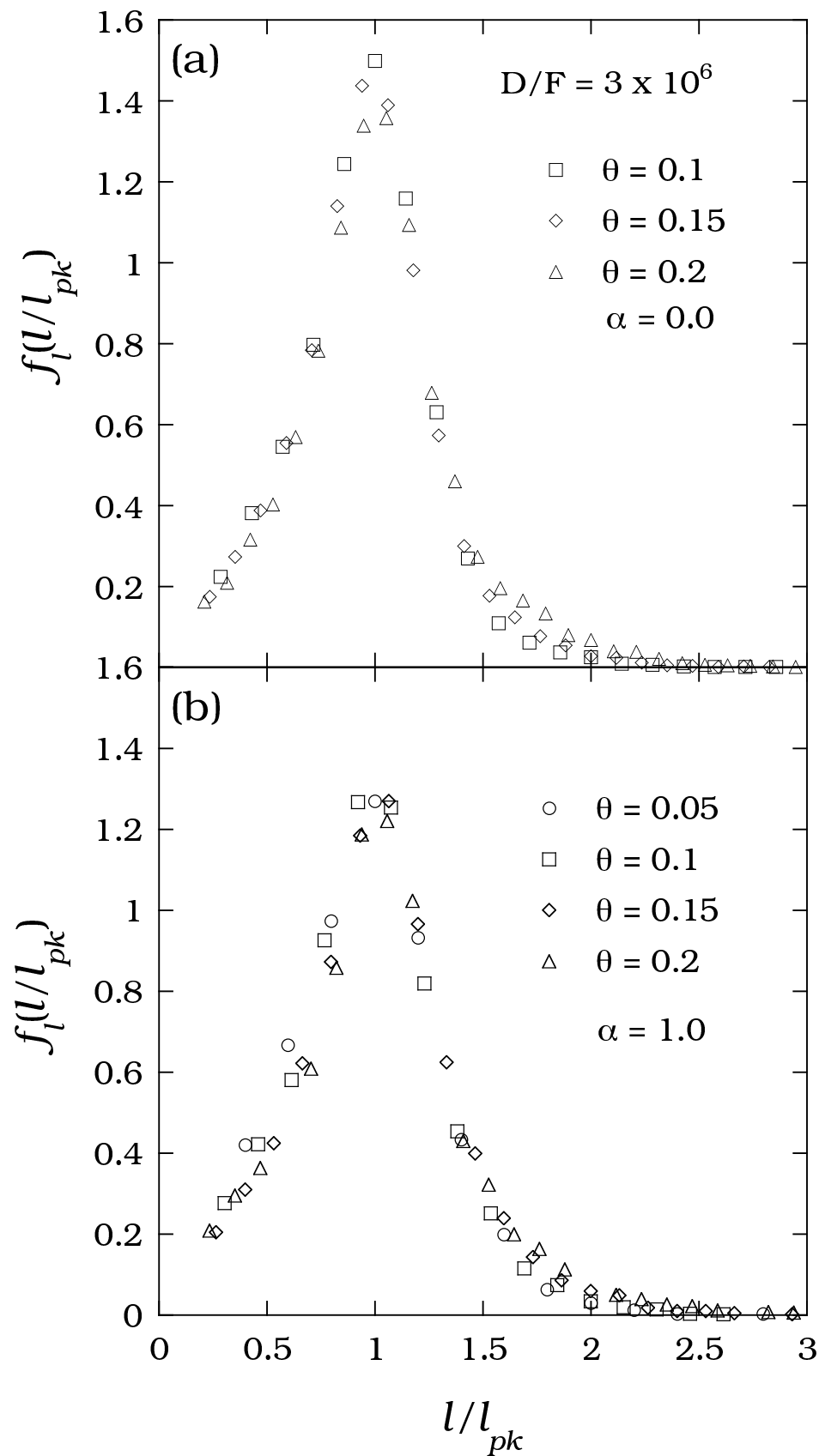


Figure 6-7: Scaled island-length distribution $f_l(l/l_{pk})$ for different coverages with $D/F = 3 \times 10^6$, (a) $\alpha = 0$ (b) $\alpha = 1.0$

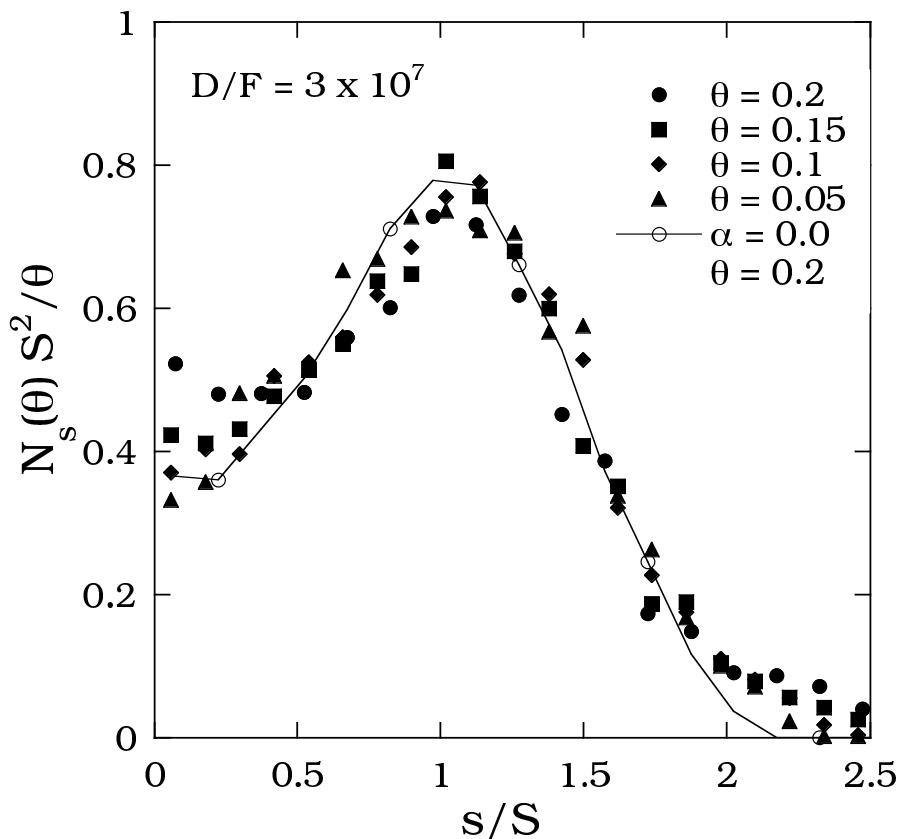


Figure 6-8: Scaled island-size distribution with $D/F = 3 \times 10^7$, $\alpha = 2.0$ and coverages ranging from $\theta = 0.05$ to $\theta = 0.2$.

6.3.3 Island-size distribution

We now consider the effects of strain on the scaled island-size distribution (ISD). This is of particular interest because it has recently been suggested[90] that the $2D$ island-size distribution in the early stages of heteroepitaxial growth may play an important role in determining the $3D$ distribution.

Fig. 6-8 shows the scaled ISD for the case of large strain ($\alpha = 2.0$, $D/F = 3 \times 10^7$) over a range of coverages ranging from 0.05 to 0.2 (solid curve). As can be seen, there is relatively good scaling as a function of coverage. For comparison the scaled ISD in

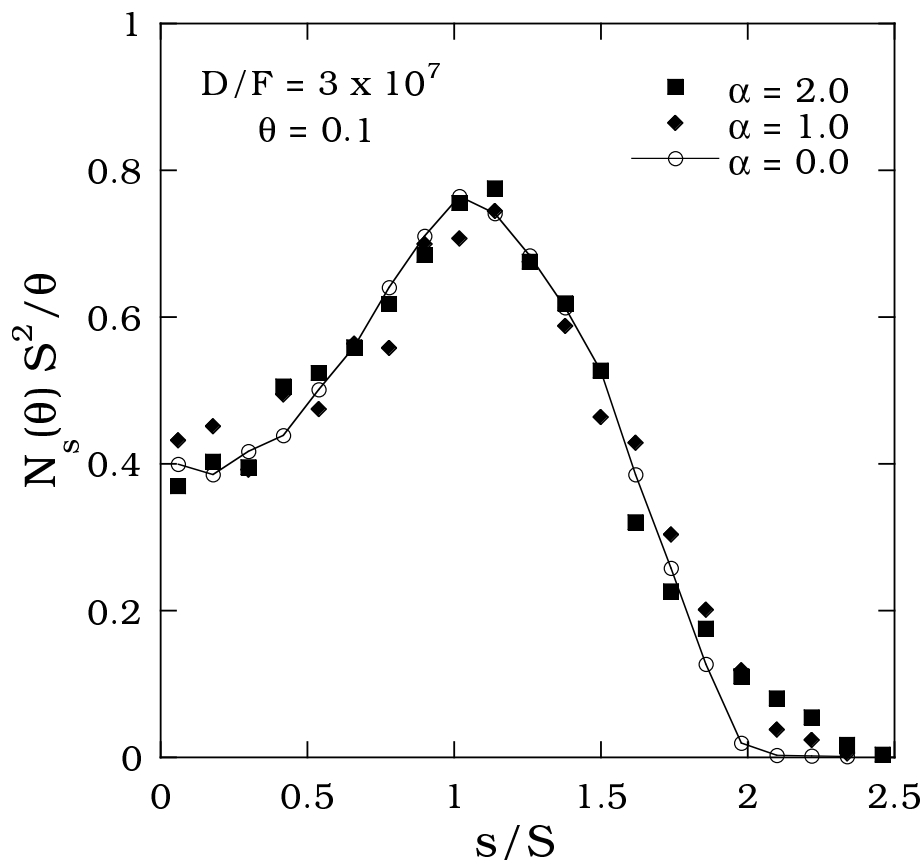


Figure 6-9: Scaled island-size distribution with $D/F = 3 \times 10^7$ at coverage $\theta = 0.1$ for $\alpha = 0, 1.0$ and 2.0 .

the absence of strain is also included (open symbols) at coverage $\theta = 0.1$. As can be seen, there is very little difference between the strained and unstrained results. We note however, that due to enhanced coalescence the strained ISD has a slightly longer tail than the ISD without strain. In addition, with increasing coverage, the scaled ISD in the presence of strain develops a small peak for small scaled island-size. We attribute this to the delayed nucleation and growth of small islands due to strain.

The dependence of the scaled ISD on strain at fixed coverage ($\theta = 0.1$) is shown in Fig. 6-9. As can be seen, there is only a relatively weak dependence of the scaled ISD on strain. We thus conclude that in the case of irreversible growth with fast island

relaxation the scaled ISD is only weakly affected by the presence of strain.

6.4 Conclusion

Using an isotropic $1/r^3$ approximation for the strain interaction, we have studied the effects of strain on the island morphology and size distribution for the case of irreversible island growth with rapid island relaxation. Consistent with previous results obtained in the absence of island relaxation,[\[87\]](#) we find that due to the increase in the barriers to dimer formation and island growth, the nucleation regime increases with increasing strain while the island and monomer densities also increase. However, only a small decrease in the effective island-density scaling exponent χ is observed. Our results also indicate that in the presence of sufficient strain and relaxation due to edge-diffusion, the island-shape becomes anisotropic. In particular, the average island aspect ratio $\langle A_r \rangle$ increases approximately linearly with strain. For a fixed strain, the anisotropy also increases with increasing edge-diffusion but eventually saturates for large edge-diffusion.

In contrast to previous work on the equilibrium island shape in the presence of strain,[\[82\]](#) we find that in the case of irreversible growth with rapid island relaxation, fluctuations play an important role. As a result there is a relatively broad distribution of anisotropies as well as a broad distribution of island-widths. We have also derived general scaling forms for the island-width and island-length distributions. In particular, the scaled island-width distribution appears to be independent of coverage and to depend only weakly on strain. For the case of the island-length distribution we found

that the distribution does not scale with the average island-length although it does scale with the peak island-length. The resulting scaled island-length distribution is again independent of coverage but depends weakly on the amount of strain.

We have also studied the dependence of the scaled island-size distribution on strain. Somewhat surprisingly, we find that the scaled ISD is only weakly affected by the presence of strain. This is consistent with recent experimental results for the scaled ISD for GaAs/GaAs(001) and InAs/GaAs(001)[95, 96] in which no difference was found between the homoepitaxial and heteroepitaxial cases. We note, however, that in these experiments the resulting scaled ISD is somewhat different from that obtained here due to the anisotropy of the underlying substrate. In the future, it would be interesting to study the effects of strain on the ISD in the case of reversible growth, since in this case the effects of fluctuations are likely to be significantly reduced.

Finally, we note that the values of the strain energy considered in our simulations are quite large compared, for example, to typical strain energies in metal heteroepitaxial growth. As an example, for the case of Cu/Ni(100) submonolayer growth, in which strain relief via island ramification was observed for the case of reversible island growth, a strain interaction energy of approximately 0.015 eV per island atom was estimated[97] which corresponds roughly to $\alpha = \gamma/2k_B T \simeq 0.1$. Since for the values of D/F used in our simulations (see Fig. 6-4) the island anisotropy is relatively low for this value of α (but increases significantly with D/F) this suggests that in order to observe large island anisotropy due to strain for the case of irreversible growth, relatively large values of D/F are required.

Chapter 7

Conclusions and Future Work

In this Thesis we have developed and applied several different methods to extend the length and time scales of kinetic Monte Carlo (KMC) simulations of non-equilibrium processes such as thin film growth and island coarsening. This includes the development of parallel algorithms for kinetic Monte Carlo, as well as the development of a first-passage time (FPT) approach to KMC simulations of metal (100) multilayer growth. In addition, we have applied a variety of methods to increase the accuracy of kinetic Monte Carlo simulations. This includes the use of a large database (obtained from self-learning KMC simulations) which includes concerted small-cluster processes in addition to a large number of simpler processes, as well as the inclusion of long-range interactions in KMC simulations of heteroepitaxial submonolayer island growth. Using these methods we have carried out realistic simulations of a variety of different processes related to thin-film growth and island coarsening.

We now consider some possible extensions to the work presented here. One important possible extension is the development of an “off-lattice” version KMC. The

development of such an off-lattice KMC method would greatly extend the applicability of SLKMC to amorphous systems as well as heteroepitaxial growth. Another important extension is the derivation of FPT expressions which explicitly take detachment into account, since this would allow us to accurately accelerate KMC simulations at higher temperatures when detachment plays a more important role. Finally, we note that recently Aqua et al [98] have developed a more accurate method to calculate the strain energy in submonolayer growth. Therefore, it would be of interest to compare results obtained using this method with those obtained here. In addition, since reversibility becomes important at higher temperatures, it would also be of interest to study the effects of strain on submonolayer island growth in the case of reversible island growth. Since such simulations are likely to be quite challenging, the extension of our parallel KMC methods to handle long-range interactions would also be of interest.

Appendix A

Ewald Sums

In various situations we require the energy of infinite periodic two-dimensional arrays of particles interaction via the R^{-3} dipole potential. In this section we show the derivation of the formula we used in our KMC simulations of $2D$ submonolayer growth with strain for the case of irreversible island growth as shown in [94]. We note that this derivation is for Ewald sums for the case of dipole-dipole interaction in two-dimensional systems with periodicity in both the directions.

The sum of the interaction energy of one tagged dipole with all other parallel dipoles in a periodic array converges quite slowly, roughly as

$$2\pi \int^{R_{max}} dr \frac{r}{r^3} \sim R_{max}^{-1} \quad (\text{A.1})$$

where R_{max} is the distance from the tagged dipole where the sum is truncated. Therefore, it is important to recast the sum in a form in which convergence is enhanced. In

the limit that the number of images become infinite, the energy per image becomes

$$E = \frac{1}{2} \sum_{i,j=1}^{\infty} \bar{\nu}(r_{ij}) \quad (\text{A.2})$$

and we are left with the problem of evaluating $\bar{\nu}(r_{ij})$.

$$\bar{\nu}(r_{ij}) = \sum'_{n_x n_y = -\infty}^{\infty} \left[(x_{ij} - n_x l_x)^2 + (y_{ij} - n_y l_y)^2 \right]^{-3/2} \quad (\text{A.3})$$

where $x_{ij} = x_i - x_j$ and n_x and n_y are number of images in x and y directions. where l_x and l_y are dimensions of the unit cell in x and y directions. The prime indicates that the $n_x = n_y = 0$ term should be omitted when $r_{ij} = 0$. Since the particle does not interact with its own image derivation for the case of $r_{ij} = 0$ is omitted. When $r_{ij} \neq 0$ there is not restriction on the sum over n_x and n_y in Eq. A.3. By factoring l_y we can rewrite Eq. A.3 as

$$\nu(r_{ij}) = \frac{1}{l_y^3} \sum_{n_x n_y = -\infty}^{\infty} \left[\left(\frac{x_{ij} - n_x l_x}{l_y} \right)^2 + \left(\frac{y_{ij} - n_y l_y}{l_y} \right)^2 \right]^{-3/2} \quad (\text{A.4})$$

The sum over n_y can be written as

$$\frac{1}{l_y^3} \sum_{n_y = -\infty}^{\infty} [t_1^2 + (t_2 - n_y)^2]^{-3/2} = \sum_{n = -\infty}^{\infty} f(n) \quad (\text{A.5})$$

where $\frac{x_{ij} - l_x n_x}{l_y} = t_1$ and $\frac{y_{ij}}{l_y} = t_2$. Using poisson sum formula equation(A.13) we

we can rewrite the above equation as

$$\sum_{n=-\infty}^{\infty} f(n) = \sum_{k=-\infty}^{\infty} \int_{-\infty}^{\infty} [t_1^2 + (t_2 - x)^2]^{-3/2} e^{-2\pi i k x} dx \quad (\text{A.6})$$

By replacing $t_2 - x$ with t_3 and dx with $-dt_3$ we can rewrite the above equation as

$$\begin{aligned} \sum_{n=-\infty}^{\infty} f(n) &= \sum_{k=-\infty}^{\infty} \int_{-\infty}^{\infty} [t_1^2 + t_3^2]^{-3/2} e^{-2\pi i k (t_2 - t_3)} dt_3 = \sum_{k=-\infty}^{\infty} e^{-2\pi i k t_2} \int_{-\infty}^{\infty} [t_1^2 + t_3^2]^{-3/2} e^{2\pi i k t_3} dt_3 \\ \sum_{n=-\infty}^{\infty} f(n) &= \sum_{k=-\infty}^{\infty} e^{-2\pi i k t_2} 2 \int_0^{\infty} (t_1^2 + t_3^2)^{-3/2} \cos(2\pi k t_3) dt_3, \end{aligned} \quad (\text{A.7})$$

Integral with $\sin(2\pi k x)$ is equal to zero since its integrand is *odd*. Using equation(??)

we get

$$\int_0^{\infty} \frac{\cos(2\pi k t_3)}{(t_1^2 + t_3^2)^{3/2}} = \frac{2\pi k}{t_1} K_1(2\pi k t_1) = f_k(t_1) \quad (\text{A.8})$$

Where K_1 modified bessel Function of second kind of 1st order. After substituting

this back in the equation(A.7) we get

$$\begin{aligned} \sum_{n=-\infty}^{\infty} f(n) &= 2 \sum_{k=1}^{\infty} \cos(2\pi k \frac{y_{ij}}{l_y}) f_k(|\frac{x_{ij} - l_x n_y}{l_y}|) & k \neq 0 \\ &+ \frac{2}{\left(\frac{x_{ij} - l_x n_x}{l_y}\right)^2} & k = 0 \end{aligned}$$

While the term with $\sin(2\pi k x)$ is equal to zero, since the sum is symmetric on the

either side of $k = 0$. Finally, substituting every thing back in equation(A.3) $\nu(r_{ij})$ is

$$\nu(r_{ij}) = \frac{2}{l_y l_x^2} \sum_{n_x=-\infty}^{\infty} \frac{1}{\left(n_x - \frac{x_{ij}}{l_x}\right)^2}$$

$$+ \frac{2}{l_y^3} \sum_{m=1}^{\infty} \sum_{n_x=-\infty}^{\infty} \cos(2\pi m \frac{y_{ij}}{l_y}) f_m \left(\left| \frac{x_{ij} - n_x l_x}{l_y} \right| \right) \quad x_{ij} \neq 0 \quad (\text{A.9})$$

If $x_{ij} = 0$ and $y_{ij} \neq 0$ then x and y are switched in the above equation. The second term in the above equation is rapidly convergent. The first term which corresponds to the case of $m = 0$ in the Poisson sum, is Taylor expanded in the variable $t = \frac{x_{ij}}{l_x}$, ($t < 1$)

$$\begin{aligned} \sum_{n_x=-\infty}^{\infty} (n_x - t)^{-2} &= t^{-2} + \sum_{n_x=1}^{\infty} [(n_x - t)^{-2} + (n_x + t)^{-2}] \\ &= t^{-2} + \sum_{n_x=1}^{\infty} \left[\frac{2}{n_x^2} + \frac{6t^2}{n_x^4} + \left\{ (n_x - t)^{-2} + (n_x + t)^{-2} - \frac{2}{n_x^2} - \frac{6t^2}{n_x^4} \right\} \right] \\ &= t^{-2} + \frac{\pi^2}{3} + t^2 \frac{\pi^4}{15} + \sum_{n_x=1}^{\infty} \frac{2t^4(5n_x^2 - 3t^2)}{n_x^4(n_x - t)^2(n_x + t)^2} \end{aligned} \quad (\text{A.10})$$

In the last step, the leading tow non-vanishing terms were summed in closed form and the remainder, which decays as n_x^{-6} , is left as a sum over n_x . Since we have assumed that $x_{ij} \neq 0$ and $t < 1$, there is not problem with vanishing denominator in Eq. A.10 Our final expression for $\bar{v}(r_{ij})$ for $x_{ij} \neq 0$ is

$$\begin{aligned} \bar{v}(r_{ij}) &= \frac{2}{l_x^2 l_y} \left[t^{-2} + \frac{\pi^2}{3} + t^2 \frac{\pi^4}{15} + \sum_{n_x=1}^{\infty} \frac{2t^4(5n_x^2 - 3t^2)}{n_x^4(n_x - t)^2(n_x + t)^2} \right] \\ &+ \frac{2}{l_y^3} \sum_{m=1}^{\infty} \sum_{n_x=-\infty}^{\infty} \cos(2\pi m \frac{y_{ij}}{l_y}) f_m \left(\left| \frac{x_{ij} - n_x l_x}{l_y} \right| \right) \quad x_{ij} \neq 0, \end{aligned} \quad (\text{A.11})$$

Proof of Eq. A.8

The poisson sum formula is a special case of the general result

$$\sum_{-\infty}^{\infty} f(x+n) = \sum_{-\infty}^{\infty} e^{-2\pi i k x} \int_{-\infty}^{\infty} f(x') e^{-2\pi i k x'} dx', \quad (\text{A.12})$$

with $x = 0$ gives poisson summation Rule

$$\sum_{-\infty}^{\infty} f(n) = \sum_{-\infty}^{\infty} \int_{-\infty}^{\infty} f(x') e^{-2\pi i k x'} dx' \quad (\text{A.13})$$

If $f(n) = (t^2 + n^2)^{-3/2}$, using poisson sum formula (A.13) we can write

$$\sum_{n=-\infty}^{\infty} f(n) = \sum_{k=-\infty}^{\infty} \int_{-\infty}^{\infty} (t^2 + x^2)^{-3/2} e^{-2\pi i k x} dx \quad (\text{A.14})$$

using $e^{ix} = \cos(x) + i \sin(x)$ and after simplification (integral with $\sin(2\pi k x)$ is equal to zero since its integrand is *odd*) we get

$$\sum_{n=-\infty}^{\infty} f(n) = 2 \sum_{k=-\infty}^{\infty} \int_0^{\infty} (t^2 + x^2)^{-3/2} \cos(2\pi k x) dx, \quad (\text{A.15})$$

using the expression for K_ν , modified Bessel Function of second kind of ν^{th} order[99]

$$K_\nu(xz) = \frac{\Gamma(\nu + \frac{1}{2})(2z)^\nu}{x^\nu \Gamma(\frac{1}{2})} \int_0^{\infty} \frac{\cos(xt)}{(t^2 + z^2)^{\nu + \frac{1}{2}}} dt, \quad (\text{A.16})$$

and substituting $\nu = 1$ we get

$$\int_0^\infty \frac{\cos(2\pi kt)}{(t^2 + z^2)^{3/2}} dt = \frac{2\pi k}{z} K_1(2\pi kz) \quad (\text{A.17})$$

and for the case of $k = 0$ integral in the Eq. A.15 is equal to $\frac{2}{t^2}$

After substituting above expressions in the equation (A.15) we get

$$\sum_{n=-\infty}^{\infty} (t^2 + n^2)^{3/2} = \begin{cases} \sum_{k=-\infty}^{\infty} \frac{4\pi k}{t} K_1(2\pi kt) & k \neq 0 \\ \frac{2}{t^2} & k = 0 \end{cases} \quad (\text{A.18})$$

Appendix B

Derivation of Expressions used in FPT KMC

B.1 Mean First Passage Time

Consider a random walk (see Fig. 5-4) on the interval $[0, L]$ with partial reflection and partial absorption at each boundary. When a walker hits either $x = 0$ or $x = L$, walker is either reflected with probability $\rho (= 1 - \beta_0)$ or $\omega (= 1 - \beta_L)$ back to $x = 1$ and $x = L - 1$ or absorbed with probability $1 - \rho$ or $1 - \omega$. Mean first passage time $t(x)$ satisfies recursive relation,

$$t(x) = \frac{1}{2}(t(x+1) + \delta t) + \frac{1}{2}(t(x-1) + \delta t) \quad (\text{B.1})$$

with boundary conditions,

$$t(0) = \rho + \rho t(1) \quad (\text{B.2})$$

$$t(L) = \omega + \omega t(L - 1) \quad (\text{B.3})$$

where δt is time for individual hop and $\delta t = 1$. Using eq [B.1](#)

$$t(1) = \frac{1}{2}t(2) + \frac{1}{2}t(0) + 1 \quad (\text{B.4})$$

Substituting for $t(1)$ by using Eq. [B.2](#) and after rearranging we get

$$t(2) = \frac{2 - \rho}{\rho}t(0) - 4 \quad (\text{B.5})$$

Similarly by using Eq. [B.1](#), Eq. [B.2](#) and Eq. [B.5](#) we can write

$$t(3) = \frac{3 - 2\rho}{\rho}t(0) + 9 \quad (\text{B.6})$$

Accordingly, we can write expressions for $t(4)$, $t(5)$ and so on in terms of $t(0)$. Finally, by observation, we can write a general expressions for first passage times as a function x in terms of $t(0)$.

$$t(x) = \left(1 + \left(\frac{1 - \rho}{\rho}\right)x\right)t(0) - x^2 \quad (\text{B.7})$$

Now substituting $x = L$ and $L - 1$ in Eq. [B.7](#) we get,

$$t(L) = \left(1 + \left(\frac{1 - \rho}{\rho}\right)L\right)t(0) - L^2 \quad (\text{B.8})$$

$$t(L - 1) = \left(1 + \left(\frac{1 - \rho}{\rho}\right)(L - 1)\right)t(0) - (L - 1)^2 \quad (\text{B.9})$$

Using Eq. B.3, Eq. B.8 and Eq. B.9 and solving for $t(0)$ we get

$$t(0) = \frac{\frac{L\rho}{1-\rho}(L + \frac{2\omega}{1-\omega})}{L + \frac{\rho}{1-\rho} + \frac{\omega}{1-\omega}} \quad (\text{B.10})$$

Substituting $t(0)$ from Eq. B.10 in Eq. B.7 and after rearranging and rewriting $\eta_0 = \rho/(1-\rho)$ and $\eta_L = \omega/(1-\omega)$, the expression for mean first passage time (Eq. 5.3) is given as,

$$t(x) = \frac{L(L + 2\eta_L)(x + \eta_0)}{L + \eta_0 + \eta_L} - x^2 \quad (\text{B.11})$$

B.2 Absorption Probabilities

$P_k(x)$ ($= P_k(x, L, \eta_0, \eta_L)$) is the probability of absorption at site k given that walker is initially at site x . Similarly $P_0(x)$ ($= P_0(x, L, \eta_0, \eta_L)$) is the absorption probability that walker is absorbed at $x = 0$ while $P_L(x)$ ($= P_L(x, L, \eta_0, \eta_L)$) is the the absorption probability that walker is absorbed at $x = L$ if walker is initially at site x . Absorption probability to the left satisfies recursive relation,

$$P_0(x) = \frac{1}{2}P_0(x+1) + \frac{1}{2}P_0(x-1) \quad (\text{B.12})$$

With boundary conditions,

$$P_0(0) = (1-\rho) + \rho P_0(1) \quad (\text{B.13})$$

$$P_0(L) = \omega P_0(L-1) \quad (\text{B.14})$$

Using Eq. B.12 and Eq. B.13 we can write

$$P_0(2) = P_0(0) \left(\frac{2 - \rho}{\rho} \right) - 2 \left(\frac{1 - \rho}{\rho} \right) \quad (\text{B.15})$$

Using Eq. B.12, Eq. B.13 and Eq. B.15 we can write

$$P_0(3) = P_0(0) \left(\frac{3 - 2\rho}{\rho} \right) - 3 \left(\frac{1 - \rho}{\rho} \right) \quad (\text{B.16})$$

Similarly, we can also write expressions for $P_0(4)$, $P_0(5)$ and so on in terms of $P_0(0)$.

Finally, from these expressions we can write a general expression for $P_0(x)$ in terms of $P_0(0)$ as,

$$P_0(x) = \left(\frac{x - (x - 1)\rho}{\rho} \right) P_0(0) - x \left(\frac{1 - \rho}{\rho} \right) \quad (\text{B.17})$$

Using Eq. B.13 and expressions for $P_0(L)$ and $P_0(L - 1)$ (from Eq. B.17) we can solve for $P_0(0)$, which is given as,

$$P_0(0) = \frac{L + \frac{\omega}{1 - \omega}}{L + \frac{\omega}{1 - \omega} + \frac{\rho}{1 - \rho}} \quad (\text{B.18})$$

substituting $P_0(0)$ in Eq. B.17 and after simplification and rewriting $\eta_0 = \rho/(1 - \rho)$

and $\eta_L = \omega/(1 - \omega)$ we get the expression for $P_0(x)$ (Eq. 5.2),

$$P_0(x) = \frac{L - x + \eta_L}{L + \eta_0 + \eta_L} \quad (\text{B.19})$$

Since $P_0(x) + P_L(x) = 1$. Absorption probability to the right boundary is given as

$$P_L(x) = \frac{x + \eta_0}{L + \eta_0 + \eta_L} \quad (\text{B.20})$$

B.3 Expression for Conditional First Passage Time

$$t(x) = P_0(x)t_0(x) + P_L(x)t_L(x) \quad (\text{B.21})$$

Where $t_0(x)$ and $t_L(x)$ are conditional mean times for the walker to be absorbed at either at $x = 0$ or at $x = L$ respectively if the walker is at x initially. We define the quantities $m_0(x) = P_0(x) t_0(x)$ and $m_L(x) = P_L(x) t_L(x)$ which satisfy the recursive relation,

$$\frac{1}{2}m_0(x+1) - m_0(x) + \frac{1}{2}m_0(x-1) = -P_0(x) \quad (\text{B.22})$$

With boundary conditions

$$m_0(1) = \frac{1}{\rho}m_0(0) - P_0(0) \quad (\text{B.23})$$

$$m_0(L-1) = \frac{1}{\omega}m_0(L) - P_0(L) \quad (\text{B.24})$$

. Using Eq. B.22 and Eq. B.23 we can write

$$m_0(2) = -2P_0(1) + \left(\frac{2-\rho}{\rho}\right)m_0(0) - 2P_0(0) \quad (\text{B.25})$$

$$\frac{1}{2}m_0(3) - m_0(2) + \frac{1}{2}m_0(1) = -P_0(2) \quad (\text{B.26})$$

Using Eq. B.22, B.23 and B.25 we get

$$m_0(3) = \left(\frac{3-2\rho}{\rho}\right)m_0(0) - 4P_0(1) - 2P_0(2) - 3P_0(0) \quad (\text{B.27})$$

Similarly we can also derive expression for $m_0(4)$ as,

$$m_0(4) = \left(\frac{4-3\rho}{\rho}\right)m_0(0) - 6P_0(1) - 4P_0(2) - 2P_0(3) - 4P_0(0) \quad (\text{B.28})$$

Using Eq. B.23 Eq. B.25 Eq. B.27 and Eq. B.28 we can write a general equation

$$m_0(x) = \left(\frac{x-(x-1)\rho}{\rho}\right)m_0(0) - 2\sum_{k=1}^{x-1}(x-k)P_0(k) - xP_0(0) \quad (\text{B.29})$$

Using Eq. B.24 and expressions for $m_0(L)$ and $m_0(L-1)$ in terms of $m_0(0)$ (obtained using Eq. B.29) we can solve for m_0^0 , which is given as,

$$m_0^0 = \frac{\rho}{1-\rho} \frac{\left(L + \frac{2\omega}{1-\omega}\right)(L^2 + 3\left(\frac{\omega}{1-\omega}\right)L - 1) + \left(L + \frac{\omega}{1-\omega}\right)(L^2 + 2)}{3\left(L + \frac{\rho}{1-\rho} + \frac{\omega}{1-\omega}\right)^2} \quad (\text{B.30})$$

After substituting expression for $m_0(0)$ (from Eq. B.30) in Eq. B.29 and after simplification we get an unique expression for $m_0(i)$.

$$m_0(x) = \frac{1}{3(L + \eta_0 + \eta_L)} \left\{ i \left[i^2 - 3\left(L + \frac{\omega}{1-\omega}\right)i - 1 \right] + \frac{\left(i + \frac{\rho}{1-\rho}\right)\psi_0(\rho, \omega)}{\left(L + \frac{\rho}{1-\rho} + \frac{\omega}{1-\omega}\right)} \right\} \quad (\text{B.31})$$

By dividing $P_0(x)$ (Eq. B.19) and and rewriting $\eta_0 = \rho/(1 - \rho)$ and $\eta_L = \omega/(1 - \omega)$ we obtain conditional first passage time to left boundary $t_0(x)$ as,

$$t_0(x) = \frac{1}{3(L + x + \eta_L)} \left\{ x \left[x^2 - 3(L + \eta_L)x - 1 \right] + \frac{(x + \eta_0)\psi(\eta_L)}{(L + \eta_0 + \eta_L)} \right\} \quad (\text{B.32})$$

where $\psi(\eta) \equiv (L + 2\eta)(L^2 + 3\eta L - 1) + (L + \eta)(L^2 + 2)$

Replacing x by $L - x$ in Eq. B.31 and interchanging η_0 and η_L an expression for $m_L(x)$ is obtained, which is given as,

$$m_x^L = \frac{1}{3(L + \eta_0 + \eta_L)} \left\{ (L - x) \left[(L - x)^2 - 3(L + \eta_0)(L - x) - 1 \right] + \frac{(L - x + \eta_L)\psi(\eta_0)}{(L + \eta_0 + \eta_L)} \right\} \quad (\text{B.33})$$

By dividing $P_L(x)$ from Eq. B.20 we obtain expression for conditional first passage time to right boundary $t_L(x)$ as,

$$t_L(x) = \frac{1}{3(x + \eta_0)} \left\{ (L - x) \left[(L - x)^2 - 3(L + \eta_0)(L - x) - 1 \right] + \frac{(L - x + \eta_L)\psi(\eta_0)}{(L + \eta_0 + \eta_L)} \right\} \quad (\text{B.34})$$

B.4 Number of times random walker reaches the boundary

Consider a random walk on the interval $[0, L]$ with partially absorbing boundaries (see Fig. 5-4). β_0 and β_L are the absorption probabilities at the boundary sites while $\eta_0 = (1 - \beta_0)/\beta_0$ and $\eta_L = (1 - \beta_L)/\beta_L$. We first consider the quantity $h_L(x, L)$ (see

Eq. 5.9) corresponding to the number of times (excluding the last time) the walker reaches the right boundary at L before it is absorbed at the right boundary. To simplify our notation we define the quantity $Q_L(x) = P_L(x, L - 1, \eta_0, 1)$ (see Eq. 5.2) corresponding to the probability that a walker initially at x reaches site L at least once. Similarly, $Q_L(L - 1) = P_L(L - 1, L - 1, \eta_0, 1)$ is the probability that a particle initially at $L - 1$ reaches site L at least once.

Probability that walker initial at x is absorbed when it reaches the right boundary the first time is $Q_L(x)\beta_L$. While the probability that walker is absorbed when it reached boundary the second time is $Q_L(x)(1-\beta_L)Q_L(L-1)\beta_L$. Similarly, probability that walker is absorbed on third attempt $Q_L(x)[(1-\beta_L)Q_L(L-1)(1-\beta_L)Q_L(L-1)]\beta_L$ and so on. One may then write,

$$h_L(x, L) = \frac{\sum_{n=1}^{\infty} n Q_L(x) [Q_L(L-1)(1-\beta_L)]^{n-1} \beta_L}{\sum_{n=1}^{\infty} Q_L(x) [Q_L(L-1)(1-\beta_L)]^{n-1} \beta_L} - 1 \quad (\text{B.35})$$

Here the factor of $Q_L(x)$ in each sum corresponds to the probability that the particle reaches L the first time, while the expression with exponent $n - 1$ corresponds to the probability that it is reflected from L and then returns to L , $n - 1$ times. The factor of β_L in each sum corresponds to the probability that it is absorbed at L the last time, while 1 is subtracted since the last time is excluded. Using Eq. 5.2 one obtains, $Q_L(x) = P_L(x, L - 1, \eta_0, 1) = \frac{x+\eta_0}{L+\eta_L}$ and $Q_L(L - 1) = P_L(L - 1, L - 1, \eta_0, 1) = \frac{L-1+\eta_0}{L+\eta_L}$. Substituting and using the formula for an infinite geometric series leads to Eq. 5.9.

$$h_L(x, L) = \eta_L \left[\frac{L - 1 + \eta_0}{L + \eta_0 + \eta_L} \right] \quad (\text{B.36})$$

Next we consider the quantity $h_L(x, 0)$ (see Eq. 5.8) corresponding to the number of times the walker reaches the left boundary at 0 before it is absorbed at the right boundary. In this case probability that walker never reaches the left boundary before it is absorbed at the right boundary is $(1 - Q_0(x))$ while the probability that walker reaches left boundary once before it is absorbed at right boundary is $Q_0(x)(1 - \beta_0)(1 - Q_0(1))$. Similarly, probability that atom reaches left boundary twice is $Q_0(x)(1 - \beta_0)[Q_0(1)(1 - \beta_0)](1 - P_0(1))$ and so on. One may then write,

$$h_L(x, 0) = \frac{Q_0(x)(1 - \beta_0)(1 - Q_0(1)) \sum_{n=1}^{\infty} n [Q_0(1)(1 - \beta_0)]^{n-1}}{1 - Q_0(x) + Q_0(x)(1 - \beta_0)(1 - Q_0(1)) \sum_{n=1}^{\infty} [Q_0(1)(1 - \beta_0)]^{n-1}} \quad (\text{B.37})$$

where $Q_0(x) = P_0(x - 1, L - 1, 1, \eta_L)$ is the probability that a walker initially at site x will reach site 0 at least once. Here the factor of $Q_0(x)$ in the numerator corresponds to the probability that a walker initially at site x will reach site 0 at least once while the factors of $1 - \beta_0$ correspond to the probability that it is reflected every time. The factors of $Q_0(1)$ in the summation correspond to the probability that the walker reaches the left boundary after being reflected from site 0, while the extra factor of $1 - Q_0(1)$ corresponds to the probability that after $n - 1$ reflections the walker is absorbed at the right boundary. Using Eq. 5.2 one obtains, $Q_0(x) = P_0(x - 1, L - 1, 1, \eta_L) = \frac{L - x + \eta_L}{L + \eta_L}$ and $Q_0(1) = P_0(0, L - 1, 1, \eta_L) = \frac{L - 1 + \eta_L}{L + \eta_L}$. Substituting and using the formula for an infinite geometric series leads to Eq. 5.9.

$$h_L(x, 0) = \frac{\eta_0(\eta_0 + 1)}{L + \eta_0 + \eta_L} \frac{L - x + \eta_L}{x + \eta_0} \quad (\text{B.38})$$

The corresponding results for $h_0(x, L)$ (Eq. B.39) corresponding to number of times walker reaches left boundary before is absorbed at the left boundary and $h_0(x, 0)$ ((Eq. B.39)) corresponding to number of times walker reaches right boundary before is absorbed at the left boundary are obtained by interchanging η_0 and η_L and replacing x with $L - x$.

$$h_0(x, 0) = \eta_0 \left[\frac{L - 1 + \eta_L}{L + \eta_0 + \eta_L} \right] \quad (\text{B.39})$$

$$h_0(x, L) = \frac{\eta_L}{\beta_L} \frac{1}{(L + \eta_0 + \eta_L)} \frac{x + \eta_0}{(L - x + \eta_L)} \quad (\text{B.40})$$

Appendix C

Characterization of Surface

Morphology

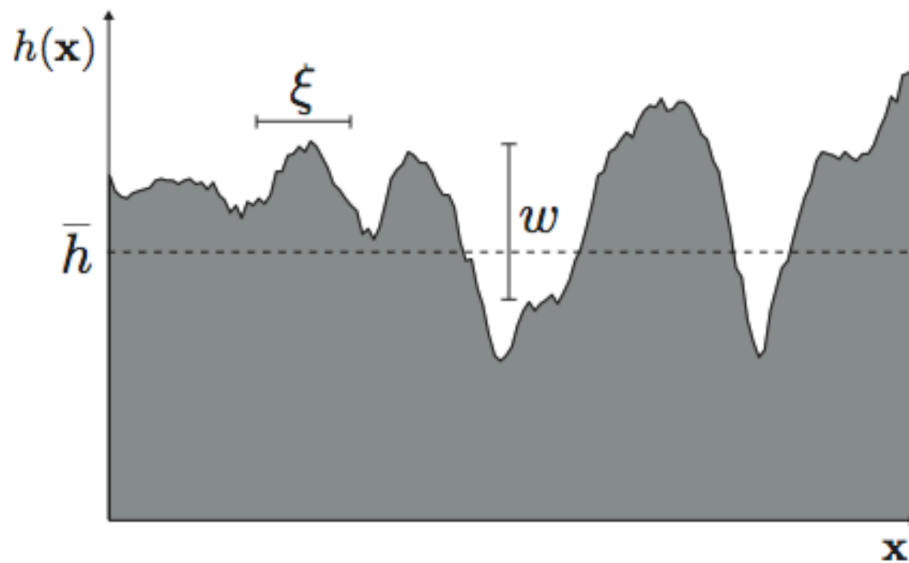


Figure C-1: Illustration of statistics used to describe rough surface. Mean height \bar{h} , interface width w , lateral correlation length ξ

The most common statistic used to describe the roughness of a surface is the standard deviation w of the surface heights $h_i(t)$ around its mean value $\overline{h(t)}$, also

called the interface width or root-mean-square (RMS) roughness. The interface width as

$$w(L, t) = \sqrt{\frac{1}{L^{d-1}} \sum_i^L [h_i(t) - \overline{h(t)}]^2} \quad (\text{C.1})$$

where L is the linear system size in d -dimensional space, $d - 1$ dimensionality of the substrate, the single-values function $h_i(t)$ describes the height of the film at the i -th location at time t , the index i labels lattice sites, and mean height of the film at time t is given as,

$$\overline{h(t)} = \frac{1}{L^{d-1}} \sum_i^L h_i(t) \quad (\text{C.2})$$

In many cases surface height fluctuations exhibit universal behavior leading to scaling in both time and space with three characteristic scaling exponents: roughness exponent α , roughening or growth exponent β , and dynamic exponent z . In case of self-affine surface, the profile of the growth interface and its properties are, generally, statistically invariant under anisotropic transformations, i.e. the length in a direction parallel to the surface is scaled by a factor and simultaneously the length in the perpendicular direction and time t are scaled by factors related to the first one.

Assuming an initially flat surface, the interface width $w(L, t)$ typically scales as a power of time in the initially stages of growth,

$$w(L, t) \sim t^\beta \quad \text{for} \quad t \ll t_X \quad (\text{C.3})$$

where β is a roughness exponent. Due to the lateral correlation in surface heights and the finite size of the system, the width eventually saturates. The saturating value of

the interface width scales with a power of the system size L ,

$$w(L, t) \sim L^\alpha \quad \text{for} \quad t \gg t_X \quad (\text{C.4})$$

where α is the roughness exponent. The crossover time t_X , at which the interface crosses from the behavior described by the Eq. C.3 to that of Eq. C.4 depends on the system size,

$$t_X \sim L^z \quad (\text{C.5})$$

where z is called dynamic exponent.

It is pointed out by Family and Viscek [100] that these three exponents α , β and z are not independent and the scaling forms for the growth and saturation of the width of the interface can be described by the following scaling relation:

$$w(L, t) \sim L^\alpha f\left(\frac{t}{L^z}\right) \quad (\text{C.6})$$

where $f(x) \sim t^\beta$ for $x \ll 1$ and $f(x) = \text{const}$ for $x \gg 1$. Thus

$$z = \frac{\alpha}{\beta} \quad (\text{C.7})$$

Statistics such as the mean height and interface width measure the vertical properties of a surface and do not reflect correlations between different lateral positions on the surface. Lateral correlation length $\xi_{||}$, the typical distance over which the surface heights “know about” each other - the characteristic distance over which they are

correlated. [101] At the beginning of the growth, the sites are correlated. During deposition $\xi_{||}$ grows with time.

$$\xi_{||} \sim t^{1/z} \quad \text{for} \quad t \ll t_X \quad (\text{C.8})$$

For a finite system $\xi_{||}$ cannot grow indefinitely, because it is limited by the size of the system, L . When $\xi_{||}$ reaches the size of the system, the entire interface becomes correlated, resulting in the saturation of the interface width. Thus at saturation

$$\xi_{||} \sim L \quad \text{for} \quad t \gg t_X \quad (\text{C.9})$$

These results imply that the scaling behavior of the surface for a particular model may be characterized by two parameters, the growth exponent β and roughness exponent α . Thus one expect that different types of growth may fall into a small number of universality classes, each characterized by given set if scaling exponents.

Alternatively, one may calculate other quantities related to correlations over a distance r from which the scaling behavior of the surface can be derived. One of these quantities is the height-height correlation function $G(r, t)$ as

$$G(r, t) = \langle \tilde{h}(0, t) \cdot \tilde{h}(r, t) \rangle = \frac{1}{L^{d-1}} \sum_i \left(h_i(t) - \overline{h(t)} \right) \left(h_{i+r}(t) - \overline{h(t)} \right) \quad (\text{C.10})$$

As can be seen from Fig. C-2 surface width $w(L, t)$ can be related to the height-

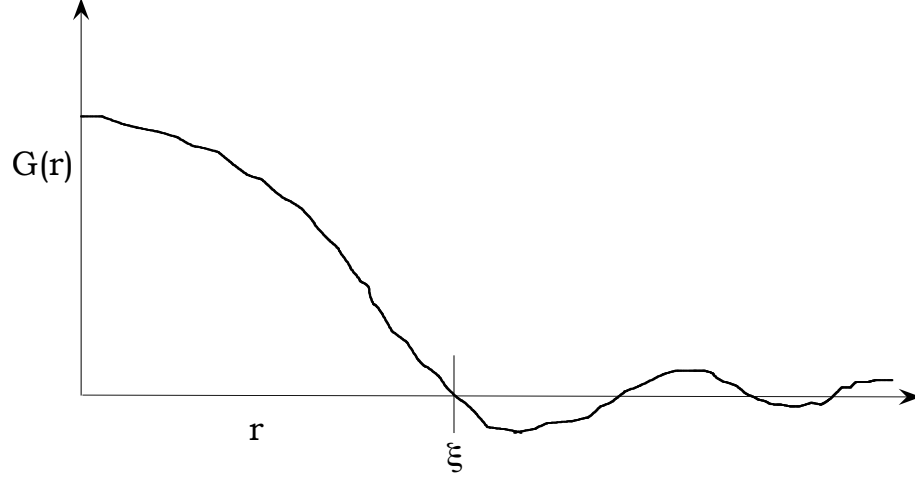


Figure C-2: The typical graph of the height-height correlation function $G(r)$

height correlation function $G(r, t)$ as,

$$W^2(L, t) = G(0, t) \quad (\text{C.11})$$

Typical, the lateral surface correlation length $\xi_{||}$ is assumed to be the value of the distance r_0 at which the height-height correlation function $G(r, t)$ first crosses zero, i.e.,

$$\xi_{||} \simeq r_0 \quad (\text{C.12})$$

Another such quantity is the height-difference correlation function $G_2(r, t)$:

$$G_2(r, t) = \frac{1}{L^{d-1}} \sum_i (h_{i+r}(t) - h_i(t))^2 \quad (\text{C.13})$$

which satisfies

$$G_2(r, t) \sim r^{2\alpha} \quad (\text{C.14})$$

One can find the relation between the roughness exponent α and the height-difference

correlation function $G_2(r, t)$.

In order to understand the scaling behavior of the surface growth in detail, one may introduce the so called general height-difference correlation function $G_n(r, t)$:

$$G_n(r, t) = \frac{1}{L^{d-1}} \sum_i |h_{i+2}(t) - h_i(t)|^n \quad (\text{C.15})$$

which satisfies

$$G_2(r, t) \sim r^{n\alpha_n} \quad (\text{C.16})$$

If the surface is self-affine and exhibits normal scaling, then $\alpha_n = \alpha$ is independent of n . Otherwise, the scaling behavior of the surface is multi-scaling and α_n depends on n .

Bibliography

- [1] D. Johnson. *Kinetic Monte Carlo: Bare Bones and a Little Flesh*.
- [2] J. M. Thijssen. *Computational Physics*. Cambridge University Press, New York, 1999.
- [3] S. Ozawa, Y. Sasajima, and D. W. Heermann. *Thin Solid Films*, 272:172, 1996.
- [4] J. M. Haile. *Molecular Dynamics Simulations: Elementary Methods*. John Wiley & Sons, 1992.
- [5] K. Ohno, K. Esfarjani, and Y. Kawazoe. *Computational Material Science: from ab initio to Monte Carlo Methods*. Springer, New York, 1999.
- [6] K. A. Fichthorn and W. H. Weinberg. *J. Chem. Phys.*, 95:1090, 1991.
- [7] A. B. Bortz, M. H. Kalos, and J. L. Lebowitz. *J. Comput. Phys.*, 17:10, 1975.
- [8] L. Xu and G. Henkelman. *J. Chem. Phys*, 129:114104, 2008.
- [9] F. El-Mellouhi, N. Maousseau, and L. J. Lewis. *Phys. Rev. B*, 78, 2008.
- [10] O. Trushin, A. Karim, A. Kara, and T. S. Rahman. *Phys. Rev. B*, 72:115401, 2005.

- [11] A. Karim, A. N. Al-Rawi, A. Kara, T. S. Rahman, O. Trushin, and T. Al-Nissila. *Phys. Rev. B*, 73:165411, 2006.
- [12] S. G. Eick, A. G. Greenberg, B. D. Lubachevsky, and A. Weiss. *ACM Trans. Model. Comput. Simul.*, 3:287, 1993.
- [13] PADS '01 IEEE. *Proceedings of the 15th Workshop on Parallel and Distributed Simulation*, Piscataway, NJ, 2001.
- [14] Y. Shim and J. G. Amar. *Phys. Rev. B*, 71:115436, 2005.
- [15] Richard M. Fujimoto. *Comm. of the ACM*, 33:30, 1990.
- [16] K. A. Fichtorn and M. Scheffler. *Phys. Rev. Lett.*, 84:5371, 2000.
- [17] Y. Shim and J. G. Amar. *Phys. Rev. B*, 71:125432, 2005.
- [18] James L. Blue, Isabel Beichl, and Francis Sullivan. *Phys. Rev. E*, 51:R867, 1995.
- [19] G. Nandipati, Y. Shim, J. G. Amar, A. Karim, A. Kara, T. S. Rahman, and O. Trushin. *J. Phys.:Condens. Matter*, 21:084214, 2009.
- [20] Y. Shim and J. G. Amar. *Phys. Rev. B*, 73:035423, 2006.
- [21] F. Shi, Y. Shim, and J. G. Amar. *Phys. Rev. E*, 76:031607, 2007.
- [22] C. V. Thompson. *Solid State Phys.*, 55:269, 2001.
- [23] R. Dhaubhadel, F. Pierce, A. Chakrabarti, and C. M. Sorensen. *Phys. Rev. E*, 73:011404, 2006.

- [24] L. Searle and R. Zinn. *Astrophys. Journ.*, 225:357, 1978.
- [25] M. Zinke-Allmang. *Thin Solid Films*, 346:1, 1999.
- [26] P. Meakin. *Physica A*, 165:1, 1990.
- [27] J. M. Wen, S.-L. Chang, J. W. Burnett, J. W. Evans, and P. A. Thiel. *Phys. Rev. Lett.*, 73:2591, 1994.
- [28] C. D Van Siclen. *Phys. Rev. Lett.*, 75:1574, 1995.
- [29] D. S. Sholl and R. T. Skodje. *Physica A*, 231:631, 1996.
- [30] D. S. Sholl and R. T. Skodje. *Phys. Rev. Lett.*, 75:3158, 1995.
- [31] J. M. Soler. *Phys. Rev. B*, 53:R10540, 1996.
- [32] W. W. Pai, A. K. Swan, Z. Zhang, and J. F. Wendelken. *Phys. Rev. Lett.*, 79:3210, 1997.
- [33] D. Kandel. *Phys. Rev. Lett.*, 79:4238, 1997.
- [34] G. R. Carlow and M. Zinke-Allmang. *Phys. Rev. Lett.*, 78:4601, 1997.
- [35] S. M. Foiles, M. I. Baskes, and M. S. Daw. *Phys. Rev. B*, 33:7983, 1986.
- [36] G. Mills H. Jónsson and K. W. Jacobsen. *Classical and Quantum Dynamics in Condensed Phase Simulations*. World Scientific, Singapore, 1998.
- [37] G. Henkelman and H. Jonsson. *J. Chem. Phys.*, 115:9657, 2001.
- [38] W. Ostwald. *Z. Phys. Chem.*, 37:385, 1901.

- [39] P. W. Voorhees. *J. Stat. Phys.*, 38:231, 1985.
- [40] S. V. Khare, N. C. Bartlet, and T. L. Einstein. *Phys. Rev. Lett.*, 75:2148, 1995.
- [41] I. M. Lifshitz and V. V. Slyozov. *J. Phys. Chem. Solids*, 19:35, 1961.
- [42] C. Wagner. *Z. Elektrochem.*, 65:581, 1961.
- [43] E. Cox, M. LI, P. Chung. C. Ghosh, T. S. Rahman, C. J. Jenks, J. W. Evans, and P. A. Theil. *Phys. Rev. B*, 71:115414, 2005.
- [44] J. G. Amar and F. Family. *Phys. Rev. Lett.*, 77:4584, 1996.
- [45] M. C. Bartelt and J. W. Evans. *Phys. Rev. B*, 46:12675, 1992.
- [46] J. M. Pomeroy and J. D. Brock. *Phys. Rev. B*, 73:245405, 2006.
- [47] G. H. Gilmer. *J. Crystal. Growth.*, 35:15, 1976.
- [48] A. F. Voter. *Phys. Rev. B*, 34:6819, 1986.
- [49] P. A. Maksym. *Semiconf. Sci. Technol.*, 3:594, 1988.
- [50] M. F. Gyure, C. Ratsch, B. Merriman, R. E. Caflisch, S. Osher, J. J. Zinck, and D. D. Vvedensky. *Phys. Rev. E*, 58(R6927), 1998.
- [51] C. A. Haselwandter and D. D. Vvedensky. *Phys. Rev. Lett*, 98:046102, 2007.
- [52] C. C. Chou and M. L. Falk. *J. Comput. Phys.*, 217:519, 2006.
- [53] L. M. Sander J. P. DeVita and P. Smereka. *Phys. Rev. B*, 72:205421, 2005.

- [54] C. C. Fu, J. D. Torre, F. Willaime, J. L. Bocquet, and A. Barbu. *Nat. Matter*, 4:68, 2005.
- [55] M. A. Novotny. *Phys. Rev. Lett.*, 74:1, 1995.
- [56] J. A. Given, J. B. Hubbard, and J. F. Douglas. *J. Chem. Phys*, 106:3761, 2006.
- [57] M. Mascagni and N. A. Simonov. *SIAM J. Sci. Comput.*, 26:339, 2004.
- [58] T. Opplestrup, V. V. Bulatov, G. H. Gilmer, M. H. Kalos, and B. Sadigh. *Phys. Rev. Lett*, 97:230602, 2006.
- [59] V. I. Tokar and H. Dreyssé. *Phys. Rev. E*, 77:066705, 2008.
- [60] A. El-shehawey. *J. Phys. A: Math Gen*, 33:9005, 2000.
- [61] J. Yu and J. G. Amar. *Phys. Rev. Lett*, 89:286103, 2002.
- [62] H.-J. Ernst, F. Fabre, R. Folkerts, and J. Lapujoulade. *Phys. Rev. Lett*, 72(112), 1994.
- [63] V. Borovikov, Y. Shim, and J. G. Amar. *Phys. Rev. B*, 76(241401), 2007.
- [64] C. E. Botez, W. C. Elliott, P. F. Miceli, and P. W. Stephens. *Phys. Rev. B*, 66(075418), 2002.
- [65] T.L. Einstein, J. Jacobsen, and C.Schiff. *Bull. Am. Phys. Soc.*, 42:26, 1997.
- [66] A. K. Swan, Z.-P. Shi, J. F. Wendelken, and Z. Zhang. *Surf. Sci.*, 391(4927), 1997.

- [67] G. Ehrlich and F. G. Hudda. *J. Chem. Phys.*, 44(1039), 1966.
- [68] L. Schwoebel. *J. Appl. Phys.*, 40(614), 1969.
- [69] J. Merikoski, I. Vattulainen, J. Heinonen, and T. Ala-Nissila. *Surf. Sci.*, 38:167, 1197.
- [70] G. Boisvert and L. J. Lewis. *Phys. Rev. B*, 56, 1997.
- [71] J. W. Evans, D. E. Sanders, P. A. Thiel, and A. E. DePristo. *Phys. Rev. B*, 41:R5410, 1990.
- [72] M. C. Bartelt and J. W. Evans. *Phys. Rev. Lett*, 75:4250, 1995.
- [73] J. G. Amar and F. Family. *Phys. Rev. B*, 54:14742, 1996.
- [74] S. Redner. *A guide to First-Passage Processes*. Cambridge University Press, New York, 2001.
- [75] Y. Saito. *Statistical Physics of Crystal Growth*. World Scientific, Singapore, 1996.
- [76] R. Nötzel, J. Temmyo, and T. Tamamura. *Nature*, 369, 1994.
- [77] R. Jullien, J. Kertesz, P. Meakin, and D. E. Wolf. *Surface Disordering: Growth, Roughening and Phase Transitions*. Nova, Commack, New York, 1993.
- [78] M. Notomi, J. Hammersberg, H. Weman, S. Nojima, H. Sugiura, M. Okamoto, T. Tamamura, and M. Potemski. *Phys. Rev. B*, 52:11147, 1995.

- [79] J. L. Gray, N. Singh, D. M. Elzey, R. Hull, and J. A. Floro. *Phys. Rev. Lett.*, 92:135504, 2004.
- [80] Y. W. Mo, D. E. Savage, B. S. Swartzentruber, and M. G. Lagally. *Phys. Rev. Lett.*, 65:1020, 1990.
- [81] D. J. Eaglesham and M. Cerullo. *Phys. Rev. Lett.*, 64:1943, 1990.
- [82] J. Tersoff and R. M. Tromp. *Phys. Rev. Lett.*, 70:2782, 1993.
- [83] Adam Li, Feng Liu, and M. G. Lagally. *Phys. Rev. Lett.*, 85:1922, 2000.
- [84] A. Pradhan, N. Y. Ma, and F. Liu. *Phys. Rev. B*, 70:193405, 2004.
- [85] J. Steinbrecher, H. Müller-Krumbhaar, E.A. Brener, C. Misbah, and P. Peyla. *Phys. Rev. E*, 59:5600, 1999.
- [86] L. D. Landau and I. M. Lifshitz. *Theory of Elasticity*. Butterworth-Heinemann, Oxford, 1999.
- [87] F. Guthiem, H. Müller-Krumbhaar, and E. Brener. *Phys. Rev. E*, 63:041603, 2001.
- [88] B. M. T. Goncalves and J. F. F. Mendes. *Phys. Rev. E*, 65:061602, 2002.
- [89] C. Ratsch, A. Zangwill, and P. Šmilauer. *Surf. Sci.*, 314:L937, 1994.
- [90] Y. Chen and J. Washburn. *Phys. Rev. Lett.*, 77:4046, 1996.
- [91] C. Ratsch, A. P. Seitsonen, and M. Scheffler. *Phys. Rev. B*, 55:6750, 1997.

- [92] L. Huang, F. Liu, and X. G. Gong. *Phys. Rev. B*, 70:155320, 2004.
- [93] D. J. Shu, F. Liu, and X. G. Gong. *Phys. Rev. B*, 64:245410, 2001.
- [94] M. M. Hurley and S. G. Singer. *J. Chem. Phys.*, 96:1938, 1992.
- [95] V. Bressler-Hill, S. Varma, A. Lorke, B.Z. Nosho, P.M. Petroff, and W.H. Weinberg. *Phys. Rev. Lett.*, 74:3209, 1995.
- [96] G. R. Bell, T. J. Krzyzewskik, P. B. Joyce, and T. S. Jones. *Phys. Rev. Lett.*, 61:R10551, 2000.
- [97] B. Müller, L.P. Nedelmann, B. Fischer, J.V. Barth H. Brune, K. Kern, D. Erdös, and J. Wollschläger. *Surf. Rev. and Lett.*, 5:769, 1998.
- [98] Jean-Noel Aqua and Thomas Frisch. *Phys. Rev. B*, 78:121305(R), 2008.
- [99] M. Abramowitz and I. A. Stegun. *Handbook of Mathematical Functions*. New York, 1970.
- [100] F. Family and T. Vicsek. *J. Phys. A*, 18:L75, 1985.
- [101] A.-L. Barabasi and H. E. Stanley. *Fractal Concepts in Surface Growth*. Cambridge University Press, New York, 1995.